2014

Analysis and development of transcranial magnetic stimulation devices

Lawrence James Crowther
Iowa State University

Analysis and development of transcranial magnetic stimulation devices

by

Lawrence James Crowther

A dissertation submitted to the graduate faculty

in partial fulfillment of the requirements for the degree of

DOCTOR OF PHILOSOPHY

Major: Electrical Engineering

Program of Study Committee:
David C. Jiles, Major Professor
John Basart
Tim Bigelow
Ravi Hadimani
Anumantha Kanthasamy
Mani Mina

Iowa State University
Ames, Iowa
2014

TABLE OF CONTENTS

Page

LIST OF FIGURES

LIST OF TABLES

ACKNOWLEDGEMENTS

I would like to thank my committee chair, David C. Jiles, and my committee members, John Basart, Tim Bigelow, Ravi Hadimani, Anumantha Kanthasamy, and Mani Mina, for their guidance and support throughout the course of this research. In addition, I would also like to thank my friends, colleagues, the department faculty and staff for making my time at Iowa State University a wonderful experience. Finally, thanks to my family for their encouragement and support throughout my studies.

ABSTRACT

Transcranial magnetic stimulation (TMS) is an emerging technique to stimulate neural tissue non-invasively by inducing electric field in the brain with pulsed high-intensity magnetic field. The advantages of stimulating neural tissue in this way have resulted in the technique being rapidly adopted for research and clinical purposes. Advances in the depth and localization of stimulation that TMS can achieve will allow new applications to be established that could replace surgical alternatives.

To evaluate the performance of coils used for TMS it is necessary to understand how electric field is induced in neural tissue. To model this phenomenon, numerical methods and anatomically realistic human head models have been employed to accurately determine where neural stimulation will occur. The results of this analysis reveal the simplified homogeneous head models used in earlier studies are unable to correctly predict the distribution of induced electric field at depth in the brain.

This method has subsequently been applied to develop novel coil designs to facilitate stimulation of deep-lying brain regions. Additionally, the mechanical stress experienced by TMS coils has been investigated to support further development of combined neuromodulation and neuroimaging systems.

CHAPTER I

INTRODUCTION

1.1 Transcranial magnetic stimulation

Transcranial magnetic stimulation (TMS) is a neuromodulation technique with the distinction of being able to activate neurons in the brain non-invasively. This ability has led to TMS being widely adopted for research in fields including clinical neurophysiology, cognitive neuroscience and psychiatry. In recent years, TMS has become an established non-pharmacologic therapy for drug-resistant major depressive disorder (MDD). Further applications of the technique are likely to present themselves if current engineering limitations can be overcome. Three principle limitations are addressed in this thesis; theoretical determination of the locus of stimulation in the brain, the ability to stimulate neural tissue at depth, and physical constraints encountered when combining TMS with neuroimaging techniques such as magnetic resonance imaging (MRI).

1.1.1 Development of transcranial magnetic stimulation

The concept of electromagnetic induction was developed in 1831 by Faraday. Faraday demonstrated that a time-varying magnetic field could cause electric current to flow in nearby conductive materials.

While attempts to stimulate the brain using time-varying magnetic fields were made as early as 1896 by d'Arsonval [1], the phenomenon has only been used in recent decades as a therapeutic modality in psychiatry, referred to as repetitive transcranial

magnetic stimulation (rTMS), which was approved for the treatment of MDD by the United States Food and Drug Administration (FDA) in 2008.

Electromagnetic induction is the major principle in TMS, due to the moving electric charge in a coil generates a magnetic field surrounding it. Alternating currents bring about fluctuating magnetic fields that cause an electric field and hence cause electric current to flow in nearby conductors, which in the case of TMS is weakly conducting brain tissue. This enables electrical stimulation of neurons within the brain in a non-invasive fashion. The most commonly used form of expression for this concept is the Maxwell-Faraday equation, shown in differential form in (1.1), which states that a circulating electric field is produced by a magnetic field that changes with time. This is also commonly referred to as Faraday's Law.

$$\vec{\nabla} \times \vec{E} = -\frac{\partial \vec{B}}{\partial t} \tag{1.1}$$

The connection between electricity and neural tissue was established prior to the discovery of electromagnetic induction, in the work of Galvani (1737-1789). Galvini discovered that frogs' legs would move when touched by two different conductors and concluded that muscles and electricity were somehow related. The earliest attempts to stimulate the human cortex with magnetic field can be traced to the work of d'Arsonval, who reported 'phosphenes' (the experience of 'seeing lights' due to stimulation of the retina) in 1896, by application of an alternating magnetic field generated by a coil with a voltage of 110 V and a current of 30 A at a frequency of 42 Hz. Thompson, unaware of work by d'Arsonval, performed a similar experiment later, in 1910, and also reported phosphenes he termed 'magnetophosphenes' by using a coil with 32 turns, 9 inches in diameter and 8 inches in length [2]. Thompson's coil was driven with a current of 180 A

at a frequency of 50 Hz, creating a reported magnetic field of 1400 Oe at center of the coil (approximately 1.11×10^5 A/m in SI units). It was later discovered by Barlow [3] that these phosphenes were arising from stimulation of the retina and not from stimulation of visual pathways in the brain as was previously thought. With the development of more powerful electronic components, pulsed magnetic field was used to activate muscles in small animals and humans in 1965 by Bickford and Fremming [4]. Non-invasive stimulation of the human motor cortex was finally achieved by Barker *et al.* in 1985 [5] whereupon adoption of the technique for various applications was initiated. Further overview of the historical development of TMS is provided by Geddes [6], George and Belmaker [7] and Walsh and Pascual-Leone [8].

1.1.2 Technical details and device design

TMS stimulators supply pulsed electric current to a coil to produce the time-varying magnetic field necessary for stimulation of neural tissue. A large capacitor is discharged by a thyristor switch, designed to reduce losses and be able to carry currents of thousands of amps. The characteristics of the discharged current are determined by the resonant frequency of the stimulator circuitry. For TMS, the primary consideration is the rate of change of current and subsequent magnetic field with respect to time. There are two types of TMS stimulator and they are distinguished by the characteristics of the waveform they produce: monophasic and biphasic. Monophasic TMS stimulators as depicted in Figure 1.1 are simpler in design and unable to generate the repetitive pulse sequences required for therapeutic use through rTMS. A typical waveform produced by a monophasic stimulator is shown in Figure 1.2.

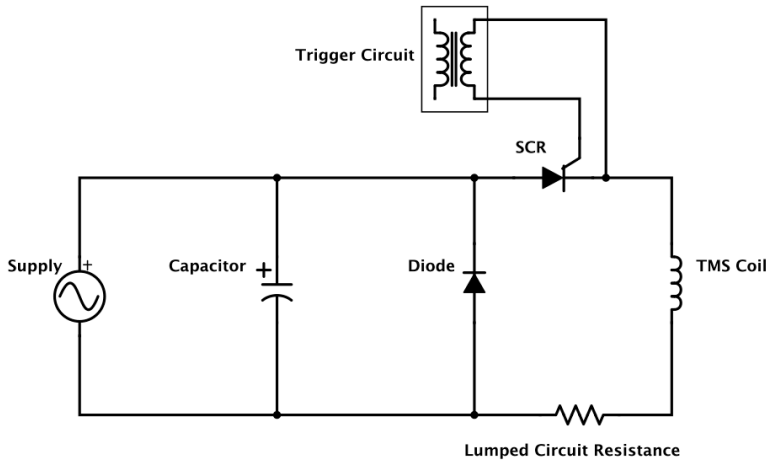

Figure 1.1. Simplified circuit diagram of a monophasic TMS pulse generator [9].

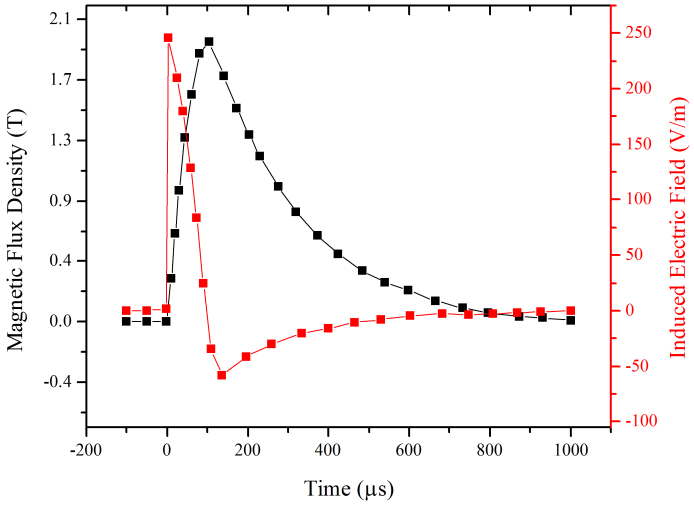

Figure 1.2. Magnetic flux density and induced electric field over a typical monophasic TMS pulse cycle. The electric current in the coil will correspond with the waveform of the magnetic flux density.

Biphasic TMS stimulators as depicted in Figure 1.3 allow short inter-pulse periods needed for rTMS. A typical waveform produced by a biphasic stimulator is shown in Figure 1.4. This type of stimulator has become more widely utilized due to its rTMS ability, offering pulse repetition rates of 100 Hz [10]. Figure 1.4 shows the relationship between the current (and magnetic flux density) intensity and the electric field induced in the conducting tissue.

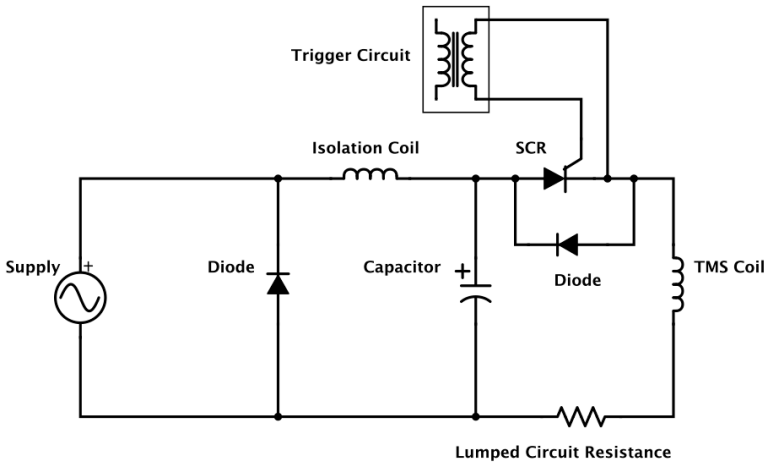

Figure 1.3. Simplified circuit diagram of a biphasic TMS pulse generator [9].

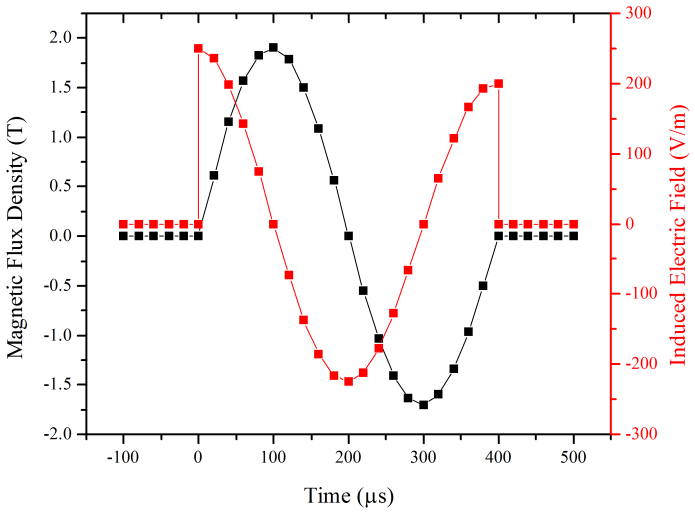

Figure 1.4. The magnetic flux density and induced electric field over a typical biphasic TMS pulse cycle. The electric current in the coil will correspond with the waveform of the magnetic flux density.

Coils first used for TMS had flat circular geometry as shown in Figure 1.5 (a). These coils are constructed from approximately a dozen turns of thick copper wire. A few years following the inception of TMS, Ueno *et al.* [11] proposed a new coil configuration, the figure-8 coil, with the ability to more easily target brain regions. An example of a figure-8 coil is shown in Figure 1.5 (b).

Figure 1.5. (a) Circular Magstim HP90 (R) and (b) figure-8 Magstim D70 (R) remote control TMS coils.

The magnetic and electric field produced by these two types of coil are shown in Figure 1.6. The fields have been calculated in a plane 20 mm from the surface of the coils, based on simple models of the circular Magstim HP90 (R) (P/N 3192-00) and figure-8 Magstim D70 (R) (P/N 3190-00) 2nd generation remote control coils, having inductances of 23.47 and 15.50 μH and maximum reported field strengths of 2.0 and 2.2 T, respectively. The calculations were performed with a homogeneous conducting medium with electrical conductivity 0.33 S/m to calculate the induced electric field. Figure 1.6 (c) shows the large ring-shape of maximum intensity of induced electric field produced by the circular coil. Figure 1.6 (d) shows the central peak of maximum induced electric field intensity produced by the figure-8 coil demonstrating its advantage over the circular coil in targeting brain regions selectively.

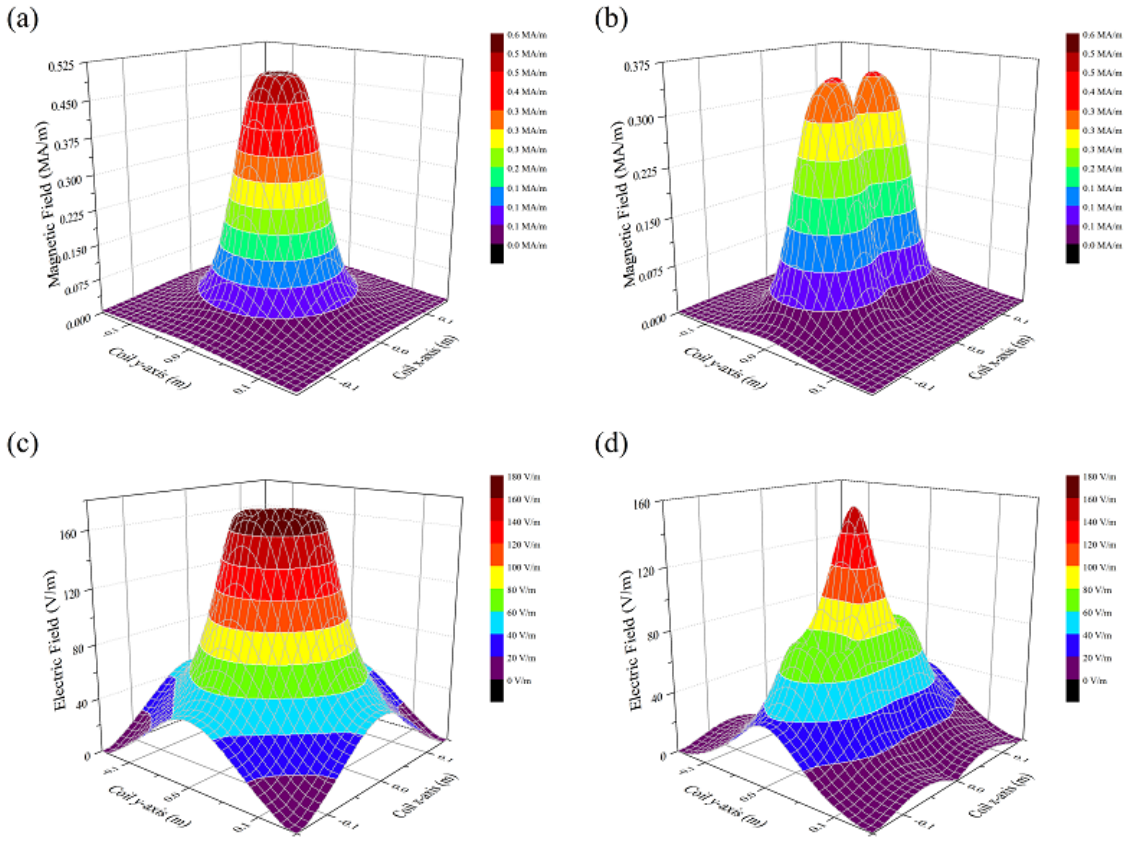

Figure 1.6. Calculated magnetic field in a plane 20 mm from (a) modeled circular TMS coil and (b) modeled figure-8 TMS coil, and electric field induced in a homogeneous conducting medium in a plane 20 mm from (c) modeled circular TMS coil and (d) modeled figure-8 TMS coil.

1.1.3 Applications and protocols

TMS offers a degree of localization such that a physiological or behavioral effect can be created by stimulating the relevant part of the cortex. For example, if the corresponding part of the primary motor cortex is targeted, the subject's thumb will twitch. In a similar fashion, if the Broca's area is targeted speech production will be affected. This allows the technique to be used to map brain function and study cortical connectivity. Figure 1.7 depicts the lobes of the brain and other prominent features.

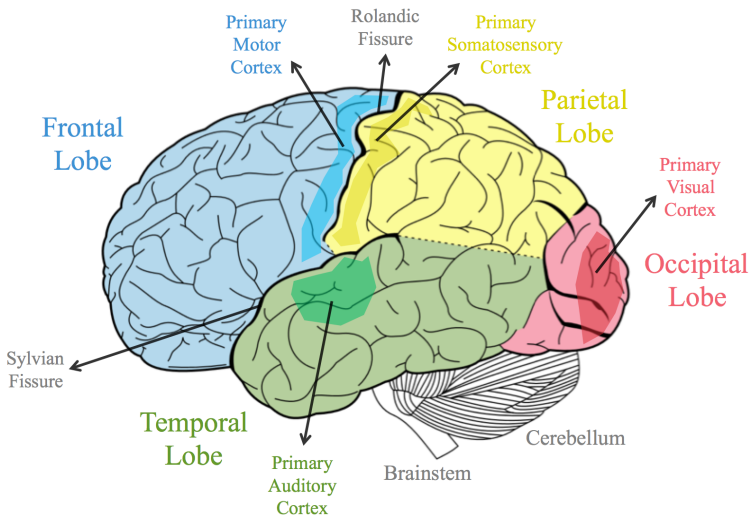

Figure 1.7. Principle features and lobes of the brain, modified from Gray's Anatomy Fig. 728 [12].

Since the inception of the technique, TMS has been used for a variety of studies. Early clinical investigations demonstrated increased latencies between the motor cortex and target muscles in patients with multiple sclerosis and motor neuron disease [13]. To date the main therapeutic use of TMS is in the treatment of MDD. MDD is one of the most prominent mental disorders in the United States, affecting 6.7% of the adult population. On average the onset of MDD occurs at 32 years although 3.3% of 13 to 18 year olds also experience MDD [14].

Establishing protocols or pulse sequences for TMS treatment requires that frequency, intensity, and duration of stimulation be determined. Stimulation frequency is typically chosen based upon the desired effect. An increase or decrease in cortical excitability can be caused, with an increase usually brought about by high frequency pulse trains. Conversely, low frequency pulse trains will decrease excitability in the stimulated region. The approved treatment for MDD consists of pulse trains lasting four seconds at 10 Hz, delivered to the left dorsolateral prefrontal cortex (DLPFC). This

causes an increase in cortical excitability in this area. Some studies in the treatment of Tourette's disorder have used a low frequency pulse train of 1 Hz over the supplementary motor area (SMA), with the anticipation that cortical excitability will be decreased.

Intensity of stimulation is primarily established by the baseline cortical excitability, which can be determined by the minimum intensity required to cause a motor evoked potential (MEP). In clinical practice, this can be determined by observation of muscle movement and is known as the resting motor threshold (RMT). Stimulation intensity in TMS protocols can then be expressed as a percentage of the patient's RMT, for example, the approved treatment for MDD is typically performed at an intensity of 120% of the patient's RMT.

The duration of a TMS pulse train also has an effect upon the duration of the subsequent effects. A 15-minute train of rTMS in the motor cortex, at approximately 1 Hz can reduce cortical excitability for the subsequent 15 minutes, while single pulse TMS has been shown to only change cortical excitability for approximately 200 ms.

Many previous studies of cortical excitability following pulse sequences vary in utilized frequency, intensity and duration and are therefore at times seemingly inconsistent as a result. Practically it is useful to work with the paradigm that cortical excitability can be increased with high frequency pulse trains, while low frequency will decrease it. Longer durations of stimulus will generally increase the duration of subsequent effects.

Theta burst stimulation (TBS) protocols utilize high frequency pulse train bursts (up to 100 Hz) at 5 Hz intervals, consistent with theta rhythm as measured by electroencephalography (EEG). Two main categories of TBS protocols have been

established, intermittent (iTBS) and continuous (cTBS), with excitatory and inhibitory effects, respectively. For 50 Hz bursts of three pulses, repeated every 200 ms, iTBS is defined as 10 bursts of stimulation repeated every ten seconds for a total of 191.84 s, or a total of 600 pulses. cTBS is defined as 20 or 40 s of continuous stimulation for a total of 300 or 600 pulses. TBS protocols are still in the investigational stage, but indicate that similar effects to rTMS may be possible with significantly shorter treatment times, with similar or sometimes even greater duration of excitatory and inhibitory effects.

1.1.4 Safety

When dealing with a medical device the safety of the procedure must be thoroughly investigated. The majority of TMS patients do not suffer adverse effects from single-pulse TMS or rTMS and no fatal events have been reported. However, a variety of safety concerns can potentially arise. To avoid adverse effects a list of guidelines for safely conducting TMS experiments was established by Pascual-Leone *et al.* in 1993 [15]. More recently, in 2008, a consensus conference was held to establish safety guidelines for TMS in research and clinical practice. The outcome of the conference are the guidelines by Rossi *et al.* [16] which take into account more recent findings and recommendations.

One of the main safety concerns with TMS is the possibility of inducing a seizure. Although the occurrence of seizure is rare, high-frequency rTMS is believed to lower the seizure threshold in susceptible persons [17]. As a result the guidelines describe a variety of conditions that should exclude certain individuals from participating in TMS studies, including individuals with epilepsy, multiple sclerosis or subjects using tricyclic

antidepressants or neuroleptic agents. A more common problem encountered during TMS is the loud clicking noise that is created by the TMS coil. This noise is sufficiently loud to potentially damage a subject's hearing but is easily avoided through the use of earplugs.

Headaches can also arise as a result of recurring stimulation of peripheral nerves in the face and scalp and are experienced in 5 to 25% of patients. Burns can potentially occur during TMS if metal objects are in contact with the skin, as they will be heated by the pulsed magnetic field. Mechanical forces can also be exerted on implants in proximity to a stimulation coil and such devices should preclude subjects from the procedure.

1.2 Other methods of brain stimulation

Transcranial magnetic stimulation is one of a number of neuromodulation methods. The following overview of the alternative techniques identifies the relative strengths and weaknesses of TMS.

1.2.1 Transcranial direct current stimulation

The technique whereby a weak constant current is caused to flow through the cortex by electrodes placed on the scalp is referred to as transcranial direct current stimulation (tDCS). Typically sub-threshold stimulation increases neural activity near the anode due to membrane depolarization while this spontaneous activity is reduced with a reversed polarity due to hyperpolarization.

1.2.2 Deep brain stimulation

Deep brain stimulation (DBS) describes the method of stimulating deep-lying brain regions with surgically inserted electrodes. DBS was approved by the FDA for treatment of Parkinson's disease and essential tremor in 1997. The benefits of this technique are the highly localized targeting capabilities that have yielded significant results in the treatment of the motor symptoms of Parkinson's disease (PD), essential tremor and dystonia. Typically, a pair of electrodes are inserted into the brain and are controlled by a generator implanted in the chest, in similar fashion to a cardiac pacemaker. Despite the invasive surgery required, there are currently over 100,000 DBS devices in use worldwide [18]. Use of DBS as a treatment for MDD is still under investigation although an early study of DBS for treatment-resistant MDD resulted in four of six subjects demonstrating marked improvement following the procedure [19].

1.2.3 Vagus nerve stimulation

The vagus nerve originates in the medulla of the central nervous system (CNS) and passes through the neck, chest and abdomen. Electrical stimulation of the vagus nerve in the neck has been proposed as a treatment for epilepsy, MDD, anxiety and migraine [20]. Vagus nerve stimulation (VNS) was approved by the FDA as a therapy for epilepsy in 1997. The technique was later approved for treatment-resistant MDD in 2005, for subjects who have had the illness for more than two years and for whom other treatments have proven ineffective.

1.2.4 Electroconvulsive therapy

In the decades since electroconvulsive therapy (ECT) was first developed the procedure has improved into a safe and effective treatment for MDD and other conditions such as bipolar disorder and schizophrenia. One of the foremost drawbacks of the treatment is the likelihood of amnestic effects [21], although it is believed this can be reduced by administering ECT unilaterally as opposed to bilaterally. As with most neuromodulation techniques, ECT is usually only considered for therapeutic use if a subject's symptoms have not improved with medication or psychotherapy. The treatment requires the subject to be sedated with general anesthesia and given muscle relaxant medication. Electrodes are used to pass current through the brain, causing a seizure typically lasting less than a minute.

A similar treatment using pulsed magnetic field instead of electrodes has more recently been proposed. Magnetic seizure therapy (MST) uses higher stimulation rates than TMS and is intended to induce seizure in the patient to obtain the same therapeutic benefits as ECT. The efficacy of this procedure is still unknown.

1.3 Effect upon neural tissue

Neural cells work to perform the numerous functions of the nervous system including cognition, emotion, movement, sensory perception, and regulation of circulation and respiration. There are two main categories of neural cells, neurons and glia. Structural and functional types of both categories exist but in general it can be stated that the function of neurons is to process and transmit information while glial cells

support the function of neurons. There are approximately 100 billion neurons in the adult human brain forming trillions of connections throughout the nervous system. The central nervous system (CNS) comprises of the brain and spinal cord while the peripheral nervous system (PNS) consists mostly of nerves, stemming from the central nervous system and going to the extremities.

1.3.1 Action potentials, chronaxie and rheobase

The resting membrane potential of a neuron is approximately -70 mV due to the relative intracellular and extracellular concentrations of potassium, sodium and chloride ions. If the membrane potential changes to approximately -40 mV the sodium channels open and a short flow of ionic current will occur, briefly shifting the membrane potential to +20 mV before returning to the resting potential. This process is referred to as an action potential. During TMS, action potentials are caused by the transient magnetic field inducing electric field in the neural tissue, which can then propagate along the nerve.

When considering the effect of TMS upon a neuron, two primary factors include rheobase and chronaxie. Rheobase is the lowest intensity of current that can generate an action potential in a neuron. Chronaxie is the minimum time for a current to double the strength of the rheobase of a neuron. When a magnetic field pulses next to neural tissue, an electric field can potentially be generated with the necessary characteristics to cause neurons to depolarize, resulting in action potentials. As stated, when the motor cortex is stimulated in this way, the result is an MEP, leading to motor activity. Stimulation of other brain regions may not be consciously experienced by the subject but have resulted in measurable changes, such as in a subject's performance of a cognitive task.

Practical application of TMS is mostly focused on rTMS, where pulses are delivered in trains at certain frequencies, having been shown to bring about lasting effects. Typically, low frequency stimulation (~1 Hz) causes reduced cortical excitability, while high frequency stimulation (> ~5 Hz) increases cortical excitability. In both cases, a lasting effect can be observed following treatment. Although the mechanism of stimulation is not entirely understood, the effect can be described by the phenomena of long-term potentiation (LTP) and long-term depression (LTD) [22].

1.3.2 Long-term potentiation and depression

LTP is a process by which synaptic communication between neurons becomes more efficient by the neurons firing in sequence. The process was first defined by Lømo in 1966 and describes how a single electric stimulus delivered to pre-synaptic fibers can result in excitatory post-synaptic potentials (EPSPs) [23]. LTD describes the opposite process to LTP and is thought to result primarily from a reduction in post-synaptic receptor density, with L-glutamate affecting multiple receptors to selectively reduce receptor strength. It is believed that the modulation of these phenomena is the method by which rTMS causes lasting effects and clinical utility.

References

[1] A. d'Arsonval, "Dispositifs pour la mesure des courants alternatifs de toutes fréquences," *CR Soc Biol*, vol. 2, pp. 450–451, 1896.

[2] S. P. Thompson, "A physiological effect of an alternating magnetic field," *Proc. R. Soc. London. Ser. B, Contain. Pap. a Biol. Character*, pp. 396–398, 1910.

[3] H. B. Barlow, H. I. Kohn, and E. G. Walsh, "Visual sensations aroused by magnetic fields," *Am. J. Physiol*, vol. 148, pp. 372–375, 1947.

[4] R. G. Bickford and B. D. Fremming, "Neuronal stimulation by pulsed magnetic fields in animals and man," in *Digest 6th Int Conf Med Electronics Biol Eng*, 1965, vol. 112.

[5] A. T. Barker, R. Jalinous, and I. L. Freeston, "Non-invasive magnetic stimulation of human motor cortex," *Lancet*, vol. 325, no. 8437, pp. 1106–1107, 1985.

[6] L. A. Geddes, "History of magnetic stimulation of the nervous system," *J. Clin. Neurophysiol.*, vol. 8, no. 1, pp. 3–9, 1991.

[7] M. George, *Transcranial magnetic stimulation in clinical psychiatry*. Washington, DC: American Psychiatric Pub, 2007.

[8] V. Walsh, *Transcranial magnetic stimulation : a neurochronometrics of mind*. Cambridge, Mass. London: MIT, 2005.

[9] E. Wassermann, C. Epstein, and U. Ziemann, *Oxford handbook of transcranial stimulation*. Oxford University Press, 2008.

[10] "Magstim Rapid P/N 3576-23-08 Operating Manual." The Magstim Company, 2006.

[11] S. Ueno, T. Tashiro, and K. Harada, "Localized stimulation of neural tissues in the brain by means of a paired configuration of time-varying magnetic fields," *J. Appl. Phys.*, vol. 64, no. 10, pp. 5862–5864, 1988.

[12] H. Gray, *Anatomy of the human body*. Lea & Febiger, 1918.

[13] A. T. Barker, I. L. Freeston, R. Jalinous, and J. A. Jarratt, "Clinical evaluation of conduction time measurements in central motor pathways using magnetic stimulation of human brain," *Lancet*, vol. 327, no. 8493, pp. 1325–1326, 1986.

[14] "What Is Depression?," *The National Institute of Mental Health*. [Online]. Available: http://www.nimh.nih.gov/health/topics/depression/index.shtml.

[15] A. Pascual-Leone, C. M. Houser, K. Reese, L. I. Shotland, J. Grafman, S. Sato, J. Valls-Sole, J. P. Brasil-Neto, E. M. Wassermann, L. G. Cohen, and others, "Safety of rapid-rate transcranial magnetic stimulation in normal volunteers," *Electroencephalogr. Clin. Neurophysiol. Potentials Sect.*, vol. 89, no. 2, pp. 120–130, 1993.

[16] S. Rossi, M. Hallett, P. M. Rossini, and A. Pascual-Leone, "Safety, ethical considerations, and application guidelines for the use of transcranial magnetic

stimulation in clinical practice and research," *Clin. Neurophysiol.*, vol. 120, no. 12, pp. 2008–2039, 2009.

[17] E. Wassermann, L. Cohen, S. Flitman, R. Chen, and M. Hallett, "Seizures in healthy people with repeated' safe' trains of transcranial magnetic stimuli," *Lancet*, vol. 347, no. 9004, pp. 825–826, 1996.

[18] "Deep Brain Stimulation for Movement Disorders," *Medtronic, Inc.*, 2014. .

[19] H. S. Mayberg, A. M. Lozano, V. Voon, H. E. McNeely, D. Seminowicz, C. Hamani, J. M. Schwalb, and S. H. Kennedy, "Deep brain stimulation for treatment-resistant depression," *Neuron*, vol. 45, no. 5, pp. 651–660, 2005.

[20] D. A. Groves and V. J. Brown, "Vagal nerve stimulation: a review of its applications and potential mechanisms that mediate its clinical effects," *Neurosci. Biobehav. Rev.*, vol. 29, no. 3, pp. 493–500, 2005.

[21] S. H. Lisanby, J. H. Maddox, J. Prudic, D. P. Devanand, and H. A. Sackeim, "The effects of electroconvulsive therapy on memory of autobiographical and public events," *Arch. Gen. Psychiatry*, vol. 57, no. 6, pp. 581–590, 2000.

[22] P. B. Fitzgerald, S. Fountain, and Z. J. Daskalakis, "A comprehensive review of the effects of rTMS on motor cortical excitability and inhibition," *Clin. Neurophysiol.*, vol. 117, no. 12, pp. 2584–2596, 2006.

[23] T. Lømo, "The discovery of long-term potentiation," *Philos. Trans. R. Soc. London. Ser. B Biol. Sci.*, vol. 358, no. 1432, pp. 617–620, 2003.

CHAPTER II

BACKGROUND

2.1 Coil design for transcranial magnetic stimulation

Much of the technological development of TMS has focused on the design of the coil used to stimulate the brain. Changing the geometry and construction of the coil affects the characteristics of the magnetic field it produces, which in turn changes the distribution of electric field that is induced in the brain. Through modification of the coil design it has previously been demonstrated, to some extent, that it is possible to change the localization of stimulation and the depth at which a stimulating magnetic field can penetrate.

2.1.1 Initial coil designs

Since the time that non-invasive stimulation of the human motor cortex was first demonstrated by Barker *et al.* in 1985 [1], TMS stimulator coils have primarily comprised of flat circular geometries. The greatest electric field induced by these coils is directly below the coil windings. This means that circular coils do not produce a single location of maximum field. However, circular coils are able to stimulate both hemispheres of the brain simultaneously to some degree, when the coil is placed at the cranial vertex. The direction of induced current can affect the extent to which neural stimulation can be achieved in the motor cortex, currents flowing from posterior to anterior are preferential. Therefore, in this scenario one hemisphere will be preferentially stimulated.

Flat circular coils are still utilized and commercially produced [2] but have largely been succeeded by more complex designs for clinical and therapeutic use. Ueno *et al.* [3] proposed the figure-8 coil in 1988 as a method to achieve localized stimulation by combining two coil windings side by side, with currents flowing in the same direction at the point where the two coils meet. The resulting electric fields constructively interfere, allowing focused stimulation. Although the figure-8 coil allows the localization of stimulation to be greatly increased, the attenuation of electric field within a homogeneous volume conductor occurs more rapidly for a figure-8 coil than a circular coil [4], [5] reducing the ability of a figure-8 coil to stimulate deep-lying brain regions.

2.1.2 Evolution of coil designs

The double-cone coil is a variant of the figure-8 coil where rather than both coil windings being flat relative to each other, each side of the coil are rotated form an angle. This allows the coil to create higher intensities of electric field at depth than is possible with a standard figure-8 coil. Some investigations have shown the double-cone coil to be capable of stimulating the leg motor area, located 30 to 40 mm below the surface of the scalp [6], [7]. Roth *et al.* [8] have estimated the stimulation threshold of neurons to be 20 to 60 V/m, requiring only 30 to 50% of the maximum output possible with a common commercial TMS stimulator, when using the double-cone coil. It has been indicated that attempting stimulation of deeper-lying regions can be painful for the subject, due to the high-intensity field being induced in higher cortical areas and the potential stimulation of facial muscles. Another limitation of the geometry of the double-cone coil is that it produces larger field intensities at the sides of the head. The field in these regions can

approach 50% of the maximum field produced below the center of the coil when stimulator output is 150% [9]. In this scenario, the field in these regions is theoretically capable of stimulating neural tissue. As a result, care must be taken when using the double-cone coil to ensure that only brain regions below the center of the coil are affected.

To decrease the field intensity away from the center of figure-8 coils, double-butterfly coils and later, eccentrically wound coils have been developed [10], [11]. Other methods to manipulate the field produced by figure-8 coils include the use of a conductive shielding plate [12] and 'active' shielding by secondary coil causing counteracting magnetic fields [13]. Layering multiple figure-8 coils has also been proposed [14].

In order to achieve an effective 'sham' coil for use in clinical studies, coils with the capability of engaging a reverse-current mode have been developed [15], which provide the sensation of stimulation without generating a field with enough intensity for neural stimulation. Most TMS coils rely solely upon the field produced by the current carrying conductor in the coils to produce the stimulating field. However, coils that make use of ferromagnetic iron cores have been also been proposed in coils of different designs and sizes [16]–[19] and have been utilized in widely-used commercial systems [20].

2.1.3 Coils for stimulation of deep-lying brain regions

The ability to apply TMS to deep brain regions has proved difficult due to the rapid attenuation of electric field intensity as a function of distance from the stimulator coil [4], [5], [21]–[23]. If commonly used coil designs are utilized to stimulate deep brain

regions, the high intensity of field that is required also stimulates cortical regions and possibly facial nerves to an extent that can cause pain [8]. However, being able to stimulate deep brain regions non-invasively could allow the development of therapeutic applications for various brain disorders [24]. TMS of deep brain regions could also create a non-invasive treatment for tremor arising from Parkinson's disease and dystonia in place of DBS.

When developing TMS coils for the stimulation of deep brain regions various factors must be considered. The stimulation threshold of neurons must be fully understood to guarantee new coil designs will be capable of stimulating desired regions. Conflicting values of stimulation threshold can be found in the literature with values of required intensity ranging from 20 to 100 V/m [8], [25]. Variations in this value are likely due to the alignment of the neurons and the overlying gyral folding pattern. Limitations of the available TMS stimulators must also be considered, such as new coils conforming to existing inductance ranges, typically 15 to 25 μH.

Roth *et al.* have also proposed a coil design to improve the depth of stimulation, termed the Hesed Coil (H-Coil), identifying that existing TMS coils can only stimulate cortical brain regions [8]. The field produced by several of these coil designs has been calculated using the method proposed by Eaton [21], assuming a current discharge of 10 kA in 100 μs. Roth *et al.* identified the effect of coil position on induced electric field, revealing that coil components that are perpendicular to the surface of the brain create an accumulation of surface charge that negatively affects, or even cancels, the perpendicular component of the induced electric field. The H-Coil attempts to minimize the presence of coil components that are not tangential to the tissue surface. Zangen *et al.* [26] report on a

modified H-Coil for stimulation of the abductor pollicis brevis (APB) area of the motor cortex to test the H-coil. The RMT was measured in patients as the H-Coil was increasingly moved away from the scalp. The intensity required for stimulation of the APB at several distances from the scalp using the H-Coil and a figure-8 coil were compared. As the distance from the scalp increased, the stimulator output required to stimulate the APB was shown to be lower for the H-Coil than for the figure-8 coil. When the maximum stimulator output was used, the figure-8 coil could stimulate the APB at a distance of 20 mm from the scalp while the H-Coil could stimulate the APB at a distance of 55 mm. However, a thorough comparison of the H-Coil and a figure-8 coil conducted by Fadini *et al.* [27], indicated that no significant advantage of the H-coil was found with regard to depth of stimulation.

2.2 Electromagnetic modeling

Electromagnetic modeling techniques can be used to calculate the magnetic and electric field produced by coils used for TMS. Since Barker's demonstration of TMS in 1985 [1], many attempts to improve the performance of TMS have been made. Much of this work relies on the ability to accurately predict the nature of the field induced inside the human head by an external electromagnetic field. The emergence of TMS was one of a number of techniques that have factored in the development of human head models for electromagnetic modeling. Techniques such as electroencephalography (EEG) and magnetoencephalography (MEG) have also given rise to a desire to accurately characterize magnetic field patterns in the brain.

2.2.1 Human head modeling

Efforts to develop realistic finite element head models were made by Thevenet *et al.* in 1992 [28]. These studies looked to assess the relationship between potentials in the human scalp and neural current sources in the brain. A four-layer concentric sphere model of the head was used with radii for brain, cerebrospinal fluid (CSF), skull and scalp of 0.84, 0.87, 0.92, and 1, respectively. A three-dimensional mesh was generated with 12479 nodes and 69784 tetrahedrons with local mesh refinement in a truncated cone. The usefulness of such concentric sphere models for electromagnetic applications was assessed by Roth *et al.* [29] by creating realistically shaped scalp, skull and brain models independently to calculate the electric potential produced by a dipole located in the temporal and frontal lobes of the brain. These realistic head model components could then be compared to a concentric sphere model as used by Thevenet *et al*. The purpose for this head modeling was the convenience of representing EEG activity sources as dipoles within the brain. The temporal and frontal lobes were specifically chosen due to the association of epileptic spikes in these particular regions. The calculated potentials were then used in an inverse calculation for the spherical model to predict the dipole position, orientation and strength. The geometry of the scalp, skull and brain were created with structural images obtained from a 1.5 T MRI scanner and coronal slices with 2 mm separation. Limitations of the approach used by Roth *et al.* were: firstly digitization of the data being performed visually rather than automatically segmenting the head regions, and secondly the realistic model approximated the brain surface to be equivalent to that of the inner surface of the skull. Due to computational limitations at the time of publication,

only certain subsets of the digitized model were used for numerical calculations resulting in an average triangle area of 73, 56 and 40 mm^2, respectively. On average, the dipole positions differed by 19.7 mm, with some results indicating a 40 mm difference, a clear demonstration that the concentric sphere model can produce large errors in the determination of the source of a dipole or the potentials generated by it.

Yuan *et al.* [30] developed a brain model for the same EEG application as Thevenet *et al.* [28] and Roth *et al.* [29], but with the desire for increased resolution in the head model. This new study also had the significant advantage of being able to calculate potentials in the brain incorporating anisotropic elements in the model. The method required special techniques to form a symmetrical stiffness matrix for use in the finite element calculation. A realistic head model composed of 73,296 elements was developed using a similar method to Roth *et al.*, as previously described. This study implemented a two-layer model comprising the skull and CSF region inside. The conductivity of the skull was specified as 0.0042 S/m for the normal direction relative to the surface and 0.042 S/m for the tangential direction. The conductivity of the CSF region was specified as 0.5 S/m in all directions (isotropic). The increased resolution of the mesh and the incorporation of anisotropic conductors allowed results to be produced with greater accuracy, although limiting the model to two regions was a severe limitation with significant detrimental effect on the calculation result.

Yao *et al.* [31] also developed an improved realistic head model for determining the active sites of the brain recorded by EEG apparatus by means of modeling equivalent sources in the human head with the finite element method. The resulting model contained 2,729 nodes and 5,446 triangular elements representing the scalp, skull and brain.

2.2.2 Human head modeling for transcranial magnetic stimulation

Wagner *et al.* [32] describe the use of three-dimensional head modeling specifically for the purpose of TMS. The model was used to determine the induced current density in realistic human head models exposed to transient magnetic field generated by external sources, such as TMS coils. The dielectric constants used in the simulations were varied to assess the effect upon the calculated electric current density. Current density was also calculated throughout the various tissue layers to determine if the tissue boundaries have a significant effect on the distribution of induced currents. The study showed that the magnitude of current density correlated to the electrical conductivity of the tissues unless the permittivity was significantly raised. Under these circumstances, displacement currents can arise making the permittivity of the tissue a more dominant factor in the calculation of current density. Wagner *et al.* [32] identified that many previous studies conclude that neurons which lie parallel to the cortical tissue interface are preferentially stimulated and that fields normal to the cortical surface are minimized in the human head. These conclusions were based upon studies involving simplified head models such as spherical isotropic conductors. Previous studies have also asserted that tissue boundary layers that surround the cortex have little influence on the field that stimulates the cortex. Wagner *et al.* dispute this assumption and state that removing tissues from a head model will result in inaccurate results, citing that the CSF has a conductivity approximately 5 times larger than the surrounding tissues.

The study by Wagner *et al.* focused on four primary areas. Firstly, investigation of how tissue boundaries can affect the induced current densities. Secondly, analysis of

conclusions drawn from earlier studies that made use of symmetric models. Thirdly, investigation of the effect of tissue geometry on resulting current distributions and lastly, to develop a head model which accounts for dispersive properties of tissues in a human head and how these can affect induced current. Wagner *et al.* [32] developed a new head model based upon MRI data of a 38-year-old male with a healthy brain, generating a model with a voxel size of 1 mm^3. The MRI data was segmented into five tissues; skin, skull, CSF, grey matter and white matter. The authors found the thickness of tissue layers varied significantly with anatomical position, identifying a severe limitation of the simplified concentric sphere head models that had been used in earlier investigations, as previously described. The mean values for tissue properties were obtained from a variety of sources resulting in conductivities of 0.465, 0.010, 1.654, 0.276, and 0.126 S/m for skin, skull, CSF, grey matter, and white matter, respectively. The model incorporated a figure-8 coil with 35 mm radii windings composed of a single turn of copper wire having radius of 7 mm.

Yang *et al.* [33] identified the need for increased localization of stimulation to develop the use of TMS beyond brain mapping, treatment of mood disorder, and associated medical problems. They indicated the need for realistic head models to achieve this goal due to the difficulty in estimating sites of stimulation. Previously, the determination of stimulated sites was achieved experimentally, reducing the efficiency of the procedure. Yang *et al.* indicate much of the TMS research continues to be done in free space and describe the need for head modeling due to differences in the properties of tissue having an effect upon the electric field and eddy current distribution in the head.

The complex geometry and tissue properties within the human head make analytical solutions difficult to achieve. Numerical methods such as such as finite element analysis can be utilized but improved realistic models are still required. Yang *et al.* [33] developed a new head model with greater complexity than previous investigations. The resulting three-dimensional model consisted of 420,875 nodes and 315,190 elements, containing scalp, skull, CSF, and the brain. Calculations were performed for a figure-8 coil placed over the vertex of the head, with 6 turns and inner radii 22.5 mm. The results of the study with the new head model showed that the field intensity decreased with distance from the coil but also that the stimulation range became wider with distance from the coil. This is indicative of the challenges posed in trying to stimulate below the cortical surface.

Sekino *et al.* [34] perform numerical simulations of eddy currents induced by TMS using another head model to study eddy currents induced in the cerebellum. The stimulating coils modeled had a diameter of 110 mm and current of 44.2 kA turns, generating a field of 0.56 T at the center of the coil. The largest current density calculated in the cerebellum was 2.9 A/m^2. The maximum depth at which an eddy current was predicted to be induced was 10 mm below the surface of the cerebellum but as indicated in other studies, currents at this depth are unlikely to be of sufficient magnitude to cause depolarization of neural cell membranes, or resulting neural stimulation. The authors stated their objective to build upon earlier work by determining intensity and localization of induced eddy currents in the cerebellum. The main goal of the investigation was to study the effect of tissue depth upon the localization of stimulation. The cerebellum is an adequate choice of brain region for this purpose as the average distance between it and a

TMS stimulator coil is likely to be 30 or 40 mm whereas the distance between a TMS stimulator coil and the cerebrum can be less than 20 mm [34]. Sekino *et al.* utilized a three-dimensional model developed by the Brooks Air Force Laboratory. This was the first model to use a significant number of tissue structures but was implemented with a spatial resolution of only 3 mm. The original model had a spatial resolution of 1 mm but the computational time required to use the highest resolution was found to be impractical by the authors at the time of the study. In total, the model was segmented into 24 distinct tissues, allowing an improved finite element result to be obtained with 189,975 nodes and 177,649 elements. The tissue properties for this study were obtained from Gabriel *et al.* [35]–[37], which are still widely used. To improve the accuracy of the model a realistic monophasic waveform was simulated with a duration of 1 ms. The coil was positioned 40 mm left of the inion, where the inion connects to the left mastoid. The field produced was calculated with the Biot-Savart law as described in the next chapter. Each coil was segmented into 72 elements and the calculation performed for each. The eddy current distribution was calculated by solving (2.1).

$$\nabla^2 P = \sigma \frac{\delta B(r,t)}{\delta t} \tag{2.1}$$

Datta *et al.* [38] used a similar methodology to calculate the electric fields produced by tDCS devices. Values for conductivity chosen were 0.2, 1.65, 0.01, and 0.465 S/m for the brain, CSF, skull, and skin, respectively. The model generated for this study had improved neural geometry compared to realistic models previously described, having greater geometric detail at the cortical gyri/sulci level, although the authors identity the model could be further improved by consideration of the differences in the tissue properties of the grey and white brain matter [38].

Effects on the induced electric field in the brain due to geometrical head model data, conductivity parameters and stimulation position was studied by Kim *et al.* [39]. This investigation made use of a head model developed by Zubal *et al.* [40] featuring increased resolution from which Kim *et al.* segmented seven tissues; skin, skull, CSF, gray matter, white matter, cerebellum, and cerebral ventricle, with conductivities of 0.33, 0.042, 1.79, 0.4, 0.2, 0.33, and 1.79 S/m, respectively. In addition to performing simulations of the induced electric field, a head phantom based upon the Zubal data was constructed from acrylic, with each of the seven regions represented. Varying electrical conductivities were achieved by adding the appropriate amount of sodium chloride to distilled water [39]. Experimental results with the head phantom were used to verify simulated results. Chen and Mogul [41] furthered developments in realistic head models by creating a model from multiple modality images. The major development in head model complexity in this study was the incorporation of microstructure detail via neocortical columnar structures. Miranda *et al.* [42] performed further studies into the effect of tissue heterogeneity and anisotropy upon induced electric field distribution, finding heterogeneity and anisotropy can introduce radial components to the induced electric field which is not observed when using isotropic conductors for head models.

A number of the head models described are depicted in Figure 2.1. A challenging aspect of performing the calculation of induced electric field or current density is determining the dielectric tissue properties, electrical conductivity and relative permittivity. Generally, permittivity increases with lower frequencies but consensus on values appropriate for TMS have previously not been established with a very wide range of suggested values between 10^2 and 10^7 for the TMS frequency spectrum.

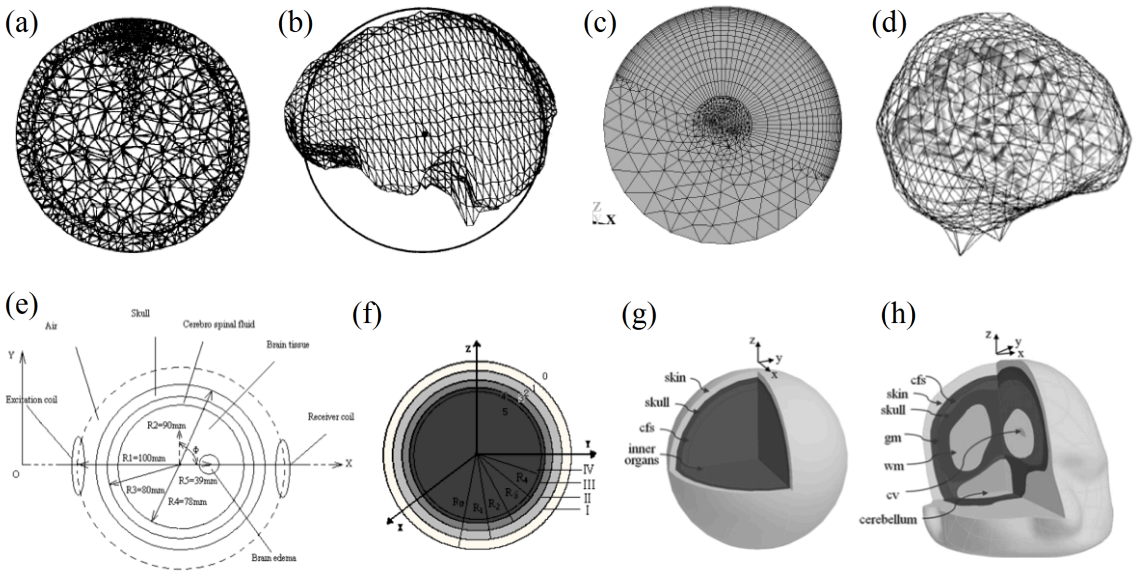

Figure 2.1. Head models utilized for electromagnetic modeling as used by (a) Thevenet *et al.* (1992), (b) Roth *et al.* (1993), (c) Miranda *et al.* (2003), (d) Im *et al.* (2003), (e) Ming-Xin *et al.* (2005), (f) Pu *et al.* (2009), and (g-h) Kim *et al.* (2009).

References

[1] A. T. Barker, R. Jalinous, and I. L. Freeston, "Non-invasive magnetic stimulation of human motor cortex," *Lancet*, vol. 325, no. 8437, pp. 1106–1107, 1985.

[2] R. Jalinous, "Guide to magnetic stimulation," *The MagStim Company, Whitland, Wales*, 1998.

[3] S. Ueno, T. Tashiro, and K. Harada, "Localized stimulation of neural tissues in the brain by means of a paired configuration of time-varying magnetic fields," *J. Appl. Phys.*, vol. 64, no. 10, pp. 5862–5864, 1988.

[4] P. J. Maccabee, L. Eberle, V. E. Amassian, R. Q. Cracco, and A. Rudell, "Spatial distribution of the electric field induced in volume by round and figure '8'magnetic coils: relevance to activation of sensory nerve fibers," *Electroencephalogr. Clin. Neurophysiol.*, vol. 76, no. 2, pp. 131–141, 1990.

[5] L. G. Cohen, B. J. Roth, J. Nilsson, N. Dang, M. Panizza, S. Bandinelli, W. Friauf, and M. Hallett, "Effects of coil design on delivery of focal magnetic stimulation.

Technical considerations," *Electroencephalogr. Clin. Neurophysiol.*, vol. 75, no. 4, pp. 350–357, 1990.

[6] D. S. Stokic, W. B. McKay, L. Scott, A. M. Sherwood, and M. R. Dimitrijevic, "Intracortical inhibition of lower limb motor-evoked potentials after paired transcranial magnetic stimulation," *Exp. brain Res.*, vol. 117, no. 3, pp. 437–443, 1997.

[7] Y. Terao, Y. Ugawa, R. Hanajima, K. Machii, T. Furubayashi, H. Mochizuki, H. Enomoto, Y. Shiio, H. Uesugi, N. K. Iwata, and others, "Predominant activation of I1-waves from the leg motor area by transcranial magnetic stimulation," *Brain Res.*, vol. 859, no. 1, pp. 137–146, 2000.

[8] Y. Roth, A. Zangen, and M. Hallett, "A coil design for transcranial magnetic stimulation of deep brain regions," *J. Clin. Neurophysiol.*, vol. 19, no. 4, pp. 361–370, 2002.

[9] E. Wassermann, C. Epstein, and U. Ziemann, *Oxford handbook of transcranial stimulation*. Oxford University Press, 2008.

[10] Q. Ai, J. Li, M. Li, W. Jiang, and B. Wang, "A new transcranial magnetic stimulation coil design to improve the focality," in *Biomedical Engineering and Informatics (BMEI), 2010 3rd International Conference on*, 2010, vol. 4, pp. 1391–1395.

[11] T. Kato, M. Sekino, T. Matsuzaki, A. Nishikawa, Y. Saitoh, and H. Ohsaki, "Fabrication of a prototype magnetic stimulator equipped with eccentric spiral coils," in *Engineering in Medicine and Biology Society, EMBC, 2011 Annual International Conference of the IEEE*, 2011, pp. 1985–1988.

[12] D.-H. Kim, G. E. Georghiou, and C. Won, "Improved field localization in transcranial magnetic stimulation of the brain with the utilization of a conductive shield plate in the stimulator," *Biomed. Eng. IEEE Trans.*, vol. 53, no. 4, pp. 720–725, 2006.

[13] L. Hernandez-Garcia, T. Hall, L. Gomez, and E. Michielssen, "A numerically optimized active shield for improved transcranial magnetic stimulation targeting," *Brain Stimul.*, vol. 3, no. 4, pp. 218–225, 2010.

[14] M. Talebinejad and S. Musallam, "Effects of TMS coil geometry on stimulation specificity," in *Engineering in Medicine and Biology Society (EMBC), 2010 Annual International Conference of the IEEE*, 2010, pp. 1507–1510.

[15] J. Ruohonen, M. Ollikainen, V. Nikouline, J. Virtanen, and R. J. Ilmoniemi, "Coil design for real and sham transcranial magnetic stimulation," *Biomed. Eng. IEEE Trans.*, vol. 47, no. 2, pp. 145–148, 2000.

[16] D.-H. Kim, J. K. Sykulski, N. Loukaides, and G. E. Georghiou, "Numerical investigation of the electric field distribution induced in the brain by transcranial magnetic stimulation," *IEE Proceedings-Science, Meas. Technol.*, vol. 151, no. 6, pp. 479–483, 2004.

[17] K. R. Davey and M. Riehl, "Suppressing the surface field during transcranial magnetic stimulation," *Biomed. Eng. IEEE Trans.*, vol. 53, no. 2, pp. 190–194, 2006.

[18] Z.-D. Deng, A. V Peterchev, and S. H. Lisanby, "Coil design considerations for deep-brain transcranial magnetic stimulation (dTMS)," in *Engineering in Medicine and Biology Society, 2008. EMBS 2008. 30th Annual International Conference of the IEEE*, 2008, pp. 5675–5679.

[19] R. Salvador, P. C. Miranda, Y. Roth, and A. Zangen, "High permeability cores to optimize the stimulation of deeply located brain regions using transcranial magnetic stimulation," *Phys. Med. Biol.*, vol. 54, no. 10, p. 3113, 2009.

[20] C. M. Epstein and K. R. Davey, "Iron-core coils for transcranial magnetic stimulation," *J. Clin. Neurophysiol.*, vol. 19, no. 4, pp. 376–381, 2002.

[21] H. Eaton, "Electric field induced in a spherical volume conductor from arbitrary coils: application to magnetic stimulation and MEG," *Med. Biol. Eng. Comput.*, vol. 30, no. 4, pp. 433–440, 1992.

[22] P. S. Tofts, "The distribution of induced currents in magnetic stimulation of the nervous system," *Phys. Med. Biol.*, vol. 35, no. 8, p. 1119, 1990.

[23] P. S. Tofts and N. M. Branston, "The measurement of electric field, and the influence of surface charge, in magnetic stimulation," *Electroencephalogr. Clin. Neurophysiol. Potentials Sect.*, vol. 81, no. 3, pp. 238–239, 1991.

[24] M. T. K. Kirkcaldie, S. A. Pridmore, and A. Pascual-Leone, "Transcranial magnetic stimulation as therapy for depression and other disorders," *Australas. Psychiatry*, vol. 31, no. 2, pp. 264–272, 1997.

[25] T. Kammer, S. Beck, A. Thielscher, U. Laubis-Herrmann, and H. Topka, "Motor thresholds in humans: a transcranial magnetic stimulation study comparing different pulse waveforms, current directions and stimulator types," *Clin. Neurophysiol.*, vol. 112, no. 2, pp. 250–258, 2001.

[26] A. Zangen, Y. Roth, B. Voller, and M. Hallett, "Transcranial magnetic stimulation of deep brain regions: evidence for efficacy of the H-coil," *Clin. Neurophysiol.*, vol. 116, no. 4, pp. 775–779, 2005.

[27] T. Fadini, L. Matthäus, H. Rothkegel, M. Sommer, F. Tergau, A. Schweikard, W. Paulus, and M. A. Nitsche, "H-coil: Induced electric field properties and input/output curves on healthy volunteers, comparison with a standard figure-of-eight coil," *Clin. Neurophysiol.*, vol. 120, no. 6, pp. 1174–1182, 2009.

[28] M. Thevenet, O. Bertrand, F. Perrin, and J. Pernier, "Finite element method for a realistic head model of electrical brain activities," in *Engineering in Medicine and Biology Society, 1992 14th Annual International Conference of the IEEE*, 1992, vol. 5, pp. 2024–2025.

[29] B. J. Roth, M. Balish, A. Gorbach, and S. Sato, "How well does a three-sphere model predict positions of dipoles in a realistically shaped head?," *Electroencephalogr. Clin. Neurophysiol.*, vol. 87, no. 4, pp. 175–184, 1993.

[30] J. Yuan and Z. Tang, "Finite-element simulation of human brain electric activity," *Magn. IEEE Trans.*, vol. 39, no. 3, pp. 1539–1542, 2003.

[31] Y. Yao, S. Zhu, and B. He, "A fast method to derive realistic FEM models based on BEM models.," in *Conference proceedings:... Annual International Conference of the IEEE Engineering in Medicine and Biology Society. IEEE Engineering in Medicine and Biology Society. Conference*, 2004, vol. 2, pp. 1575–1577.

[32] T. A. Wagner, M. Zahn, A. J. Grodzinsky, and A. Pascual-Leone, "Three-dimensional head model simulation of transcranial magnetic stimulation," *Biomed. Eng. IEEE Trans.*, vol. 51, no. 9, pp. 1586–1598, 2004.

[33] S. Yang, G. Xu, L. Wang, Y. Chen, H. Wu, Y. Li, and Q. Yang, "3D realistic head model simulation based on transcranial magnetic stimulation," in *Conf Proc IEEE Eng Med Biol Soc*, 2006, pp. 6469–6472.

[34] M. Sekino, M. Hirata, K. Sakihara, S. Yorifuji, and S. Ueno, "Intensity and localization of eddy currents in transcranial magnetic stimulation to the cerebellum," *Magn. IEEE Trans.*, vol. 42, no. 10, pp. 3575–3577, 2006.

[35] C. Gabriel, S. Gabriel, and E. Corthout, "The dielectric properties of biological tissues: I. Literature survey," *Phys. Med. Biol.*, vol. 41, no. 11, p. 2231, 1996.

[36] S. Gabriel, R. W. Lau, and C. Gabriel, "The dielectric properties of biological tissues: II. Measurements in the frequency range 10 Hz to 20 GHz," *Phys. Med. Biol.*, vol. 41, no. 11, p. 2251, 1996.

[37] S. Gabriel, R. W. Lau, and C. Gabriel, "The dielectric properties of biological tissues: III. Parametric models for the dielectric spectrum of tissues," *Phys. Med. Biol.*, vol. 41, no. 11, p. 2271, 1996.

[38] A. Datta, M. Elwassif, and M. Bikson, "Electrical Stimulation of Brain using a realistic 3D Human Head Model: Improvement of Spatial Focality," in *Excerpt from the Proceedings of the COMSOL Conference*, 2008.

[39] D.-H. Kim, N.-S. Choi, C. Won, and G. E. Georghiou, "Distortion of the electric field distribution induced in the brain during transcranial magnetic stimulation," *IET Sci. Meas. Technol.*, vol. 4, no. 1, pp. 12–20, 2010.

[40] I. G. Zubal, C. R. Harrell, E. O. Smith, Z. Rattner, G. Gindi, and P. B. Hoffer, "Computerized three-dimensional segmented human anatomy," *Med. Phys.*, vol. 21, no. 2, pp. 299–302, 1994.

[41] M. Chen and D. J. Mogul, "Using increased structural detail of the cortex to improve the accuracy of modeling the effects of transcranial magnetic stimulation on neocortical activation," *Biomed. Eng. IEEE Trans.*, vol. 57, no. 5, pp. 1216–1226, 2010.

[42] P. C. Miranda, M. Hallett, and P. J. Basser, "The electric field induced in the brain by magnetic stimulation: a 3-D finite-element analysis of the effect of tissue heterogeneity and anisotropy," *Biomed. Eng. IEEE Trans.*, vol. 50, no. 9, pp. 1074–1085, 2003.

CHAPTER III

ELECTROMAGNETIC THEORY

3.1 Analytic calculation of induced electric field

The electric field induced in the brain can be calculated analytically if certain constraints are imposed on the calculation. The electric field around a current path can be determined as shown in (3.1).

$$\oint \vec{E} \cdot dl = -\iint \frac{dB}{dt} \cdot ds \tag{3.1}$$

Assuming the induced electric field will form a circular path and that a uniform magnetic flux density is produced by the stimulator coil (3.2) and (3.3) can be asserted.

$$2\pi rE = \pi r^2 \frac{dB}{dt} \tag{3.2}$$

$$E = \frac{r}{2}\frac{dB}{dt} \tag{3.3}$$

The magnetic flux density due to a sinusoidal current pulse can be calculated by (3.4).

$$B = B_0 \sin\left(\frac{2\pi}{\tau}t\right) \tag{3.4}$$

Substituting the derivative of (3.4) into (3.3) yields the induced electric field as shown in (3.5).

$$E = \frac{r}{2}\left(\frac{2\pi}{\tau}\right)B_0 \cos\left(\frac{2\pi}{\tau}t\right) \tag{3.5}$$

If we assume a pulse duration of 400 μs, an induced current path length of 0.01 m, and a magnetic flux density produced by the coil of 1 T, then the induced electric field will be 78.5 V/m. This method requires various assumptions and highlights that in order to

obtain detailed information of the distribution of electric field in the brain, numerical methods need to be employed because analytic solutions only exist for the most simplified cases.

Similar calculations can be performed to calculate other quantities relating to how the tissue responds to the presence of the magnetic field produced by the TMS coil. Using the electric field calculated in (3.5) the induced current density can be calculated by the relation $J = \sigma E$. Assuming an electrical conductivity 1 S/m, a current density of 78.5 A/m^2 can be calculated. Charge density can also be derived from the relation $Q = J\Delta t$ yielding 3.925 mC/m^2.

A quantity that is often useful to consider in studies of electromagnetic radiation and biological tissue is the specific absorption rate (SAR). The energy dissipated by each pulse can be calculated by (3.6).

$$\frac{J^2}{2\sigma\rho}\tau \tag{3.6}$$

This yields a value of 0.616 mJ/kg. If a pulse repetition rate of 1 Hz is employed a SAR of 0.616 mW/kg will occur.

3.2 Numerical methods

Assuming the relations in (3.7) to (3.10),

$$\vec{B} = \mu\vec{H} \tag{3.7}$$

$$\vec{D} = \varepsilon\vec{E} \tag{3.8}$$

$$\vec{J}_m = \rho'\vec{H} \tag{3.9}$$

$$\vec{J}_e = \sigma \vec{E} \tag{3.10}$$

the time-dependent Maxwell's curl equations can be defined in differential form as shown in (3.11) and (3.12).

$$\frac{\delta \vec{H}}{\delta t} = -\frac{1}{\mu}\nabla \times \vec{E} - \frac{\rho'}{\mu}\vec{H} \tag{3.11}$$

$$\frac{\delta \vec{E}}{\delta t} = \frac{1}{\varepsilon}\nabla \times \vec{H} - \frac{\sigma}{\varepsilon}\vec{E} \tag{3.12}$$

The finite-difference time-domain (FDTD) formulation originally proposed by Yee [1] was initially intended to be used in isotropic, homogeneous media on a uniform grid, utilizing the central difference approximation. Second order accuracy is achieved using second order finite difference approximation for (3.11) and (3.12) for time and space.

$$\frac{\delta u}{\delta x}(i,j,k,n) = \frac{u^n_{i+\frac{1}{2},j,k} - u^n_{i-\frac{1}{2},j,k}}{\Delta x} + O\left[(\Delta x)^2\right] \tag{3.13}$$

$$\frac{\delta u}{\delta t}(i,j,k,n) = \frac{u^{n+\frac{1}{2}}_{i,j,k} - u^{n-\frac{1}{2}}_{i,j,k}}{\Delta t} + O\left[(\Delta t)^2\right] \tag{3.14}$$

The indices i, j and k indicate nodes in the spatial FDTD grid.

$$\frac{E_x\big|^{n+1}_{i,j,k} - E_x\big|^{n}_{i,j,k}}{\Delta t} = \frac{1}{\varepsilon_{i,j,k}}\left(\frac{H_z\big|^{n+\frac{1}{2}}_{i,j+\frac{1}{2},k} - H_z\big|^{n+\frac{1}{2}}_{i,j-\frac{1}{2},k}}{\Delta y} - \frac{H_y\big|^{n+\frac{1}{2}}_{i,j,k+\frac{1}{2}} - H_y\big|^{n+\frac{1}{2}}_{i,j,k-\frac{1}{2}}}{\Delta z} - \sigma_{i,j,k} E_x\big|^{n+\frac{1}{2}}_{i,j,k}\right) \tag{3.15}$$

The x-component of the electric field in (3.12) is determined in FDTD by the central difference method as shown in (3.16).

$$E_x\big|^{n+\frac{1}{2}}_{i,j,k} = \frac{E_x\big|^{n+1}_{i,j,k} + E_x\big|^{n}_{i,j,k}}{2} \tag{3.16}$$

Therefore, (3.15) can be written as,

$$E_x\Big|_{i,j,k}^{n+1} = \left(\frac{1-\frac{\Delta t\sigma_{i,j,k}}{2\varepsilon_{i,j,k}}}{1+\frac{\Delta t\sigma_{i,j,k}}{2\varepsilon_{i,j,k}}}\right) E_x\Big|_{i,j,k}^{n} + \left(\frac{\frac{\Delta t}{\varepsilon_{i,j,k}}}{1+\frac{\Delta t\sigma_{i,j,k}}{\varepsilon_{i,j,k}}}\right)\left(\frac{H_z\Big|_{i,j+\frac{1}{2},k}^{n+\frac{1}{2}} - H_z\Big|_{i,j-\frac{1}{2},k}^{n+\frac{1}{2}}}{\Delta y} - \frac{H_y\Big|_{i,j,k+\frac{1}{2}}^{n+\frac{1}{2}} - H_y\Big|_{i,j,k-\frac{1}{2}}^{n+\frac{1}{2}}}{\Delta z}\right) \tag{3.17}$$

This procedure allows Maxwell's curl equations to be discretized yielding explicit expressions for all components of magnetic and electric field. The stability of the method is defined by the Courant-Friedrichs-Lewy criterion as in (3.18) for the given increments.

$$\Delta t \le \frac{1}{c\sqrt{\frac{1}{(\Delta x)^2}+\frac{1}{(\Delta y)^2}+\frac{1}{(\Delta z)^2}}} \tag{3.18}$$

If a harmonic oscillation $e^{j\omega t}$ is assumed, Maxwell's curl equations can be transformed into the frequency domain. Assuming a quasi-static model, the magnetostatic vector potential can be calculated by the Biot-Savart law as shown in (3.19).

$$\vec{A}_0(\vec{r}) = \frac{\mu_0}{4\pi}\int_\Omega \frac{\vec{J}_0(\vec{r}\,')}{|\vec{r}-\vec{r}\,'|}d\vec{r}\,' \tag{3.19}$$

The vector potential **A** is decoupled from the electric field **E**, which is calculated by (3.20),

$$\vec{E} = -j\omega\vec{A} + \nabla\phi = \vec{E}_s + \vec{E}_i \tag{3.20}$$

where $\nabla\cdot\mathbf{E}_s = 0$ (solenoidal) and $\nabla\cdot\mathbf{E}_i$ (irrotational). A magneto-quasi-static method can be implemented as shown in (3.21).

$$\nabla\cdot\sigma\nabla\phi = j\omega\nabla\cdot(\sigma\vec{A}_0) \tag{3.21}$$

Such an implementation is used in the low-frequency solver in SEMCAD X electromagnetic simulation software (Schmid & Partner Engineering AG, Zurich, Switzerland), which is utilized in the following studies.

References

[1] K. S. Yee and others, "Numerical solution of initial boundary value problems involving Maxwell's equations in isotropic media," *IEEE Trans. Antennas Propag*, vol. 14, no. 3, pp. 302–307, 1966.

CHAPTER IV

RESULTS I: ANATOMICALLY REALISTIC HUMAN HEAD MODELING

4.1 Effect of head model complexity

The majority of previous electromagnetic studies of TMS have utilized simplified human head models, although some increase in complexity has been observed in more recent years. Effective modeling of TMS allows researchers to determine the locus of stimulation and can ultimately be used to aid in the development of new TMS coils by identifying the advantages novel coil designs offer.

The effect of head model complexity has been investigated to determine the necessity of anatomically realistic head models and the extent to which inhomogeneous models affect the calculated electric field induced in the brain during TMS. Initially, three three-dimensional human head models of varying complexity have been considered.

The most primitive model, which is prevalent in earlier literature but still often utilized, consists of a homogeneous sphere as shown in Figure 4.1 (a). In this study the radius of the sphere is assumed to be 100 mm. In addition to the spherical head model, a homogeneous volume with the external dimensions and features of a human head, the standard anthropomorphic model (SAM), will also be used, Figure 4.1 (b). Finally, an anatomically realistic human head model, derived from structural MRI data of a 34-year-old adult male has been employed, originally part of the Virtual Family Project dataset [1], Figure 4.1 (c). The advantage of a realistic model is the ability to independently apply tissue properties for each distinct tissue type that has been segmented in the head

model. This ability is significant as some neighboring tissues in the head can have electrical conductivity values that differ by more than an order of magnitude.

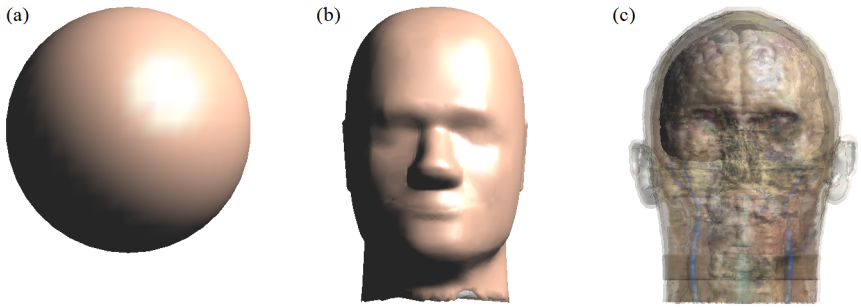

Figure 4.1. Three-dimensional human head models, (a) homogeneous sphere, (b) homogeneous standard anthropomorphic model, and (c) inhomogeneous anatomically realistic human head model derived from structural MRI data of an adult male.

For the purposes of this study, dielectric tissue values have been calculated from the IT'IS material parameter database [2]. The database is based upon a survey of all relevant literature on the subject of tissue parameters, which has been periodically updated since its inception in 2011, with the most recent version 2.5 being released on August 1st 2014. The studies described in this text make use of parameters from this most recent version unless otherwise stated. A sample of dielectric properties obtained from the database for the main tissues of the head are shown in Table 4.1.

Table 4.1. Values of dielectric tissue properties at 2.5 kHz, obtained from IT'IS database [2].

Tissue	Relative Permittivity	Electrical Conductivity [S/m]
Brain (Grey Matter)	7.81×10^{4}	1.04×10^{-1}
Brain (White Matter)	3.43×10^{4}	6.45×10^{-2}
Cerebellum	7.84×10^{4}	1.24×10^{-1}
Cerebrospinal Fluid	1.09×10^{2}	2.00×10^{0}
Skin	1.14×10^{3}	2.00×10^{-4}
Skull	1.44×10^{3}	2.03×10^{-2}

The skin component of this data comprises the cellular epidermis and dermis but not the outermost stratum corneum that contains no excitable nerve endings. A complete list of utilized parameters can be found in the appendices of this text.

The method for solving the magnetic and electric fields implements a low-frequency solver, as described in Chapter 3. For each model the parameters relating to the stimulator coil remained the same. A sinusoidal magnetic flux density of 2.5 kHz and peak current of 5 kA were assumed. The solution domain consisted of 6.5, 7.2 and 6.1 million voxels for the spherical, SAM and inhomogeneous head models, respectively. The homogeneous spherical and SAM models were assigned an averaged electrical conductivity of 0.33 S/m and relative permeability and relative permittivity of 1 and 11000, respectively. A circular coil based upon a Magstim HP90 (R) coil and a figure-8 coil based upon a Magstim D70 (R) coil were both modeled for the purposes of this study. The circular coil comprised of 14 turns with internal radius 33.5 mm and external radius 62.5 mm. Both windings of the figure-8 coil comprised of 9 turns with internal radius 27.5 mm and external radius 47.5 mm.

To ensure valid field values were obtained, measurements of the magnetic field produced by the modeled figure-8 coil were conducted. A gaussmeter and axial Hall probe with an active component area of 0.46 mm^2, positioned by a multi-axis linear stage system with positioning accuracy of 0.6 μm was utilized. Axial magnetic field measurements were obtained along the coil length (x-axis) at distances of 20 and 50 mm (z-axis) from the figure-8 coil as shown in Figure 4.2. These distances were chosen as 20 mm is a depth at which neural stimulation is currently feasible in the head and 50 mm

represents a target depth for future TMS coil designs. For reference, the distance between scalp and cortical surface is typically 14.3 mm [3].

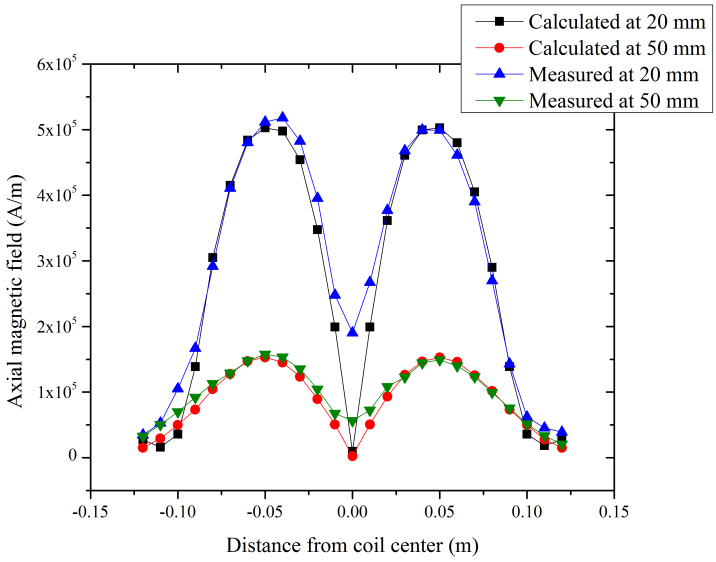

Figure 4.2. Measured and calculated axial magnetic field along coil length (x-axis) at 20 and 50 mm (z-axis) from Magstim D70 (R) coil at 100% stimulator output, energized with Magstim Rapid^2 stimulator.

At the distances concerned, the largest field intensities are observed at the center of each coil winding. At 20 mm this value reaches approximately 0.5 MA/m reducing to 0.15 MA/m at a distance of 50 mm. The results obtained through measurement and calculation of the magnetic field show good agreement. Based on this corroboration we can assume calculated results of electric field to also be valid, which provides a practical estimation of where stimulation is likely to occur in the brain.

The electric field needed to cause neural stimulation has been reported to be between 20 and 100 V/m [4]. The calculated magnetic and electric field induced in the medial coronal plane of each head model by the modeled circular coil is shown in Figure 4.3.

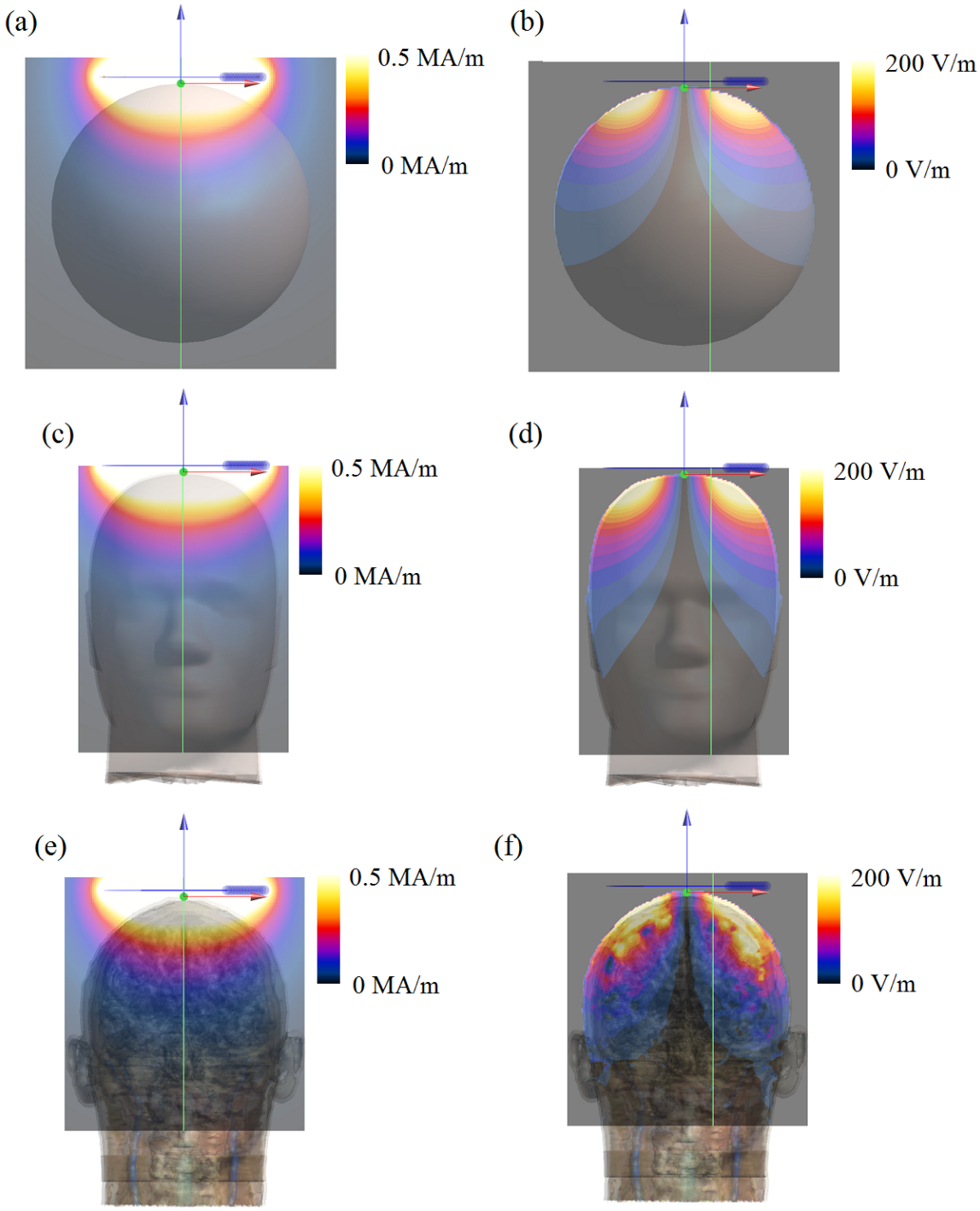

Figure 4.3. Calculated magnetic and electric field in the medial coronal plane of (a-b) homogeneous sphere, (c-d) homogeneous standard anthropomorphic model, and (e-f) inhomogeneous anatomically realistic human head model, with modeled circular coil.

Theoretically, the presence of the head should have no effect upon the magnetic field produced by the coil. This result is confirmed in Figure 4.4, which shows the magnetic field along the model z-axis, indicated by the green line in Figure 4.3 (a), (c), and (e), passing through the vertex of the head and the center of circular coil. In each case the head model has no effect on the magnetic field calculated inside the head. The figure shows that the magnetic field at the vertex of the head is approximately 0.7 MA/m, reducing to approximately 0.5 MA/m at a depth of 20 mm and 0.2 MA/m at a depth of 50 mm.

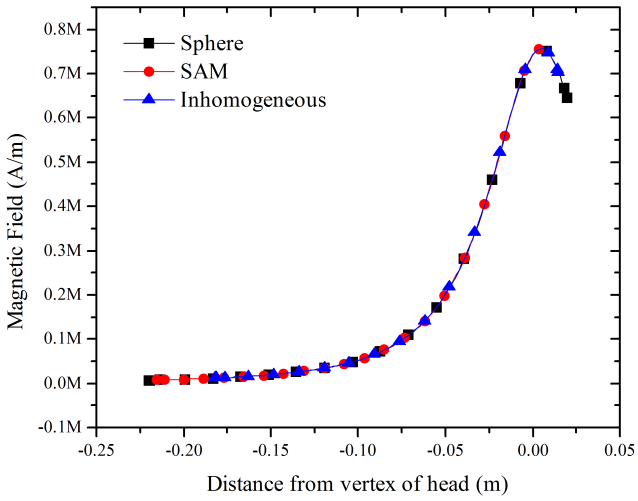

Figure 4.4. Calculated magnetic field along model z-axis, through vertex of the head in spherical, SAM and inhomogeneous head models with modeled circular coil.

The electric field induced in each head model, 20 mm off-axis, in the medial coronal plane, as indicated by the green line in Figure 4.3 (b), (d), and (f), is shown in Figure 4.5. The spherical and SAM head models show similar characteristics while the inhomogeneous head model shows variation in the induced electric field not observed in the homogeneous models. Each model induces an electric field above 150 V/m at the

surface of the head, reducing to between approximately 40 and 60 V/m at a depth of 50 mm.

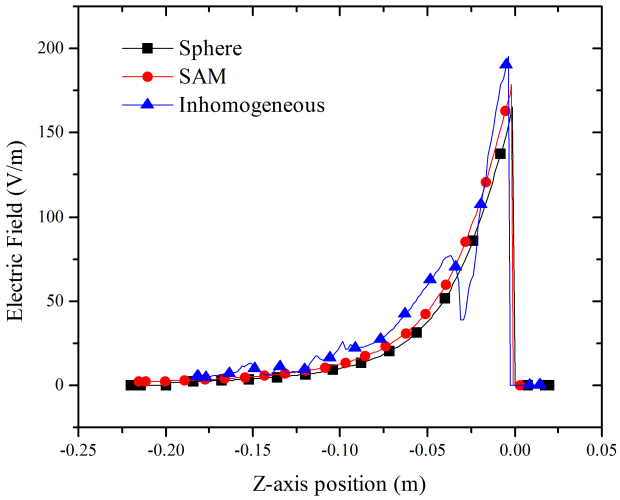

Figure 4.5. Calculated electric field induced 20 mm from z-axis origin, in spherical, SAM and inhomogeneous head models with circular coil.

The extent of this variation is more clearly demonstrated by comparing the electric field induced in transverse planes of the spherical and inhomogeneous head model as shown in Figure 4.6. At a distance of 10 mm the planes show a similar distribution of the induced electric field. At greater distances of 20 and 30 mm, significant changes in the distribution and magnitude of the electric field can be observed. This highlights the limitations of the simplified homogeneous model and indicates an inability of the homogeneous model to accurately determine the induced electric field at depth in the brain.

The distribution of magnetic flux density on the surface of the homogeneous SAM head model and on the surface of the skin, grey matter and white matter of the inhomogeneous head model are shown in Figure 4.7. The homogeneous SAM head

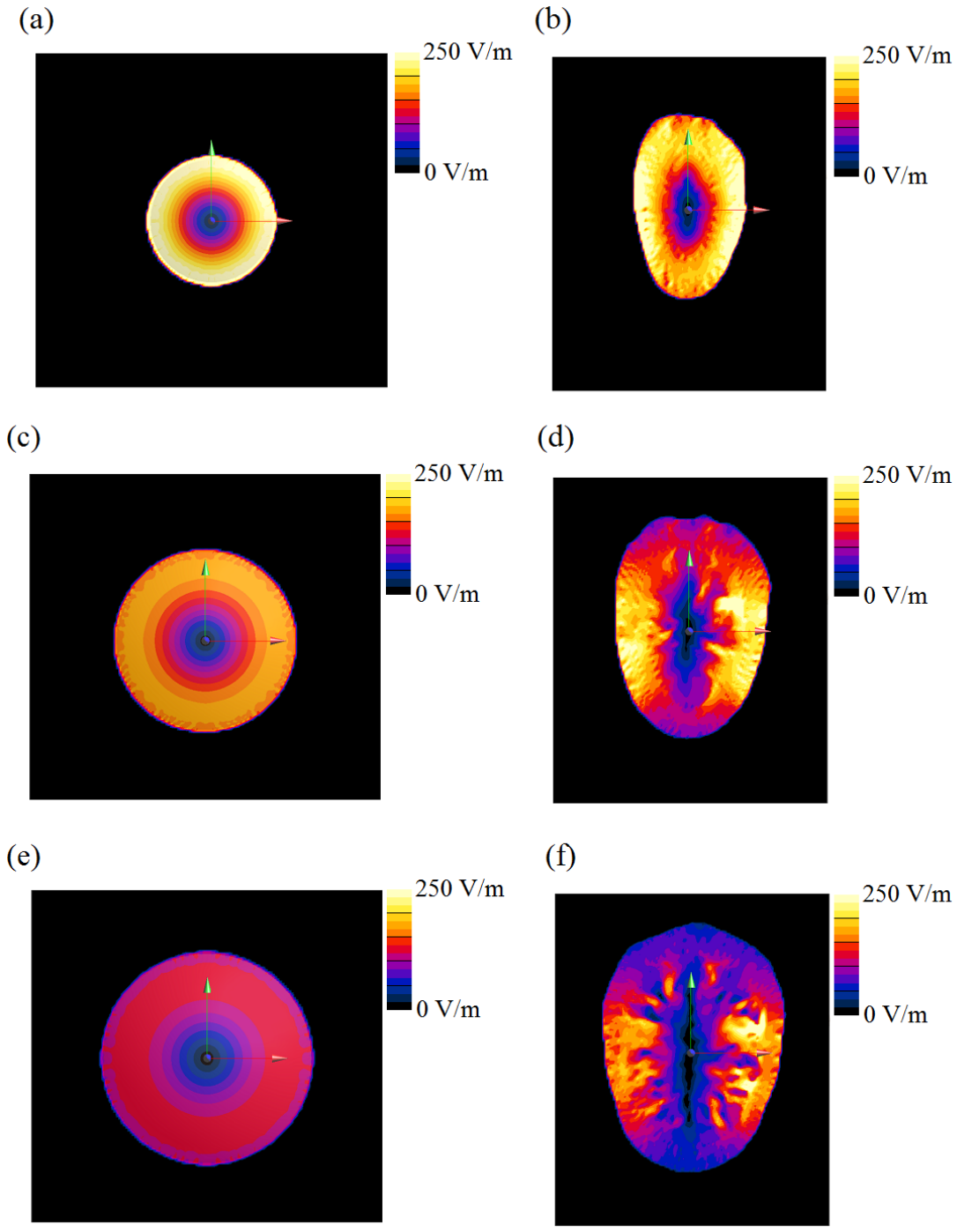

Figure 4.6. Induced electric field in transverse planes in (a) spherical and (b) inhomogeneous model 10 mm below the vertex, (c) spherical and (d) inhomogeneous model 20 mm below the vertex, and (e) spherical and (f) inhomogeneous model 30 mm below the vertex, induced by a modeled circular TMS coil.

model shows similar magnetic flux density distribution to the inhomogeneous model on the surface of the head but is unable to show the magnetic flux density distribution on the surface of the brain.

The distribution of electric field induced on the surface of the homogeneous SAM head model and on the surface of the skin, grey matter and white matter of the inhomogeneous model are shown in Figure 4.8. Again, the homogeneous SAM head model shows similar electric field distribution to the inhomogeneous model on the surface of the head but is unable to show the electric field distribution on the surface of the brain.

While circular coils are still often used for TMS, figure-8 coils are more prevalent due to their improved targeting capabilities. The calculated magnetic and electric field induced in the medial coronal plane of each head model by the modeled figure-8 coil is shown in Figure 4.9.

Results of the magnetic field generated by the figure-8 coil show that the magnetic field in all head models is the same and not influenced by the presence of a head model, as shown in Figure 4.10. The figure also shows that the magnetic field at the surface of the head is approximately 0.75 MA/m, reducing to approximately 0.3 MA/m at a depth of 20 mm and 0.1 MA/m at a depth of 50 mm.

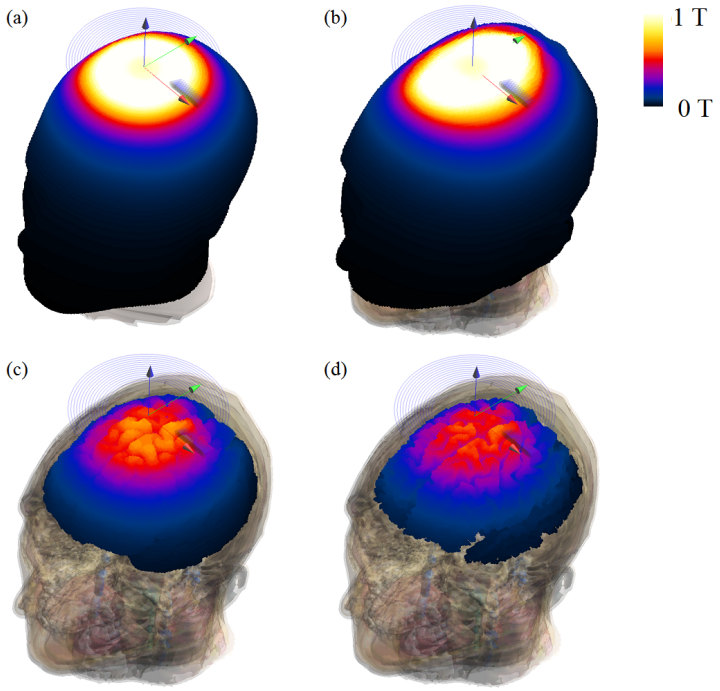

Figure 4.7. Calculated magnetic flux density on (a) surface of inhomogeneous SAM head model and surface of (b) skin, (c) grey matter, and (d) white matter of inhomogeneous head model with circular coil.

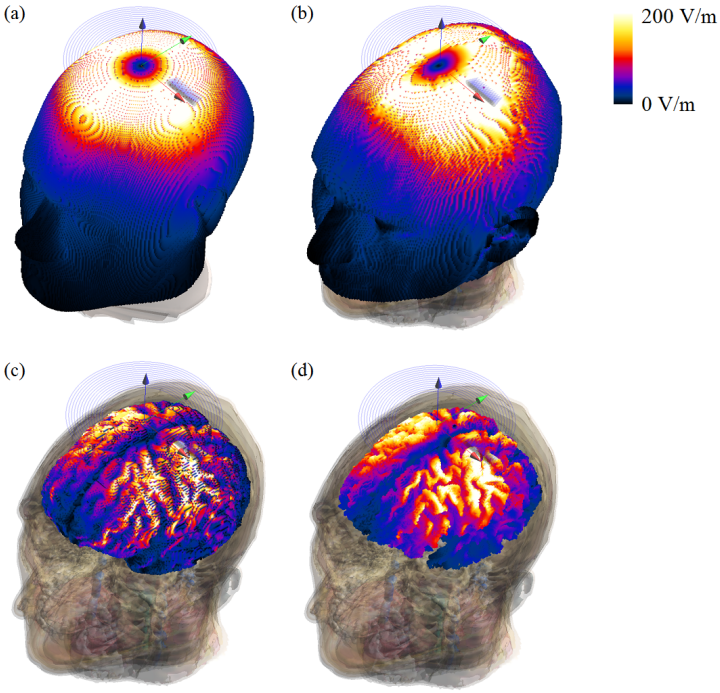

Figure 4.8. Calculated electric field induced on (a) surface of inhomogeneous SAM head model and surface of (b) skin, (c) grey matter, and (d) white matter of inhomogeneous head model with circular coil.

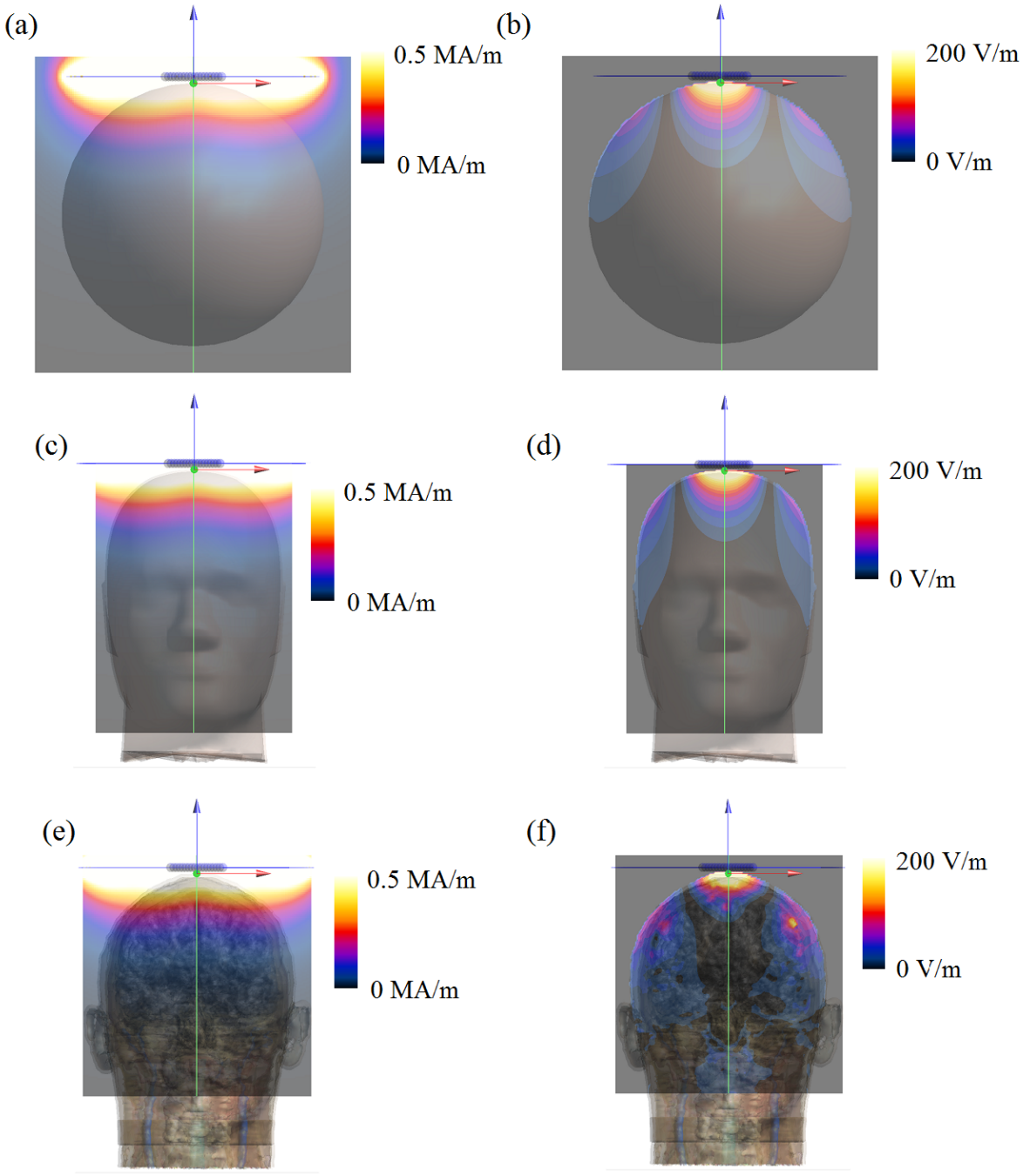

Figure 4.9. Calculated magnetic and electric field in the medial coronal plane of (a-b) homogeneous sphere, (c-d) homogeneous standard anthropomorphic model, and (e-f) inhomogeneous anatomically realistic human head model, with modeled figure-8 coil.

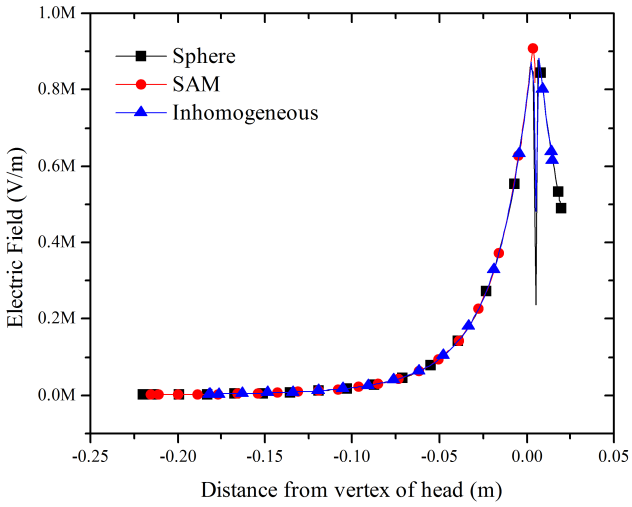

Figure 4.10. Calculated magnetic field along model z-axis through vertex of the head in spherical, SAM and inhomogeneous head models with modeled figure-8 coil.

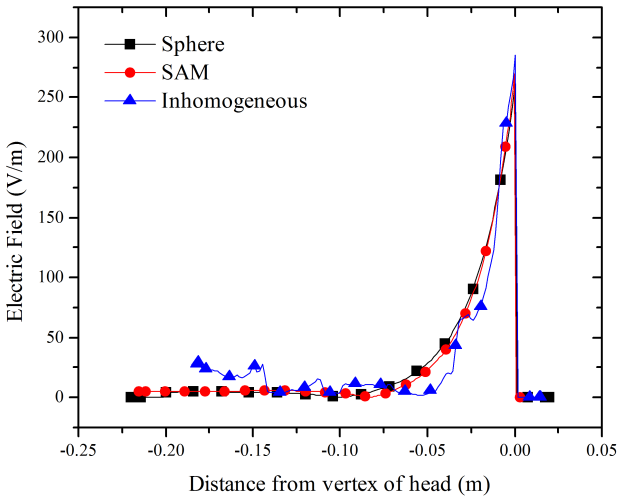

Figure 4.11. Calculated electric field induced along model z-axis through vertex of the head in spherical, SAM and inhomogeneous head models with modeled figure-8 coil.

The electric field induced along the model z-axis, passing through the vertex of each of the three models is shown in Figure 4.11. Again, the result of the two homogeneous models are very similar, with variation in the induced field observed in the

inhomogeneous model. For this coil, the electric field induced at the vertex of the head is over 250 V/m for each head model, reducing to less than 50 V/m at a depth of 50 mm.

The electric field induced in transverse planes 10, 20 and 30 mm below the vertex of the head for the spherical and inhomogeneous head models are shown in Figure 4.12. Near to the surface of the coil, at a distance of 10 mm, some similarities in the distribution of the induced electric field can be observed between the homogeneous sphere and inhomogeneous head models. As the distance is increased to 20 mm fewer similar features can be distinguished and at 30 mm only regions at the side of the plane, at the surface of the head, show similar electric field distribution. This supports the hypothesis that the simplified homogeneous models are unable to accurately model the induced electric field at depth in the brain.

The distribution of magnetic flux density on the surface of the homogeneous SAM head model and on the surface of the skin, grey matter and white matter of the inhomogeneous model with the modeled figure-8 coil are shown in Figure 4.13. As before, the homogeneous SAM head model shows similar magnetic flux density distribution to the inhomogeneous model on the surface of the head but is unable to show the magnetic field distribution on the surface of the brain.

The distribution of electric field induced on the surface of the homogeneous SAM head model and on the surface of the skin, grey matter and white matter of the inhomogeneous model are shown in Figure 4.14. Again, the homogeneous SAM head model shows similar electric field distribution to the inhomogeneous model on the surface of the head but is unable to show the magnetic field distribution on the surface of the brain.

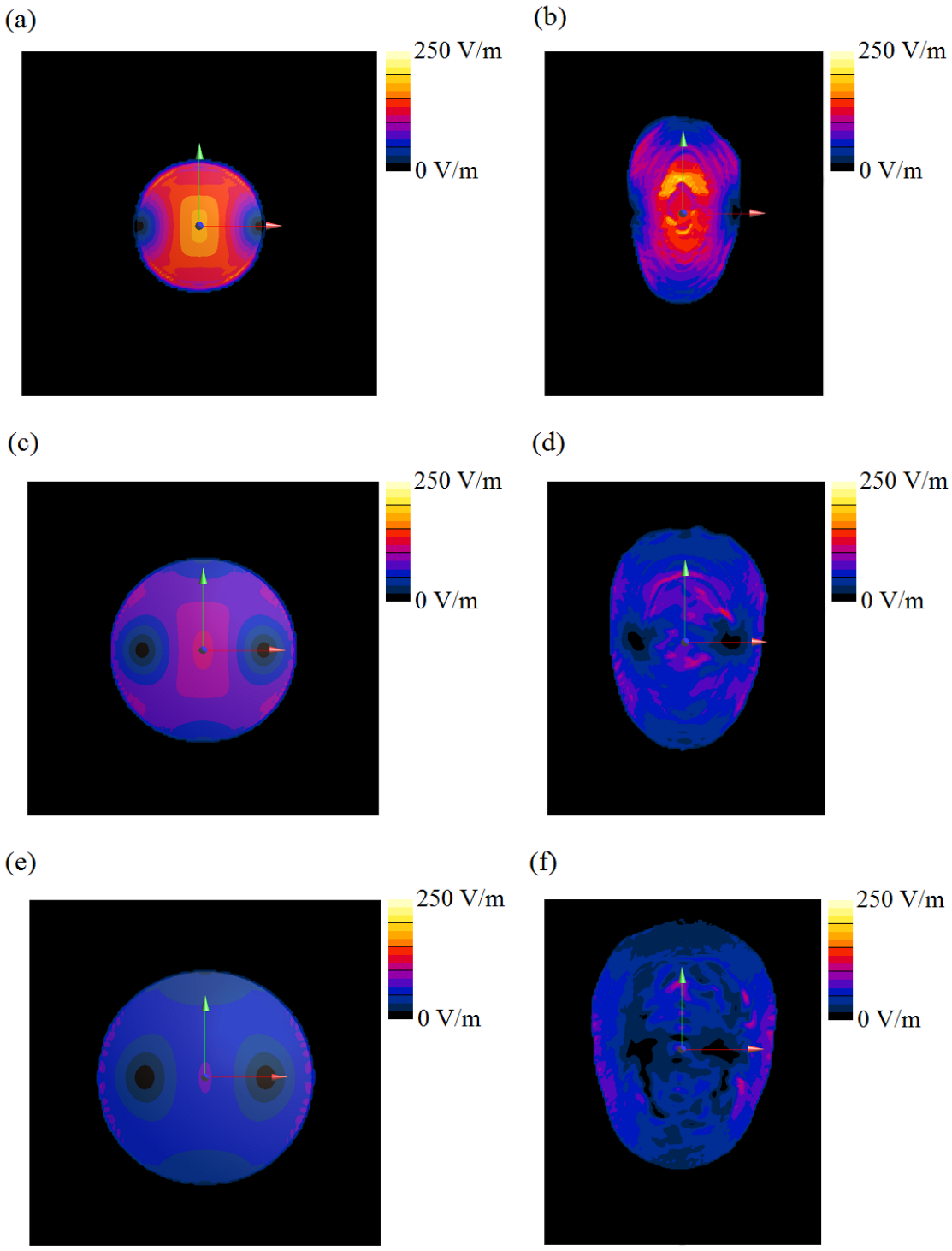

Figure 4.12. Induced electric field in transverse planes in (a) spherical and (b) inhomogeneous model 10 mm below the vertex, (c) spherical and (d) inhomogeneous model 20 mm below the vertex, and (e) spherical and (f) inhomogeneous model 30 mm below the vertex, induced by a modeled figure-8 TMS coil.

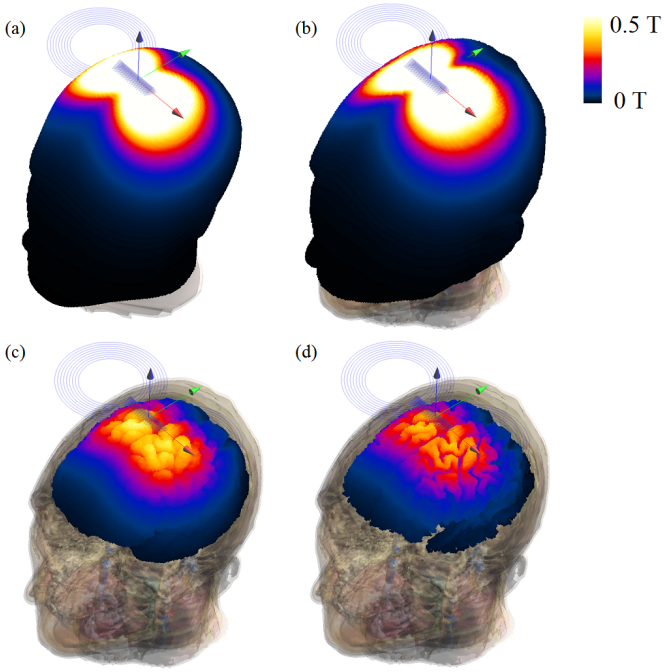

Figure 4.13. Calculated magnetic flux density on (a) surface of inhomogeneous SAM head model and surface of (b) skin, (c) grey matter, and (d) white matter of inhomogeneous head model with figure-8 coil.

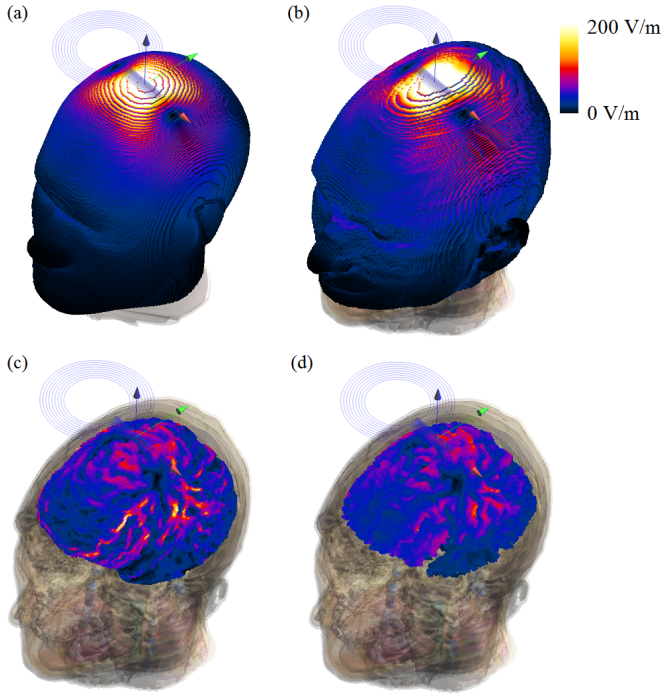

Figure 4.14. Calculated electric field induced on (a) surface of inhomogeneous SAM head model and surface of (b) skin, (c) grey matter, and (d) white matter of inhomogeneous head model with figure-8 coil.

The shortcomings of the homogeneous models at depth in the brain can be easily demonstrated by considering the induced electric field along the model x-axis at various distances from the coil surface. The electric field calculated 20 mm from the coil surface along the coil x-axis is shown in Figure 4.15. Generally it is anticipated that the maximum induced electric field will lie below the coil center, at x = 0. At 20 mm, the magnitude of the electric field in the inhomogeneous model is approximately 70% of the electric field calculated for the homogeneous models whereas the peaks at ± 50 mm are greater in the inhomogeneous case. This suggests the field at the surface of the head is greater than determined with a homogeneous model and attenuates more rapidly.

Figure 4.16 shows the calculated electric field at a distance of 50 mm along the coil x-axis. In this case we more clearly see the large difference between simplified and realistic head models. This disparity is sufficiently large enough to erroneously identify likely regions of neural stimulation during TMS.

The inhomogeneous model indicates the value of induced electric field at this depth below the vertex is well below the field required to generate an action potential and cause neural stimulation. However, the electric field values closer to the surface of the head at this distance from the coil are greatly increased, increasing the likelihood of having two stimulated sites with a spatial separation of 100 mm.

The theoretical calculations and empirical measurements exhibited demonstrate the impact of human head model complexity upon the calculation of electric field in the brain for neural stimulation. It is evident that tissue heterogeneity in the brain has a significant effect on the induced electric field. In general, it is observed that a simplified

homogeneous head model will overestimate the field intensity at depth in the brain and underestimate the field intensity at the surface.

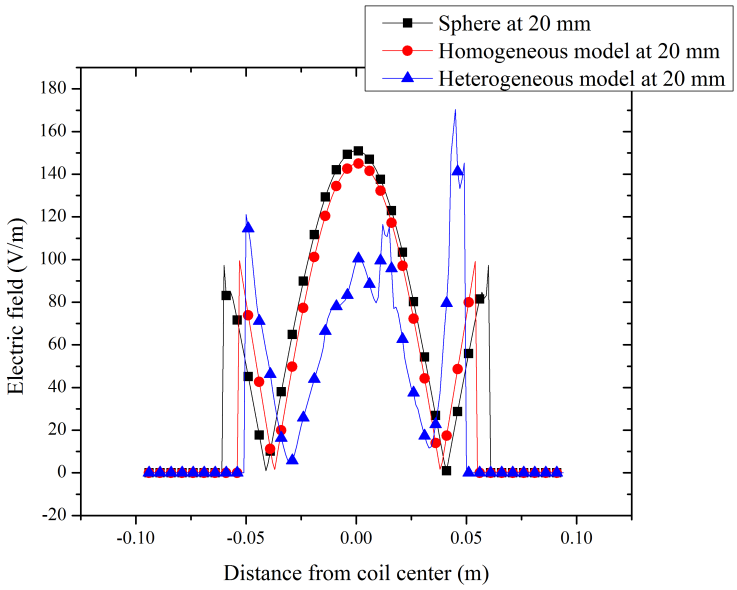

Figure 4.15. Calculated electric field profile 20 mm from coil surface for three human head models with figure-8 coil.

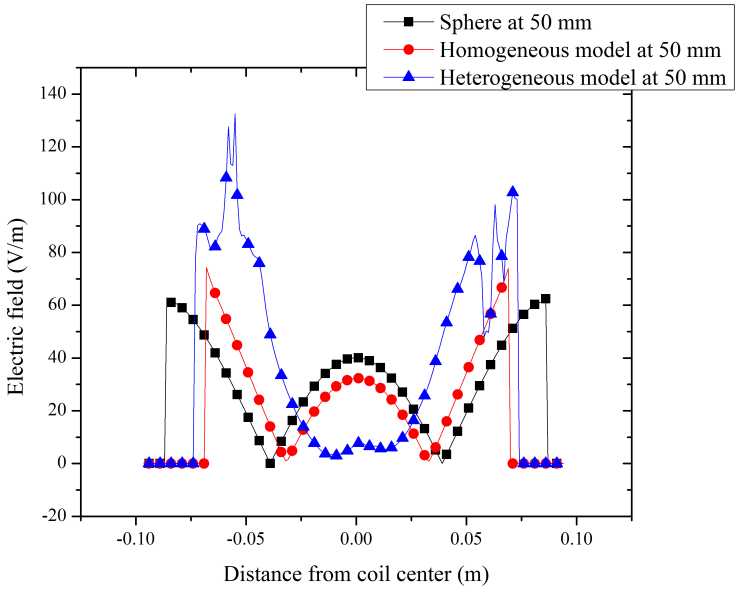

Figure 4.16. Calculated electric field profile 50 mm from coil surface for three human head models with figure-8 coil.

A point that arises from these results is that, as the physical characteristics of the brain of each TMS subject will vary, the spatial distribution of the induced electric field will also vary. As a result, one TMS coil may not accurately stimulate a desired cortical target for a variety of subjects. The results also highlight the necessity to implement realistic head models when assessing novel coil designs for TMS applications, or else accurate determination of stimulated sites cannot be asserted.

4.2 Grid resolution and model validation

The importance of grid resolution has been studied to establish if valid results are yielded by these calculations. A series of simulations have been performed with the inhomogeneous head model and modeled figure-8 coil with approximately 0.2, 0.5, 1, 2, 5, 10, and 20 million voxels in the solution domains. Model parameters and computational metrics are given in Table 4.2.

Table 4.2. Simulation duration and peak memory usage for solution domains of varying resolution.

Number of voxels (millions)	Grid dimensions	Simulation duration (hh:mm:ss)	Peak memory usage [MB]
0.20328	$55 \times 66 \times 56$	00:01:25	56.9570
0.50616	$74 \times 90 \times 76$	00:03:47	72.4688
1.00685	$92 \times 114 \times 96$	00:08:10	101.027
2.00448	$116 \times 144 \times 120$	00:17:16	160.121
5.06702	$157 \times 198 \times 163$	00:48:48	363.301
9.99600	$196 \times 250 \times 204$	01:44:04	739.797
20.4900	$248 \times 319 \times 259$	03:45:36	1575.14

The lowest resolution simulation had a grid size of 55 × 66 × 56 elements, approximately 0.2 million voxels, and required only 1 minute and 25 seconds to complete, utilizing just 56 MB of memory. The highest resolution simulation had a grid size of 248 × 319 × 259 elements, approximately 20 million voxels, and required 3 hours and 45 minutes to complete, utilizing over 1.5 GB of memory. A linear relationship was observed between the number of voxels in the solution domain and both the overall simulation duration and peak memory usage, as shown in Figure 4.17.

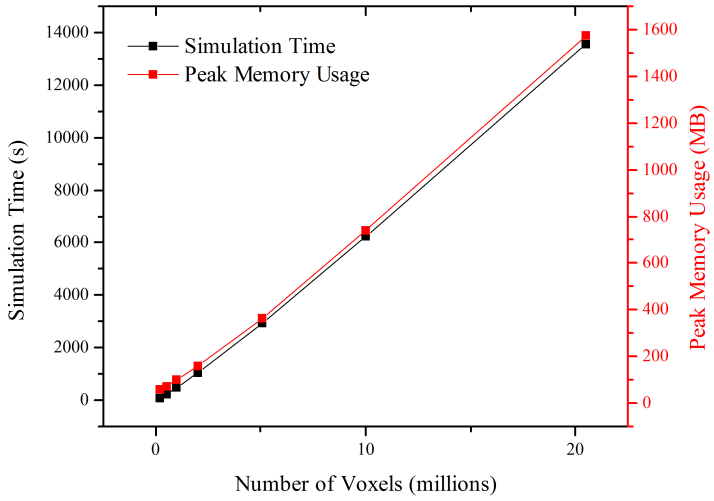

Figure 4.17. Simulation duration and peak memory usage for solution domains of varying resolution.

The magnetic field in the medial coronal plane for each simulation is shown in Figure 4.18. The coarseness of the grid and resulting calculated magnetic field distribution in the simulations with fewer voxels is visually evident, but increasingly difficult to distinguish as the grid resolution increases.

The electric field induced in the head model for each of these solutions is shown in Figure 4.19. It is evident that additional features are present in the solutions with a

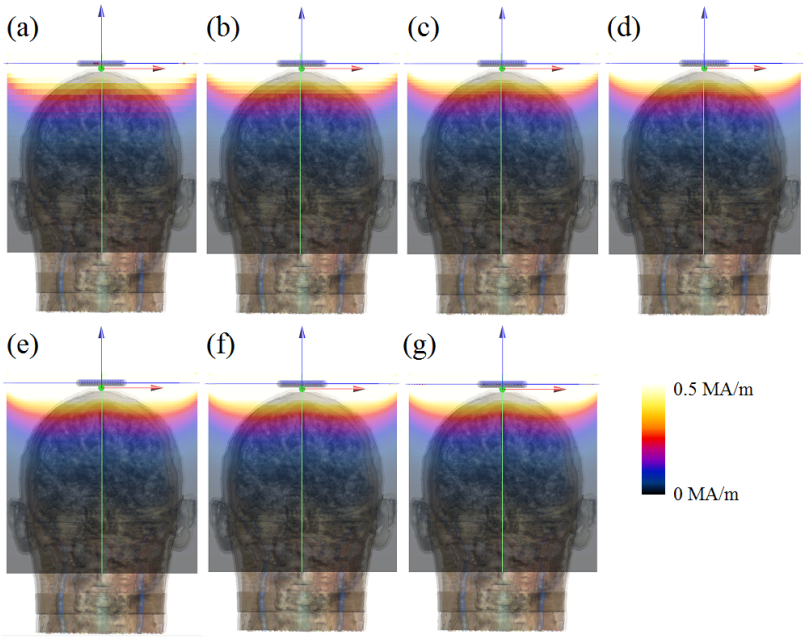

Figure 4.18. Calculated magnetic field produced by a modeled figure-8 coil in the medial coronal plane in solution domains consisting of (a) 0.20328, (b) 0.50616, (c) 1.00685, (d) 2.00448, (e) 5.06702, (f) 9.99600, and (g) 20.4900 million voxels.

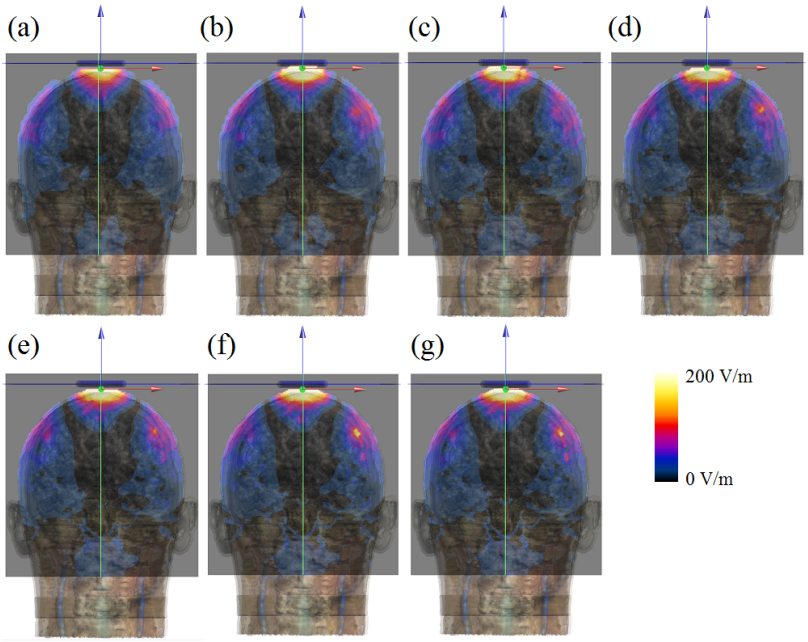

Figure 4.19. Calculated electric field induced in an inhomogeneous head model by a modeled figure-8 coil in the medial coronal plane in solution domains consisting of (a) 0.20328, (b) 0.50616, (c) 1.00685, (d) 2.00448, (e) 5.06702, (f) 9.99600, and (g) 20.4900 million voxels.

greater number of voxels, particularly the area of high field in the left hemisphere in the medial coronal plane.

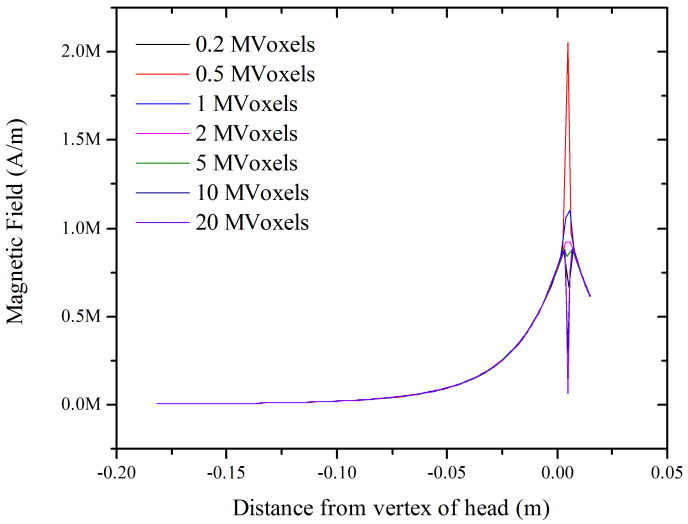

Figure 4.20. Calculated magnetic field along the model z-axis, in the medial coronal plane, passing through the vertex of the head, as indicated by the green lines in Figure 4.18.

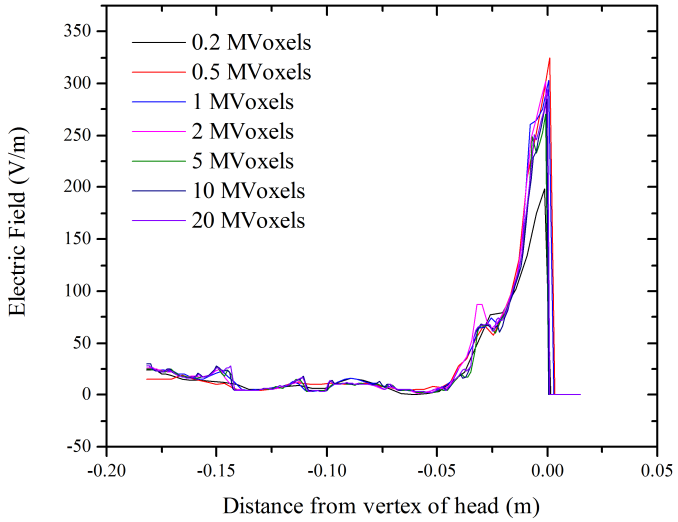

Figure 4.21. Calculated electric field induced in an inhomogeneous head model by a modeled figure-8 coil, along the model z-axis, in the medial coronal plane, passing through the vertex of the head, as indicated by the green lines in Figure 4.19.

The magnetic field calculated in the medial coronal planes, along the model z-axis, passing through the vertex of the head is shown in Figure 4.20. The difference in grid resolution has an effect on the magnetic field calculated in the locality of the coil windings but little effect on the magnetic field away from the coil, in the head region.

The electric field calculated in the medical coronal planes, along the model z-axis, passing through the vertex of the head is shown in Figure 4.21. Discernable differences can be identified between simulated results, with greater detail and features present in the calculations utilizing a larger number of voxels.

The two previous figures demonstrate results along the origin of the z-axis, where all values are extracted from x = 0 mm. If values are desired off-axis, for example 20 mm from the coil surface, in the medial coronal plane, variations in the discretization step size means not all models have a value calculated at exactly z = -20 mm. In this case, values from the nearest grid position must be analyzed. The results of this scenario are presented in Figure 4.22. Good corroboration of magnetic field values is seen for models with 2 million or more voxels. Significant differences are observed in the models with fewer voxels.

The electric field calculated 20 mm below the vertex of the head, in the medial coronal plane is shown in Figure 4.23. The results again show that detail is lost in the models with fewer than 2 million voxels. This is highlighted by the peak at approximately x = -0.015 m not being present in the data obtained from those models.

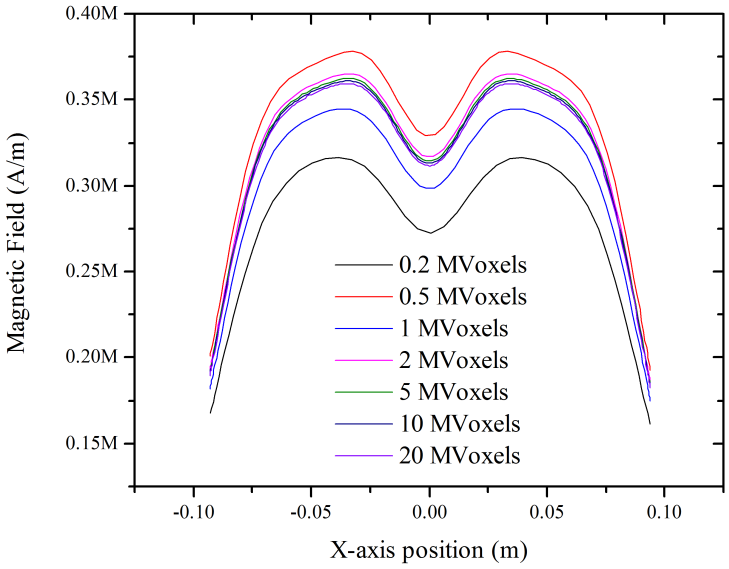

Figure 4.22. Calculated magnetic field along the model x-axis, 20 mm below the coil surface and vertex of the head, in the medial coronal plane.

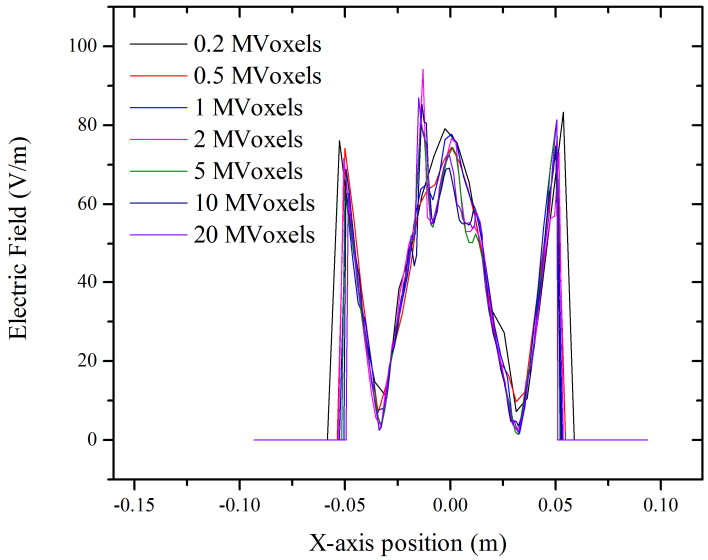

Figure 4.23. Calculated electric field induced in an inhomogeneous head model, along the model x-axis, 20 mm below the coil surface and vertex of the head, in the medial coronal plane.

4.3 Variation of dieletric parameters

Biological material is highly inhomogeneous, consisting of cellular structures containing water, ions, organic molecules and insoluble particles. Unlike electrical conductors such as copper, biological material facilitates charge transportation through ionic conduction. The nature of biological material therefore has an effect on how it interacts with an electric field. If the size of the structural features in the tissue are smaller than the wavelength of the field the bulk response of a tissue can be described by the relative permittivity [5]. For TMS the dielectric properties are around the α-dispersion region, 1-100 kHz. In this range, the relative permittivity of some tissues can be large, with values from approximately 10^3 to 10^7 [6]–[8]. Establishing values of relative permittivity has proven difficult due to disagreement between *in vivo* and *in vitro* measurements and variation in permittivity of exanimated tissue [9]. Measurements of muscle tissue *in vivo* have yielded relative permittivity values up to 10^7 [10], [11]. This can be explained in part by interfacial polarization and counterion diffusion effects [5] but further examination of the properties is still needed. The frequency dependence of relative permittivity and electrical conductivity of grey matter calculated with the IT'IS material parameter database [2] is shown in Figure 4.24.

Through electromagnetic modeling, the extent to which variation in relative permittivity and electrical conductivity affects induced electric fields during TMS can be examined. Using the anatomically realistic head model, the relative permittivity and electrical conductivity of different brain tissues can be varied and the effect on the resulting induced electric field can be studied. Figures 4.25 and 2.26 demonstrate that the

induced electric field during TMS is nearly independent of variation of the relative permittivity. The induced electric field profiles for the two heterogeneous head models did not vary. The variation in the induced electric field was due to the difference in the conductivities of the tissue but not due to the differences in relative permittivity up to the point where displacement currents are in the range of conduction currents.

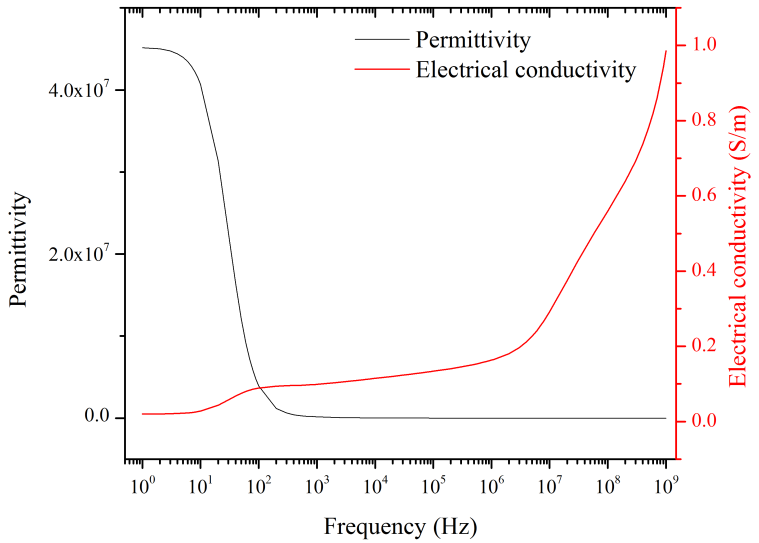

Figure 4.24. Frequency dependence of relative permittivity and electrical conductivity of grey matter calculated with the IT'IS material parameter database.

This result is significant as in the framework of TMS it is understood that spatial variations in induced electric field at axon terminations or bent paths, like the interface between grey and white matter can have significant impact on the site of stimulation [12]. Wagner *et al.* described the effect of different relative permittivities on current density in the brain, showing no significant impact is caused by changing values between 10^2 and 10^4 [13]. However, the model utilized in the present study has higher resolution [2].

The effect on induced electric field can be studied by modeling the electrical conductivity of a single type of tissue with varied values. The electrical conductivity of

principal tissues in the brain have been increased by 50, 100, and 150% without changing the relative permittivity and electrical conductivity values of surrounding tissues. The results are shown in Figure 4.27.

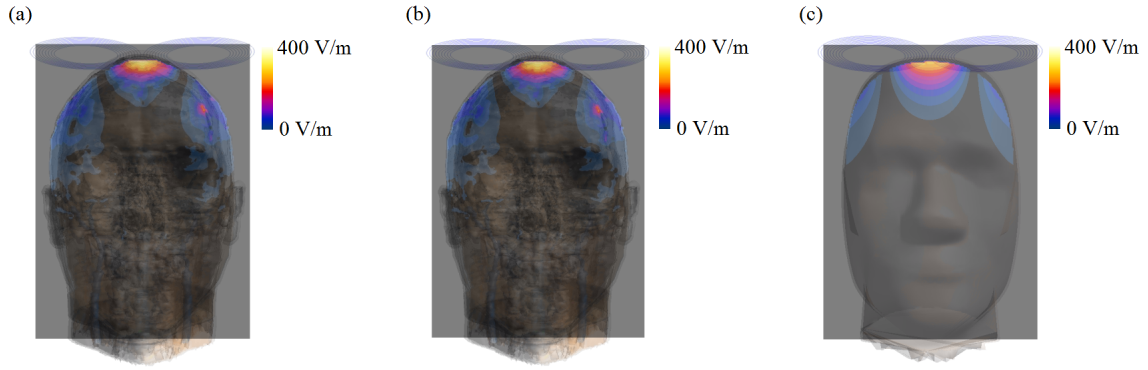

Figure 4.25. Calculated induced electric field in head models with (a) varying electrical conductivity and relative permittivity, (b) varying electrical conductivity and constant relative permittivity, (c) constant electrical conductivity and relative permittivity.

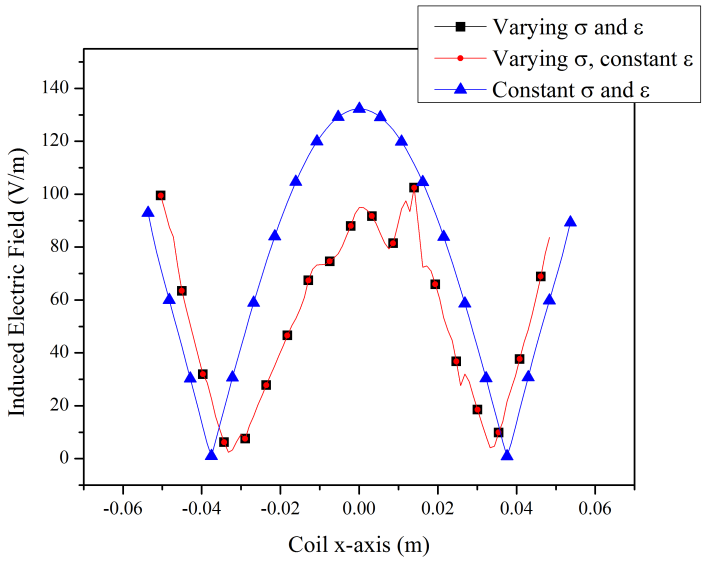

Figure 4.26. Calculated induced electric field 20 mm from coil surface in head models with (a) varying electrical conductivity and relative permittivity, (b) varying electrical conductivity and constant relative permittivity, (c) constant electrical conductivity and relative permittivity.

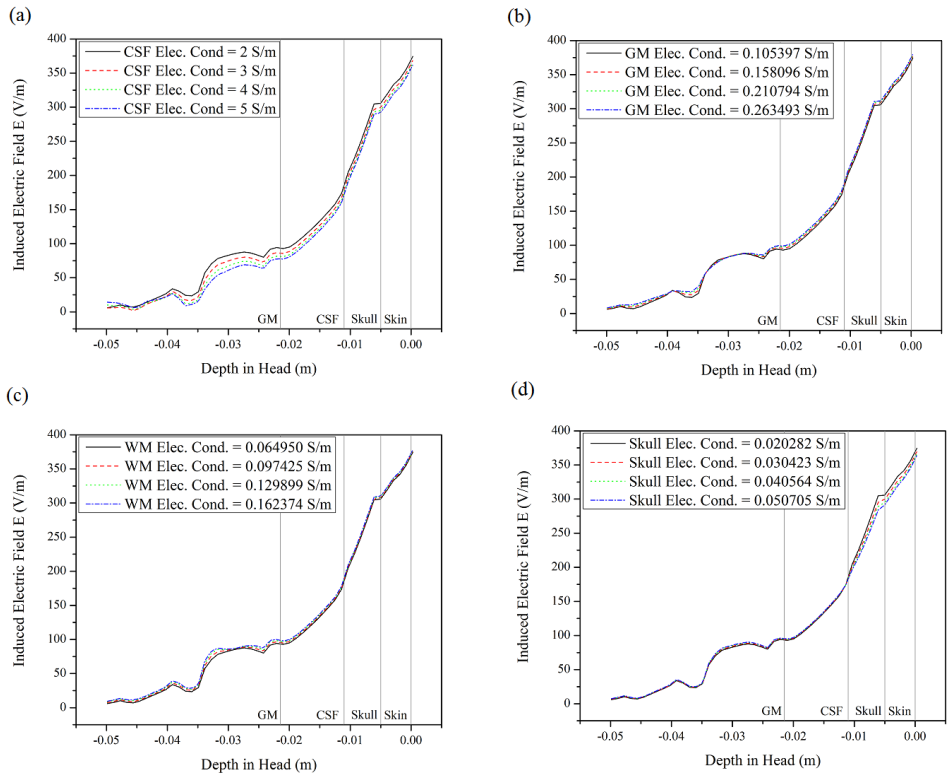

Figure 4.27. Calculated induced electric field decay in anatomically realistic head model utilizing a modeled figure-8 coil positioned at the vertex with electrical conductivity of the (a) cerebrospinal fluid, (b) grey matter, (c) white matter, and (d) skull increased by 50, 100, and 150%.

The results show that the electric field is altered in a number of regions in the head, not just the region where the electrical conductivity value has been modified. Changing the electrical conductivity of CSF has an effect on the induced electric field in the CSF and grey matter region while having a smaller effect on the skin region, and little effect on the induced electric field in the skull. Similarly, changing the electrical conductivity of the grey and white matter also affects the induced electric field in the grey matter. Variation of the electrical conductivity of the CSF caused the largest changes to the overall electric field than the other tissues. This indicates CSF is the most sensitive part of the head that influences the electric field induced in the brain during TMS. It is worth noting that the induced electric field depends on the change of magnetic field with

respect to time and this value changes with distance from the coil. Due to the structure of the head this cannot be avoided. Surprisingly, variation in the conductivities of white matter and grey matter do not influence the change in the electric field as significantly as CSF.

4.4 Effect of brain size and coil orientation on induced electric field

Most studies of TMS consider adult subjects but there is potential for the method to also be a beneficial tool for patients of younger ages. It is well known that the anatomical structure of the brain changes somewhat during childhood and earlier studies using scaled adult head models in the study of RF radiation have been shown to be erroneous. Using a variety of anatomically realistic human head models of varying age, the extent to which induced electric field depends upon the age of the subject can be determined.

During infancy and adolescence complex structural changes occur in the brain. For example, a linear increase of white matter is observed whereas grey matter growth occurs pre-adolescence and decreases post-adolescence [14]. The latency of the ipsilateral silent period has also been seen to decrease from an age of 6 years to early adolescence [15], representative of myelination of the corpus callosum and the development of cortical inhibitory neurons. As shown previously in this chapter, the electric field induced by TMS depends on the dielectric properties of the brain tissue being stimulated. Indications suggest that other age-dependent parameters will also have

an effect on the induced electric field. Therefore, the nature of these changes needs to be studied at different stages of development.

Previous modeling studies of electromagnetic fields in young subjects have utilized scaled adult models. These scaled models introduce anatomical errors due to the non-uniform growth of organs as identified in other studies [16], [17]. Anatomically realistic models of varying ages were obtained from the Virtual Family Project [1], shown in Figure 4.28, which are derived from MRI data of an adult male and female, aged 34 and 26 years, respectively, a female aged 11 years and male aged 6 years. The spatial resolution of the data is 0.9 × 0.9 × 2.0 mm in the trunk and limbs and 0.5 × 0.5 × 1.0 mm in the head. Details of each subject are provided in Table 4.3.

To observe the effect of the inhomogeneous tissue, equivalent homogeneous head models based on the standard anthropomorphic model (SAM) were developed, oriented and scaled to closely match the position and dimensions of the inhomogeneous models. As before, dielectric parameters for the tissues of each model were obtained from the IT'IS tissue database [2]. Each inhomogeneous head model is shown in Figure 4.29 with the modeled figure-8 TMS coil.

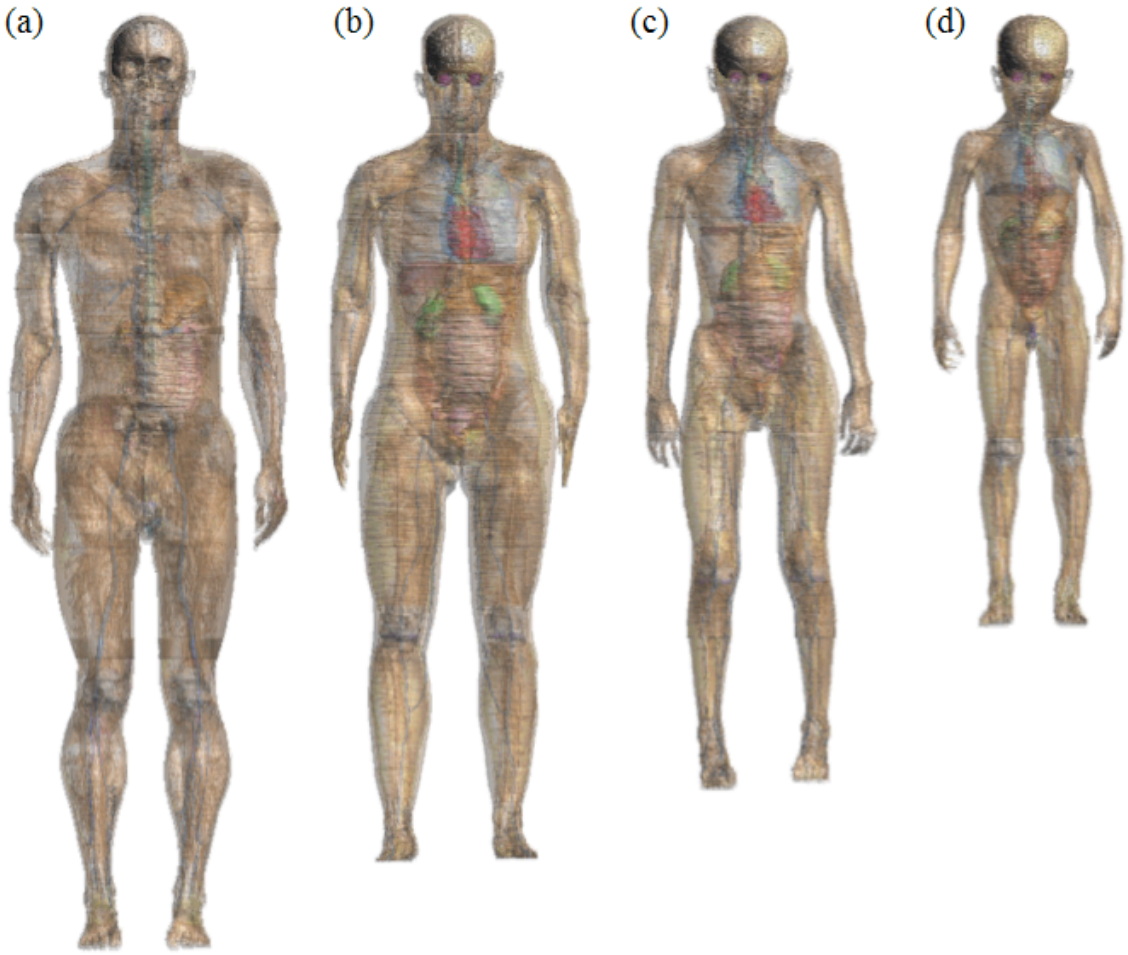

Figure 4.28. Anatomically realistic human body models of (a) 34-year-old male, (b) 26-year-old female, (c) 11-year-old female, and (d) 6-year-old male.

Table 4.3. Anatomically realistic MRI-derived body model specifications.

Sex	Age [years]	Height [m]	Weight [kg]	BMI [kg/m^3]
M	34	1.77	72.4	23.1
F	26	1.63	58.7	22.0
F	11	1.47	35.4	16.5
M	6	1.17	19.3	14.0

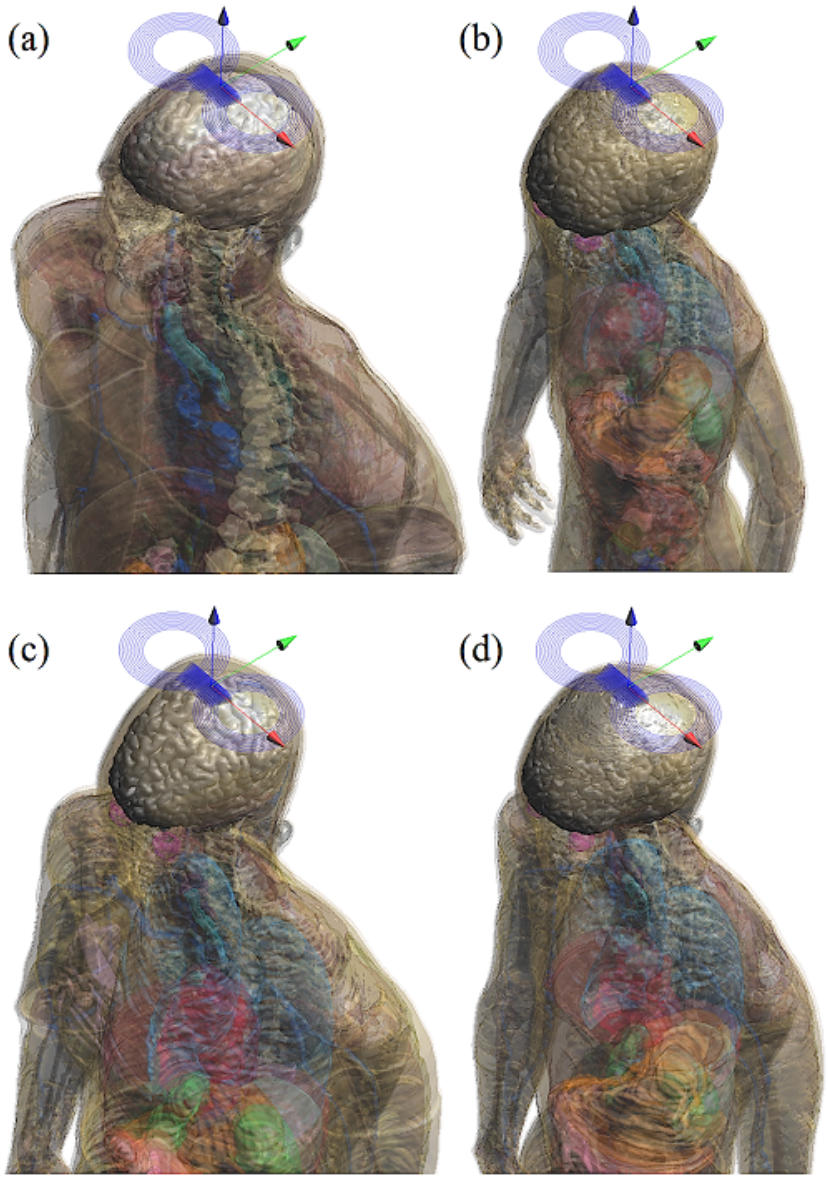

Figure 4.29. Modeled figure-8 coil with anatomically realistic human body models of (a) 34-year-old male, (b) 6-year-old male, (c) 26-year-old female, and (d) 11-year-old female.

The electric field induced in the central coronal plane of each inhomogeneous model and equivalent homogeneous head model are shown in Figure 4.30. The exposure scenario investigated considers the TMS coil targeting the tissue below the vertex of the head.

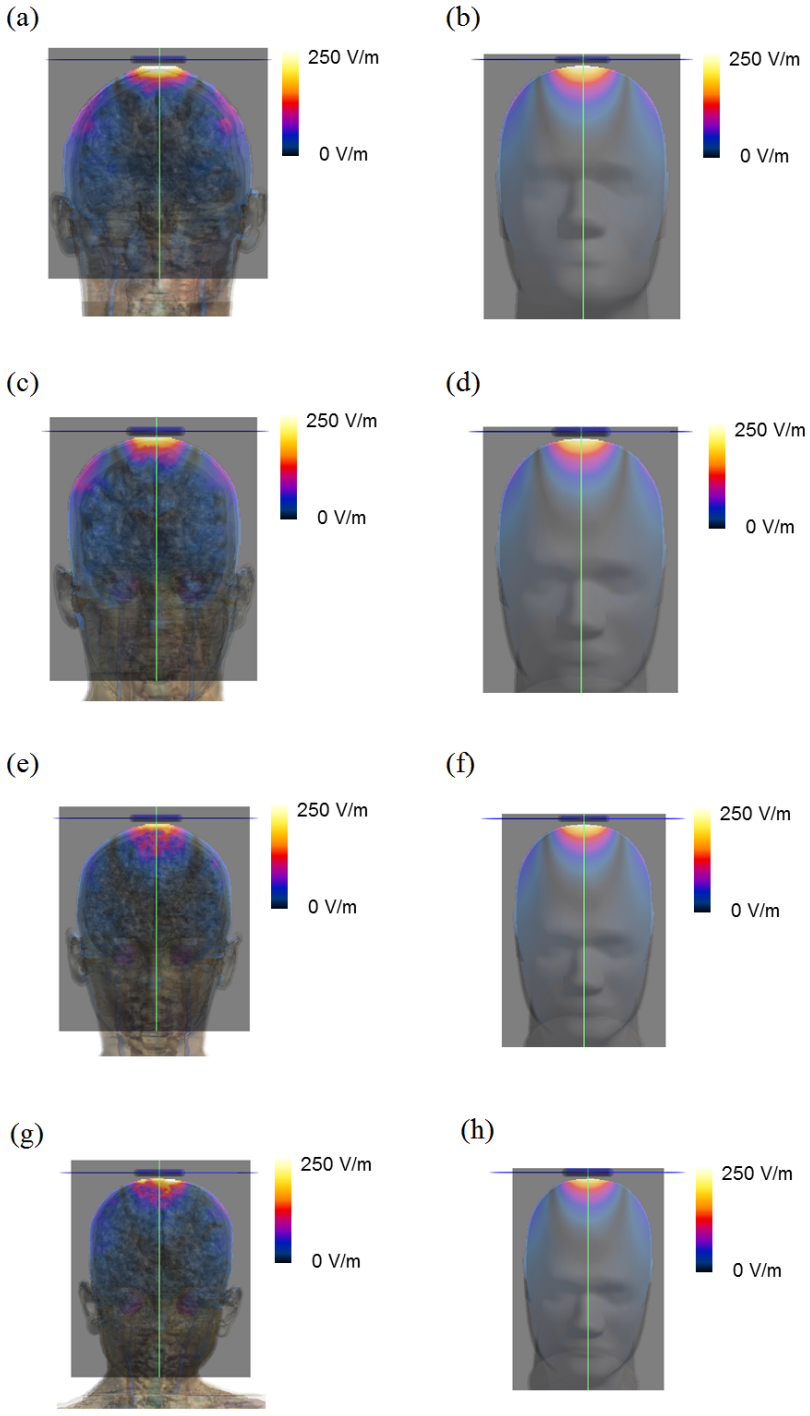

Figure 4.30. Induced electric field calculated in central coronal plane of (a) inhomogeneous 34-year-old male and (b) homogeneous equivalent, (c) inhomogeneous 26-year-old female and (d) homogeneous equivalent, (e) inhomogeneous 11-year old female and (f) homogeneous equivalent, and (g) inhomogeneous 6-year-old male and (h) homogeneous equivalent.

The induced electric field calculated along each inhomogeneous model z-axis, through the vertex of the head is shown in Figure 4.31. For the inhomogeneous models, the values of electric field in the two child models differ from that of adult models significantly in the 20 to 30 mm region, where neural tissue is located. The same result for the homogenous equivalent models are shown in Figure 4.32. In the case of the homogeneous models, marginally lower values of electric field are calculated in the child head models, a result consistent with that of Weissman *et al.* where small animal brains were considered [18].

The shape of the coil will also have an effect on how electric field is distributed in the brain and should be considered when determining safety guidelines for pediatric TMS studies. These studies could be improved by considering the variation in dielectric properties that occur with age. Peyman *et al.* [19] have demonstrated that electrical conductivity of bone marrow reduces significantly with age although only slight changes in SAR are observed in radio frequencies investigations. Overall the results show that different protocols should be considered when conducting TMS experiments with pediatric patients to ensure desired neurological effects are achieved in a safe manner.

The effect of varying the TMS coil position and orientation have also been investigated. Various orientations of the modeled figure-8 coil are shown in Figure 4.33 with the adult male anatomically realistic human head model. In each case the cortical target remains the same but the coil has been rotated by 45-degree increments.

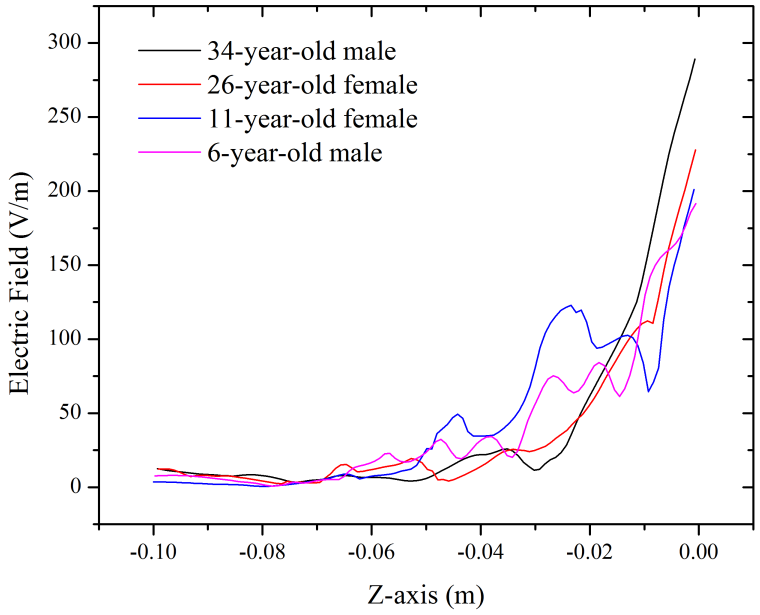

Figure 4.31. Induced electric field calculated along vertical z-axis in inhomogeneous models.

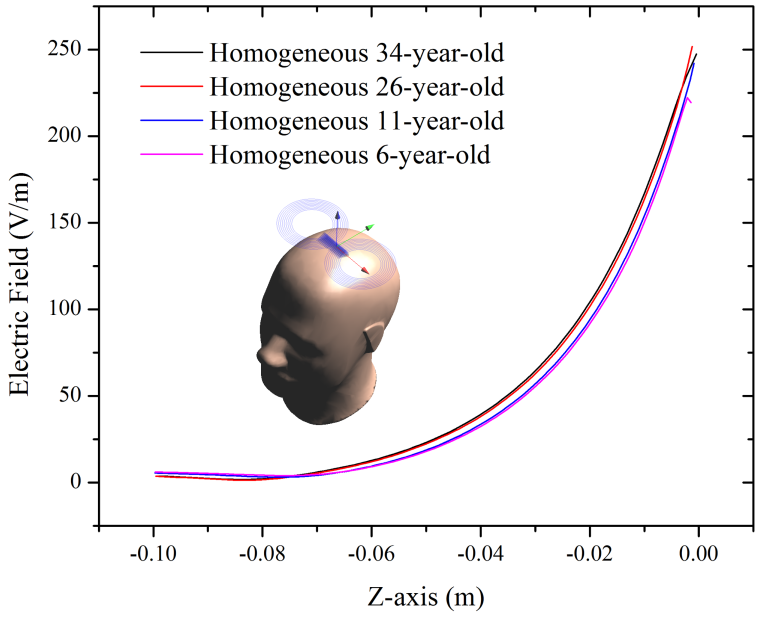

Figure 4.32. Induced electric field calculated along vertical z-axis in homogeneous models.

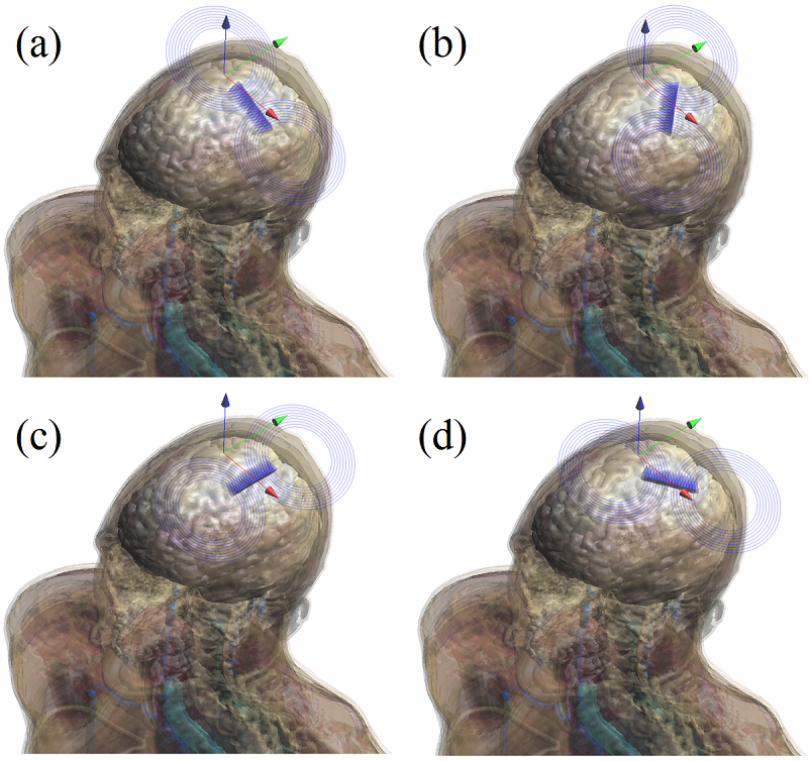

Figure 4.33. Anatomically realistic human head model with four rotations of figure-8 coil.

The resulting magnetic flux density on the surface of the grey matter is shown in Figure 4.34. The effect of coil orientation on the distribution of magnetic flux density is clearly evident. The electric field induced on the surface of the grey matter is shown in Figure 4.35. Distinctly different patterns of induced electric field on the surface of the grey matter are observed, despite the coil being centered above the same region. A significant effect on the localization of electric field on the surface of the head model is also observed, indicating that coil orientation can have a large effect on the volume of neural tissue that may be stimulated.

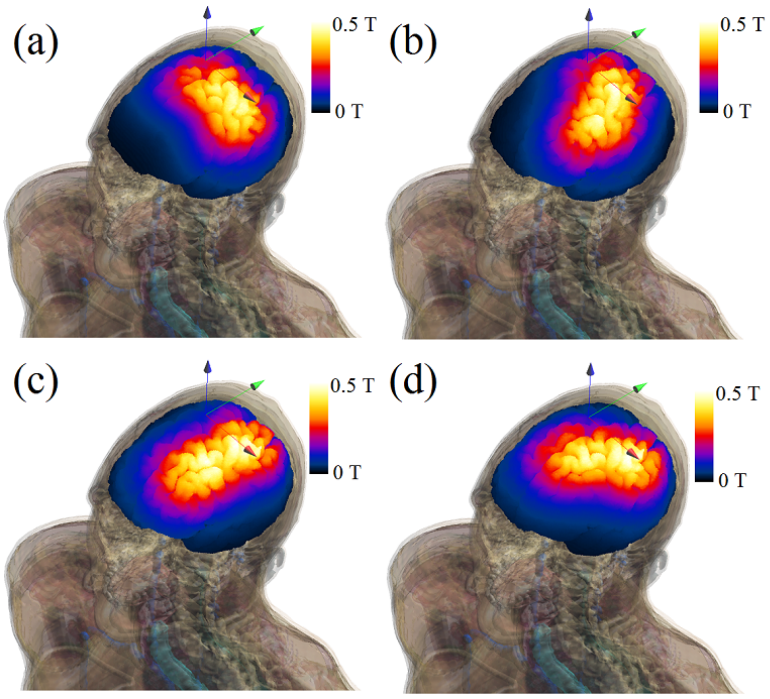

Figure 4.34. Magnetic flux density on surface of grey matter for four rotations of figure-8 coil, (a) 0 degrees, (b) 45 degrees, (c) 90 degrees, and (d) 135 degrees.

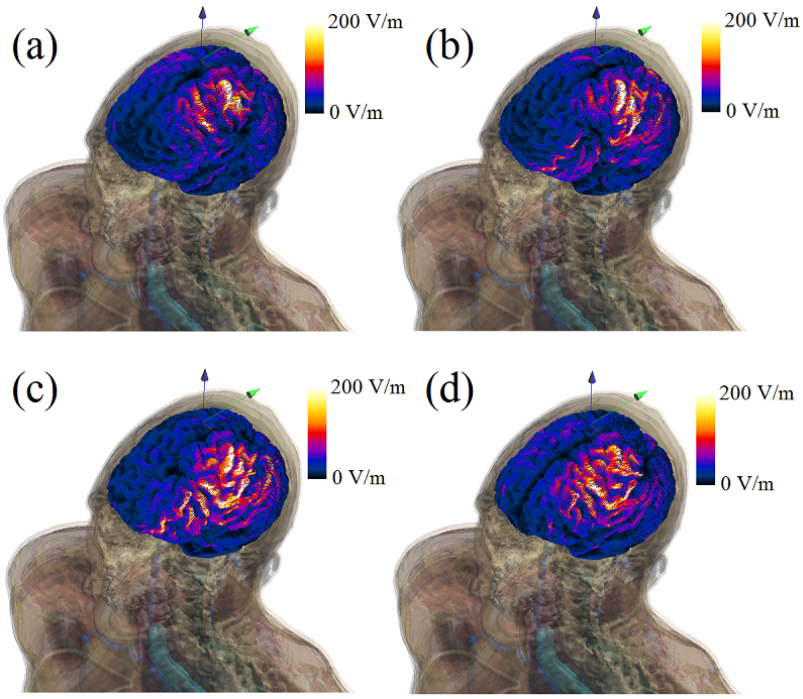

Figure 4.35. Induced electric field on surface of grey matter for four rotations of figure-8 coil, (a) 0 degrees, (b) 45 degrees, (c) 90 degrees, and (d) 135 degrees.

The induced electric field in the medial coronal plane of the anatomically realistic human head models is shown in Figure 4.36. This figure demonstrates the extent to which coil orientation affects the penetration of the induced electric field.

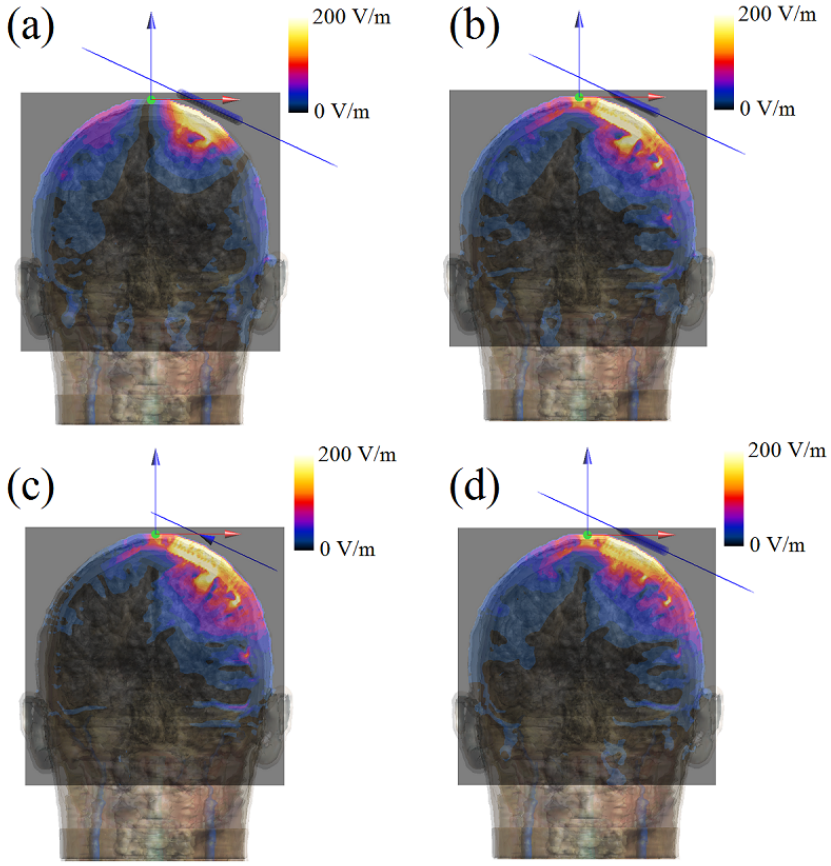

Figure 4.36. Induced electric field profiles in medial coronal plane of anatomically realistic human head model for four rotations of figure-8 coil, (a) 0 degrees, (b) 45 degrees, (c) 90 degrees, and (d) 135 degrees.

The figures demonstrate the differences in magnetic flux density and induced electric field that arise when changing coil orientation, even when centered over the same cortical target. An increased understanding of the resulting changes in induced electric field can be obtained by studying the effect of the gyral folding pattern as demonstrated in Figure 4.37. The figures indicate that gyrus ridges are preferentially stimulated when oriented parallel to the long axis of the figure-8 TMS coil.

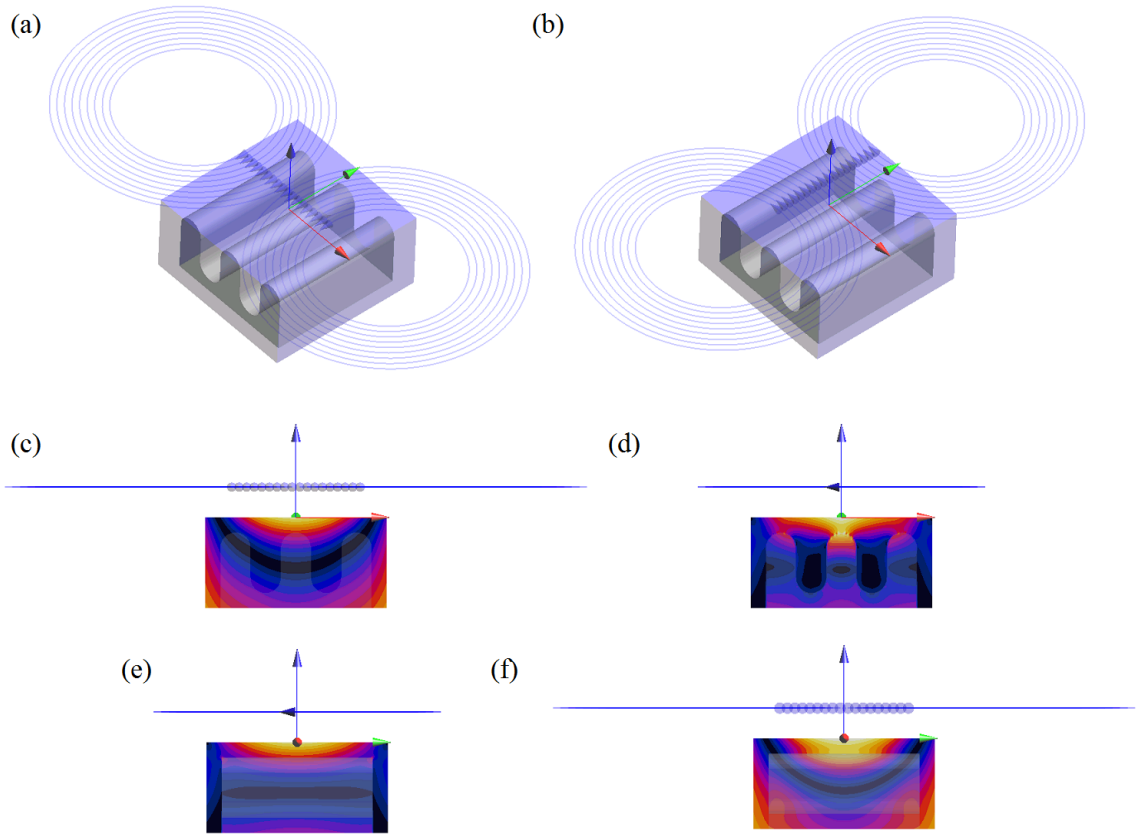

Figure 4.37. Model of gryral folding pattern with (a) first coil orientation, (b) second coil orientation, rotated 90 degrees, (c) induced electric field in front-facing plane for first and (d) second orientation, and (e) side-facing orientation for first and (f) second orientation.

References

[1] A. Christ, W. Kainz, E. G. Hahn, K. Honegger, M. Zefferer, E. Neufeld, W. Rascher, R. Janka, W. Bautz, J. Chen, and others, "The Virtual Family—development of surface-based anatomical models of two adults and two children for dosimetric simulations," *Phys. Med. Biol.*, vol. 55, no. 2, p. N23, 2010.

[2] P. A. Hasgall, E. Neufeld, M. C. Gosselin, A. Klingenböck, and N. Kuster, "IT'IS Database for thermal and electromagnetic parameters of biological tissues," *Sept. 26th*, 2011.

[3] F. A. Kozel, Z. Nahas, M. Molloy, J. P. Lorberbaum, D. Bohning, S. C. Risch, M. S. George, and others, "How coil--cortex distance relates to age, motor threshold,

and antidepressant response to repetitive transcranial magnetic stimulation," *J. Neuropsychiatry Clin. Neurosci.*, vol. 12, no. 3, pp. 376–384, 2000.

[4] T. Kammer, S. Beck, A. Thielscher, U. Laubis-Herrmann, and H. Topka, "Motor thresholds in humans: a transcranial magnetic stimulation study comparing different pulse waveforms, current directions and stimulator types," *Clin. Neurophysiol.*, vol. 112, no. 2, pp. 250–258, 2001.

[5] B. Greenebaum and F. S. Barnes, *Bioengineering and Biophysical Aspects of Electromagnetic Fields*. CRC press, 2006.

[6] C. Gabriel, S. Gabriel, and E. Corthout, "The dielectric properties of biological tissues: I. Literature survey," *Phys. Med. Biol.*, vol. 41, no. 11, p. 2231, 1996.

[7] S. Gabriel, R. W. Lau, and C. Gabriel, "The dielectric properties of biological tissues: II. Measurements in the frequency range 10 Hz to 20 GHz," *Phys. Med. Biol.*, vol. 41, no. 11, p. 2251, 1996.

[8] S. Gabriel, R. W. Lau, and C. Gabriel, "The dielectric properties of biological tissues: III. Parametric models for the dielectric spectrum of tissues," *Phys. Med. Biol.*, vol. 41, no. 11, p. 2271, 1996.

[9] H. Schwan, "Die elektrischen eigenschaften von muskelgewebe bei niederfrequenz," *ZEITSCHRIFT FUR Naturforsch. Sect. BA J. Chem. Sci.*, vol. 9, no. 4, pp. 245–251, 1954.

[10] F. X. Hart and W. R. Dunfee, "In vivo measurement of the low-frequency dielectric spectra of frog skeletal muscle," *Phys. Med. Biol.*, vol. 38, no. 8, p. 1099, 1993.

[11] F. X. Hart, R. B. Toll, N. J. Berner, and N. H. Bennett, "The low-frequency dielectric properties of octopus arm muscle measured in vivo," *Phys. Med. Biol.*, vol. 41, no. 10, p. 2043, 1996.

[12] P. C. Miranda, L. Correia, R. Salvador, and P. J. Basser, "The role of tissue heterogeneity in neural stimulation by applied electric fields," in *Engineering in Medicine and Biology Society, 2007. EMBS 2007. 29th Annual International Conference of the IEEE*, 2007, pp. 1715–1718.

[13] T. A. Wagner, M. Zahn, A. J. Grodzinsky, and A. Pascual-Leone, "Three-dimensional head model simulation of transcranial magnetic stimulation," *Biomed. Eng. IEEE Trans.*, vol. 51, no. 9, pp. 1586–1598, 2004.

[14] J. N. Giedd, J. Blumenthal, N. O. Jeffries, F. X. Castellanos, H. Liu, A. Zijdenbos, T. Paus, A. C. Evans, and J. L. Rapoport, "Brain development during childhood

and adolescence: a longitudinal MRI study," *Nat. Neurosci.*, vol. 2, no. 10, pp. 861–863, 1999.

[15] M. A. Garvey, U. Ziemann, J. J. Bartko, M. B. Denckla, C. A. Barker, and E. M. Wassermann, "Cortical correlates of neuromotor development in healthy children," *Clin. Neurophysiol.*, vol. 114, no. 9, pp. 1662–1670, 2003.

[16] J. Wiart, A. Hadjem, N. Gadi, I. Bloch, M. F. Wong, A. Pradier, D. Lautru, V. F. Hanna, and C. Dale, "Modeling of RF head exposure in children," *Bioelectromagnetics*, vol. 26, no. S7, pp. S19–S30, 2005.

[17] A. Hadjem, D. Lautru, C. Dale, M. F. Wong, V. F. Hanna, and J. Wiart, "Study of specific absorption rate (SAR) induced in two child head models and in adult heads using mobile phones," *Microw. Theory Tech. IEEE Trans.*, vol. 53, no. 1, pp. 4–11, 2005.

[18] J. D. Weissman, C. M. Epstein, and K. R. Davey, "Magnetic brain stimulation and brain size: relevance to animal studies," *Electroencephalogr. Clin. Neurophysiol. Potentials Sect.*, vol. 85, no. 3, pp. 215–219, 1992.

[19] A. Peyman, C. Gabriel, E. H. Grant, G. Vermeeren, and L. Martens, "Variation of the dielectric properties of tissues with age: the effect on the values of SAR in children when exposed to walkie--talkie devices," *Phys. Med. Biol.*, vol. 54, no. 2, p. 227, 2009.

CHAPTER V

RESULTS II: COIL DESIGN FOR TRANSCRANIAL MAGNETIC STIMULATION

5.1 Analysis of existing coil designs

To improve the performance of TMS coils the characteristics of the existing devices must be fully understood. Magnetic field measurements have been performed to identify the differences between commercially available coil designs and determine their relative advantages and limitations. Axial magnetic field measured on the surface of four commercial TMS coils at 100% stimulator output is shown in Figure 5.1. The characterized coils are the circular Magstim HP90 (R) coil and figure-8 D70 (R), D70 (AFC), and D70-2 coils.

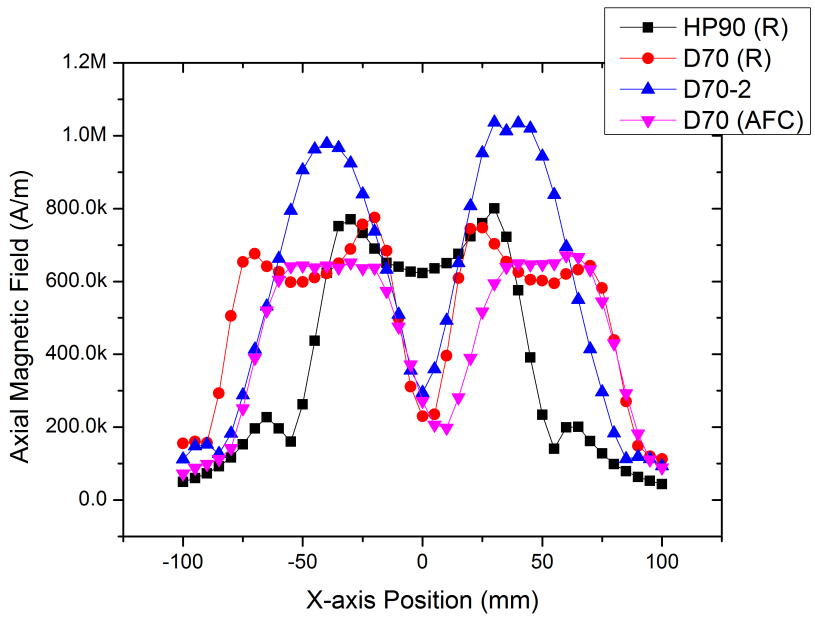

Figure 5.1. Measured axial magnetic field on surface of Magstim HP 90 (R), D70 (R), D70-2, and D70 (AFC) TMS coils at 100% stimulator output.

As expected, the circular and figure-8 coil designs have distinctly different field profiles. However, the D70-2 coil exhibits a significantly different distribution and higher peak magnitude of magnetic field than the other figure-8 coils, despite having a similar design. The three figure-8 coils compared are depicted in Figure 5.2. The Magstim D70 (R) coil has a long-established design and is widely used in research. This particular coil possesses a control on the handle of the coil to initiate stimulation pulses and adjust the stimulator output level. The Magstim D70 (AFC) Air Film Coil differs from the other coils in that it features an integrated cooling fan, to mitigate coil heating during operation. The active cooling allows the coil to be operated for much longer periods of time than the standard D70 (R) coil.

The axial magnetic field measured 20 mm from the coil surfaces at 50% stimulator output is shown in Figure 5.3, together with calculated values from a modeled figure-8 coil. The measurements at this distance indicate that the D70 (AFC) coil produces lower intensity of magnetic field than the D70 (R), while the D70-2 coil produces a higher intensity. To determine the cause in variations of the magnetic field distribution and intensity produced by the three figure-8 coils, x-ray images were generated to reveal the dimensions of the current carrying conductor in each case and overall coil construction. The x-ray images are shown in Figure 5.4, revealing the construction of the D70-2 coil to be significantly different to the other two figure-8 coils. It is apparent the D70-2 coil utilizes Litz wire, which reduces skin and proximity effects. The inner and outer radii of the coil windings are also significantly different to that present in the D70 (R) and D70 (AFC) coils.

\

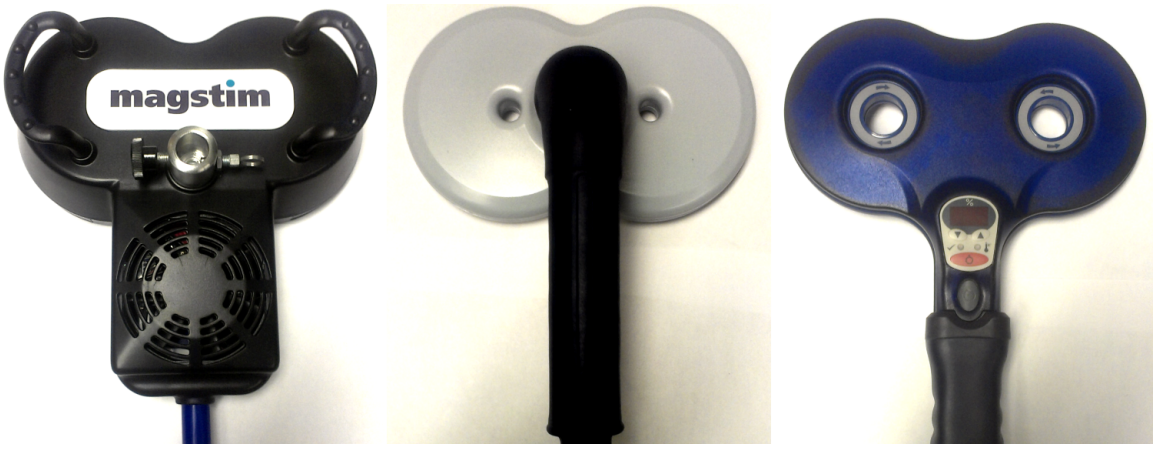

Figure 5.2. Magstim D70 (AFC), D70-2, and D70 (R) figure-8 TMS coils.

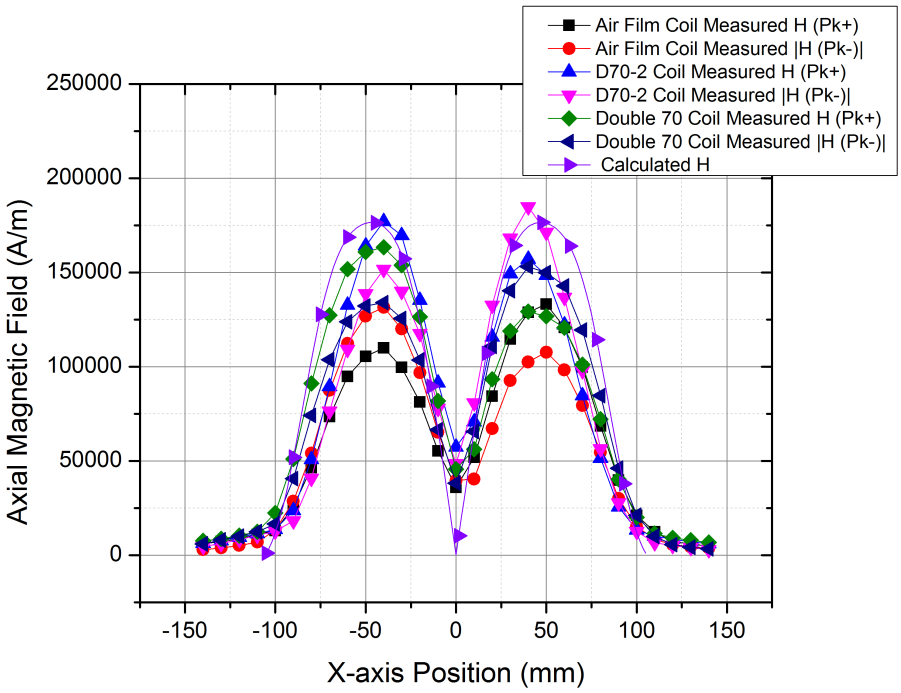

Figure 5.3. Axial magnetic field measured 20 mm from coil surface for Magstim D70 (R), D70-2 and D70 (AFC) figure-8 TMS coils, with calculated values produced by a modeled coil.

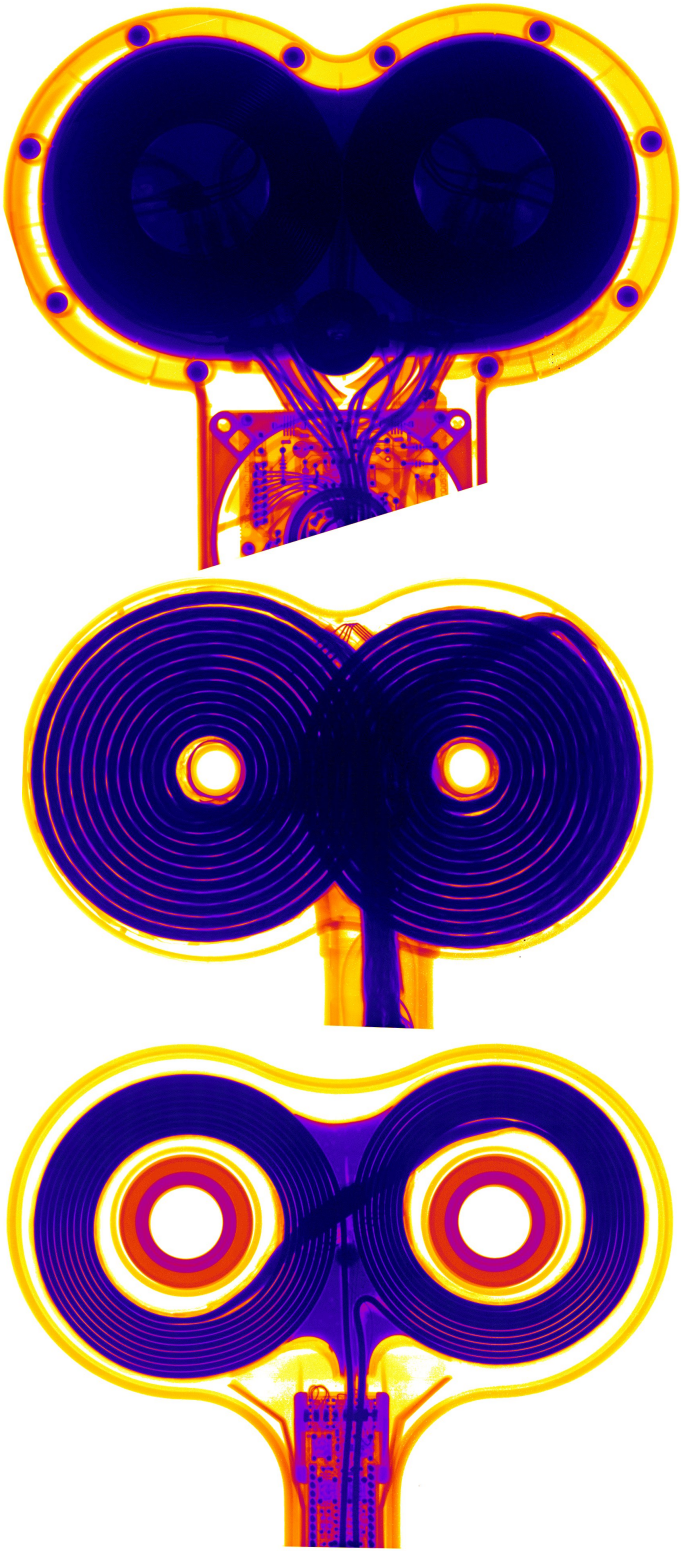

Figure 5.4. X-ray images of Magstim (a) D70 (AFC), (b) D70-2 containing Litz wire, and (c) D70 (R) figure-8 TMS coils.

Measuring the magnetic field generated in an entire plane gives greater insight into the overall field distribution provided by the commercial coils. The axial magnetic field produced by the HP90 (R) circular coil in planes 20 and 40 mm from the coil surface with 50% stimulator output are shown in Figure 5.5. The highest measured value of axial magnetic field 20 mm from the coil surface is approximately 2×10^5 A/m, while at 40 mm the maximum field is approximately 1×10^5 A/m.

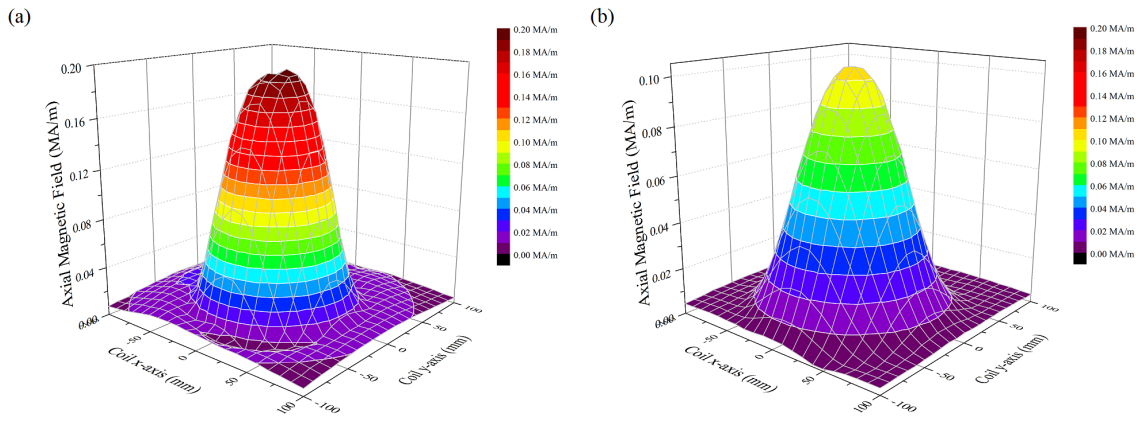

Figure 5.5. (a) Measured axial magnetic field profile of Magstim HP90 (R) circular TMS coil at 50% stimulator output in planes 20 mm and (b) 40 mm from the coil surface.

The axial magnetic field produced by the D70 (R) figure-8 coil in planes 20 and 40 mm from the surface of the coil at 50% stimulator output are shown in Figure 5.6. The maximum field intensity measured at 20 mm is approximately 1.5×10^5 A/m while at 40 mm it is approximately 7×10^4 A/m, both significantly lower than the maximum field produced in these planes by the circular HP90 (R) coil. This is likely due to the HP90 (R) circular coil having 14 turns whereas the D70 (R) figure-8 coil has only 9 turns in each winding.

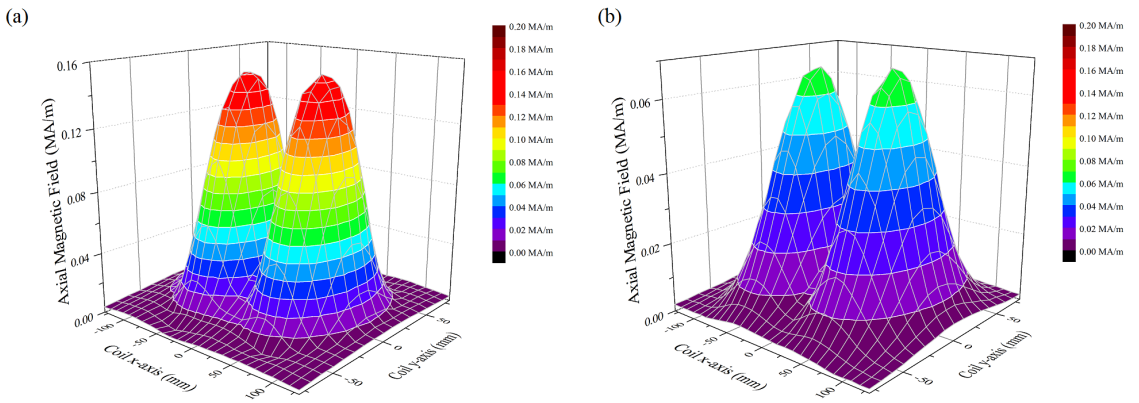

Figure 5.6. Measured axial magnetic field profile of Magstim D70 (R) figure-8 TMS coil at 50% stimulator output in plane 20 mm and (b) 40 mm from the coil surface.

The axial magnetic field produced by the D70-2 and D70 (AFC) figure-8 coils in a plane 20 mm from the surface of the coils are shown in Figure 5.7. Whereas the standard D70 (R) coil produced a maximum field of approximately 1.5×10^5 A/m at this distance, the D70-2 coil produces a maximum of approximately 1.8×10^5 while the cooled D70 (AFC) coil produces approximately 1.35×10^5 A/m.

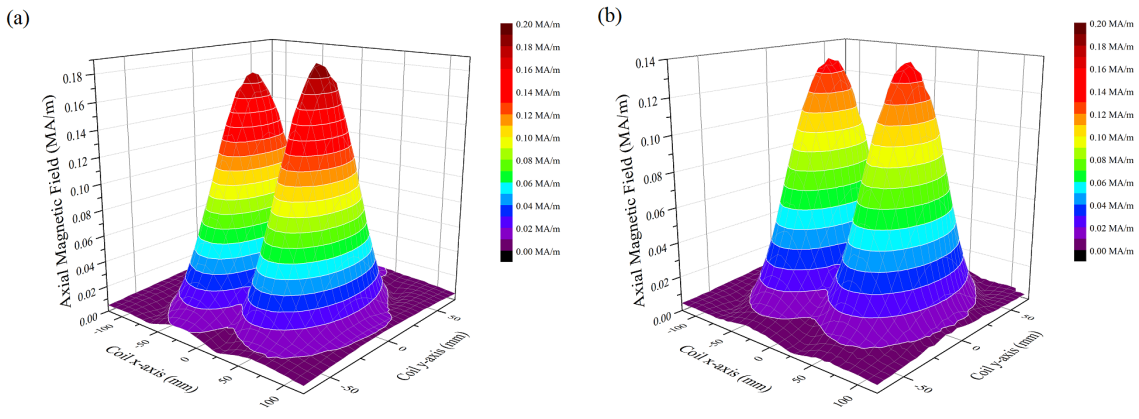

Figure 5.7. (a) Measured axial magnetic field profile at 50% stimulator output in a plane 20 mm from the coil surface of Magstim D70-2 and (b) Magstim D70 (AFC) figure-8 TMS coils.

5.2 Halo coil design

A novel coil design, the 'Halo' coil, a large circular coil capable of being placed around the head has been developed to increase the magnetic field at depth in the brain if used together with existing circular and figure-8 coils commonly used for TMS. The design has been optimized using finite element analysis software incorporating anatomically realistic human head models as described in Chapter 4. The Halo coil increases the depth to which the stimulating field penetrates, allowing more energy to be deposited into deeper regions of the brain. This enables the stimulation of subcortical regions that have previously not been reachable with commercial coils without encountering adverse physiological effects.

Figure 5.8 (a) gives an overview of the Halo coil design, with the anatomically realistic head model of an adult male. The Halo coil has inner and outer radii of 138 and 150 mm, respectively, and has five turns. In this study the Halo coil is operated simultaneously with a typical circular coil of mean diameter 90 mm, with 14 turns. The smaller circular coil is positioned 100 mm above the Halo coil. The optimized Halo coil was constructed, as depicted in Figure 5.8 (b) with a Magstim HP90 (R) coil, and was found to have a resistance of 0.048 Ω and an inductance of 17.966 μH at a frequency of 10 kHz.

In this study, the Halo coil was used together with a circular coil, as it provides less decay of field as a function of distance than a conventional figure-8 coil [1]. A figure-8 coil can alternatively be used together with the Halo coil to increase localization of stimulation at the expense of penetration depth.

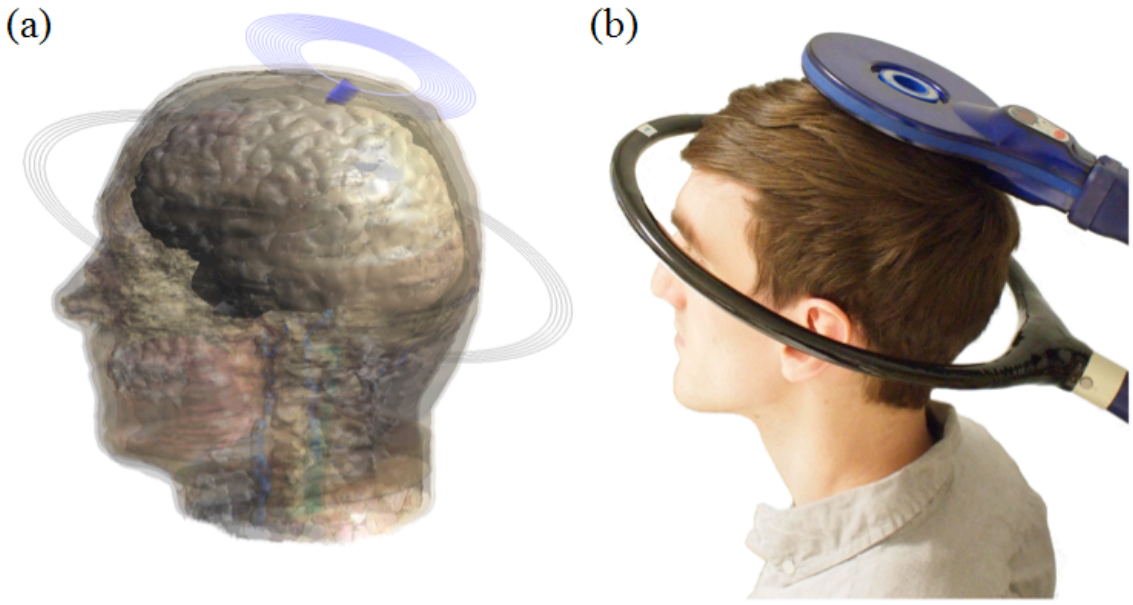

Figure 5.8. (a) Modeled and (b) constructed Halo coil with 90 mm circular coil in typical configuration, separated by 100 mm.

As previously described, earlier studies of TMS coil design have relied on homogeneous spherical volume conductors as head models despite evidence that tissue heterogeneity and anisotropy have a significant effect on the distribution of electric field induced in the brain [2]. The anatomically realistic modeling technique described in Chapter 4 has been employed to accurately predict the site of neural stimulation during TMS to account for the variation in conductivities of the different brain tissues [3].

The model implements a sinusoidal magnetic flux density with a frequency equal to 2.5 kHz and a peak current of 5 kA if 100% stimulator output is assumed. The SAM head model was also utilized, with conductivity, relative permittivity and relative permeability values of 0.33 S/m, 11000 and 1.0, respectively. Magnetic field measurements were performed on the constructed Halo coil with a Gaussmeter and axial

Hall probe, supported by a multi-axis positioning system. The coils were energized with a Magstim Rapid^2 stimulator with either 50 or 100% output.

The magnetic field generated by the circular HP90 (R) coil operated alone and then simultaneously with the Halo was studied for comparison. The Halo coil was positioned 100 mm below the HP90 (R) circular coil, consistent with the configuration shown in Figure 5.8. The magnetic field strength of the Halo coil at 20 and 40 mm below the vertex of the head is shown in Figure 5.9. In both instances the magnetic field is increased compared to the magnetic field produced by the circular coil when used independently.

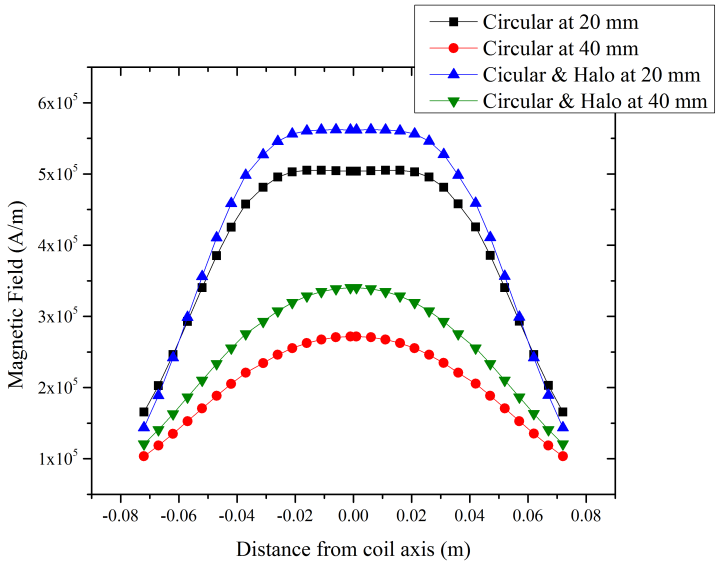

Figure 5.9. Calculated magnetic field 20 and 40 mm below the vertex of the head and circular coil surface.

The electric field strength of both coils in a homogeneous medium is shown in Figure 5.10, at 20 and 40 mm from the surface of the circular coil and the vertex of the head. At both distances the electric field is increased throughout the head. This demonstrates the ability of the Halo coil to induce an electric field of higher magnitude and the capacity to initiate an action potential in neural tissue in deeper regions of the

brain than the circular coil operated alone. Figure 5.11 compares the measured and calculated magnetic field along the common coil axis for the described configuration. The results show very good agreement in both amplitude and rate of decay.

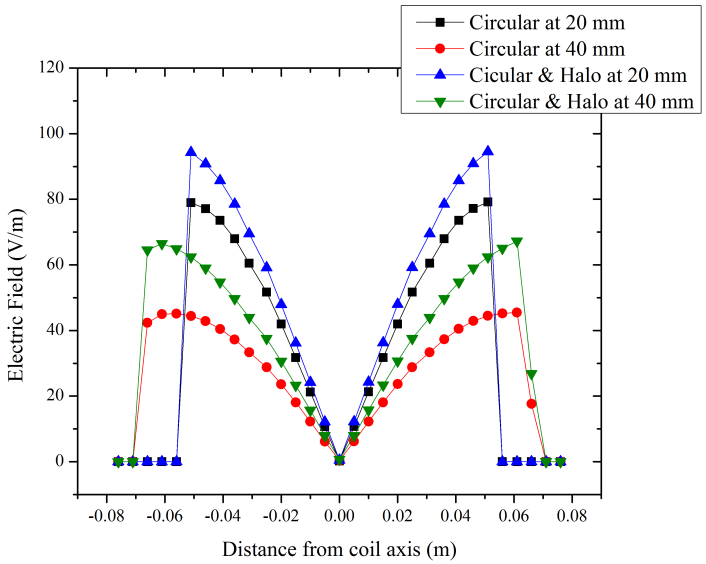

Figure 5.10. Calculated electric field 20 and 40 mm below the vertex of the head and circular coil surface.

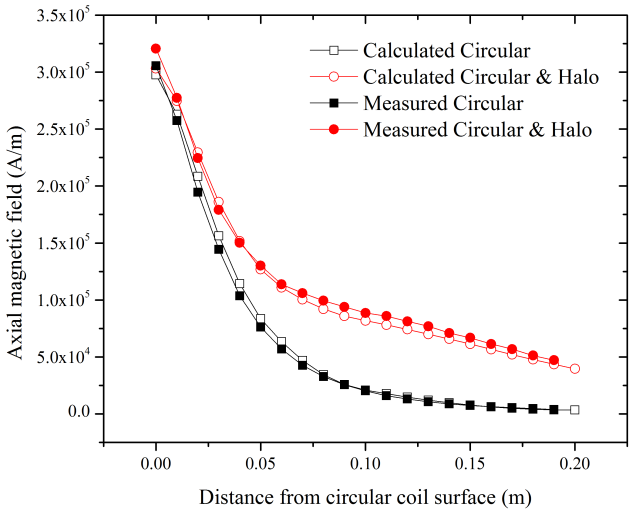

Figure 5.11. Attenuation of magnetic field strength along common coil axis from surface of circular coil with and without Halo coil.

Along the common coil axis the Halo coil can increase the magnetic field strength by approximately 10% at a distance of 20 mm, and by approximately 50% at a distance of 50 mm from the circular coil, compared to the circular coil used independently. The magnetic field in the medial coronal and sagittal planes of the inhomogenous head model is shown in Figure 5.12. The electric field induced in the medial coronal and sagittal planes of the inhomogeneous head model are shown in Figure 5.13.

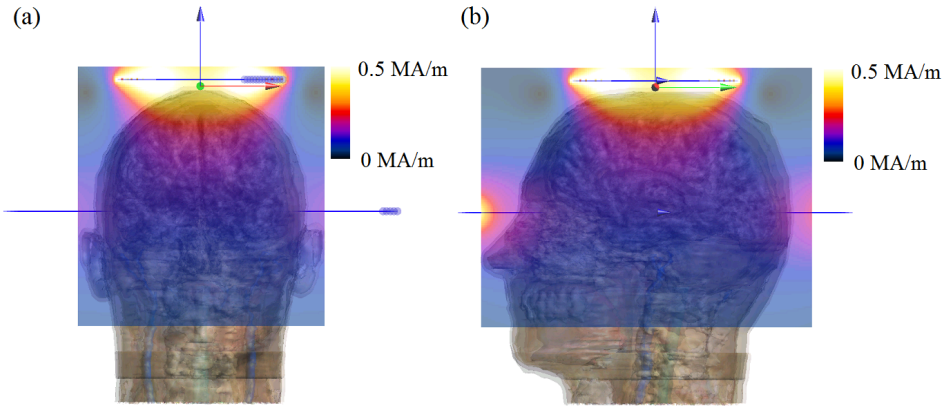

Figure 5.12. Calculated magnetic field in (a) medial coronal and (b) sagittal planes for the inhomogeneous head model with Halo coil and 90 mm circular coil.

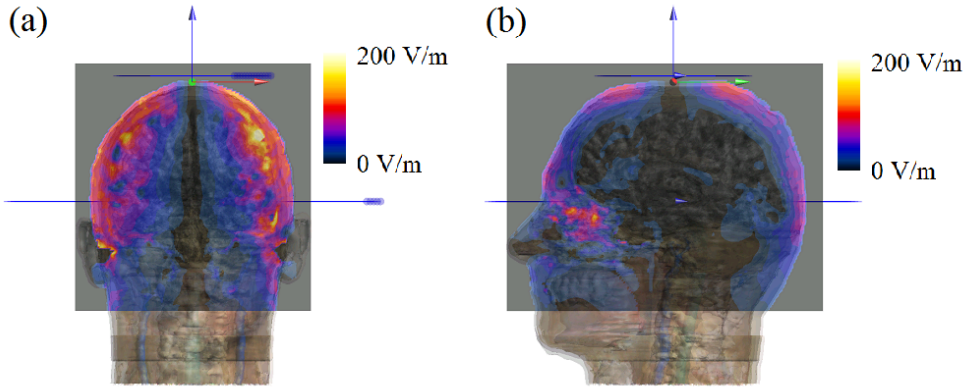

Figure 5.13. Calculated electric field in (a) medial coronal and (b) sagittal planes of the inhomogeneous head model with Halo coil and 90 mm circular coil.

A benefit of the size of the Halo coil is the ability to reposition the coil to change the overall distribution of the magnetic and induced electric field. Figure 5.14 demonstrates the change in the magnetic and electric field distribution by moving the coil 50 mm closer to and away from the 90 mm circular coil. The coil can also be rotated as demonstrated in Figure 5.15.

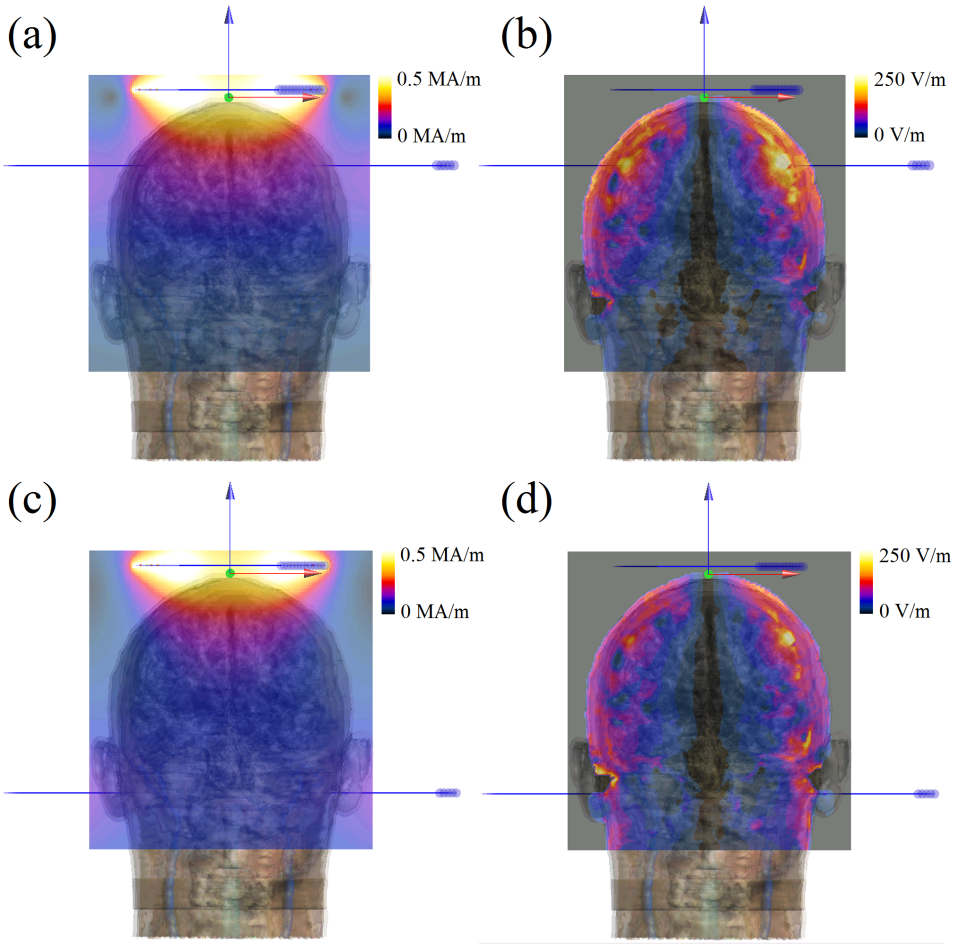

Figure 5.14. Calculated (a) magnetic and (b) electric field with Halo coil positioned 50 mm from 90 mm circular coil, and (c) magnetic and (d) electric field with Halo coil positioned 150 mm from 90 mm circular coil.

In addition to penetration depth, localization of stimulation is an important criterion in the design of TMS coils. The Halo coil does not increase the localization of

electric field but existing methods to suppress the surface field could be employed together with the Halo coil in order to improve localization of the field.

The calculations and experimental measurements demonstrate the performance gains of the Halo coil. Both methods of analysis have shown that the Halo coil is able to improve the penetration depth compared to a standard circular coil used independently. This enables the stimulation of neural tissue at a greater depth than is presently achievable with existing coil designs. These results show promise for developing TMS for additional research and therapeutic applications.

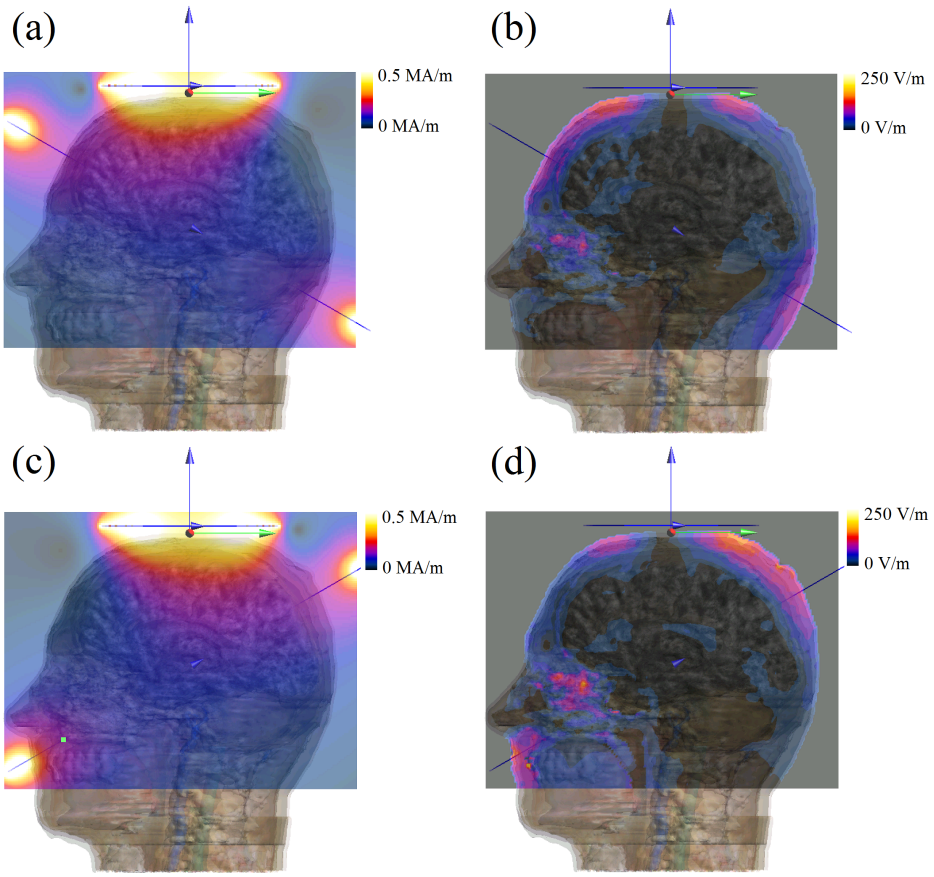

Figure 5.15. Calculated (a) magnetic and (b) electric field with Halo coil rotated +30 degrees, and (c) magnetic and (d) electric field with Halo coil rotated -30 degrees.

5.3 Stimulation depth and localization trade-off

To stimulate neural tissue at depth a variety of coil designs have been studied and developed. Some coil designs that have been investigated are shown in Figure 5.16, with calculated induced electric field distributions.

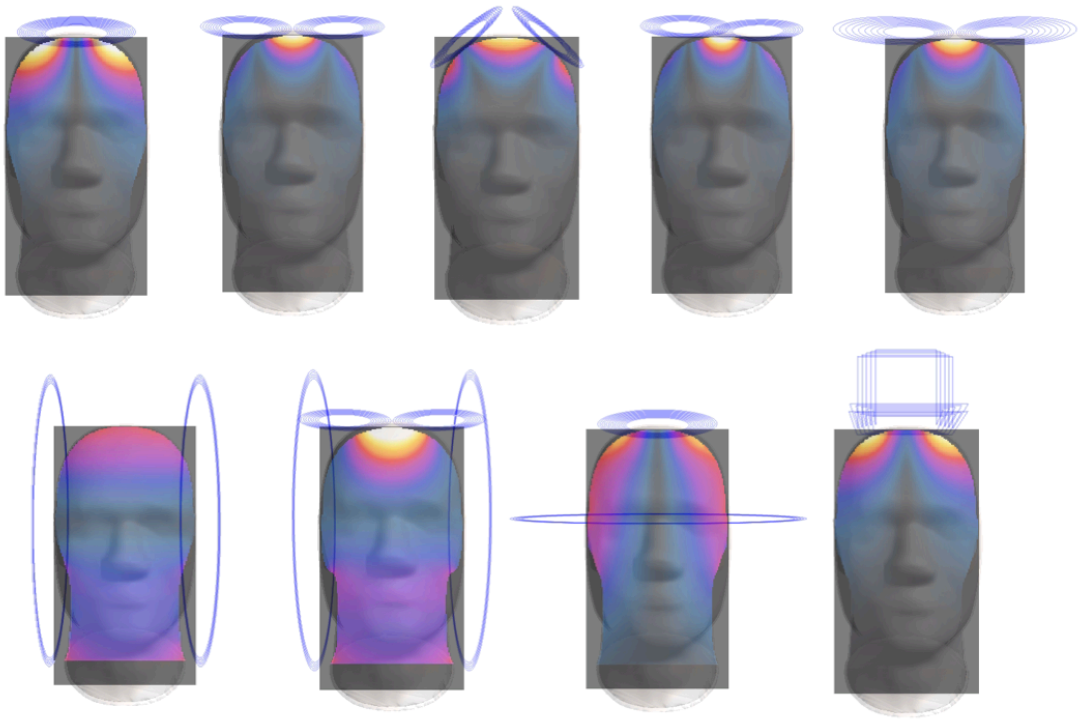

Figure 5.16. Calculated induced electric field in medial coronal plane of homogeneous SAM model for various coil designs.

Localization of stimulation can be quantified as in (5.1), where s_{half} is the localization and tangential field spread, v_{half} is the volume of neural tissue experiencing more than or equal to half the maximum electric field intensity, and d_{half} is the depth to which at least half of the maximum electric field intensity reaches.

$$s_{half} = \frac{v_{half}}{d_{half}} \tag{5.1}$$

Plotting the d_{half} and v_{half} values of each coil reveals a stimulation depth and localization trade-off, as evident in Figure 5.17. Generally it can be stated that the greater the depth of stimulation possible, a larger volume of neural tissue will be stimulated.

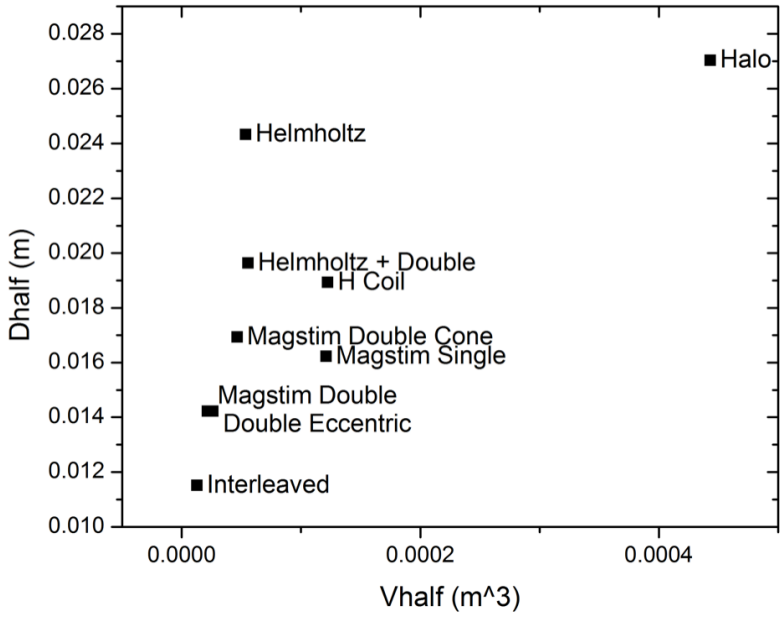

Figure 5.17. Electric field d_{half} and v_{half} values for a variety of proposed TMS coil designs, indicating electric field depth and localization trade-off.

The figure demonstrates that these metrics reveal the novel Halo coil is capable of stimulating to a greater depth than the other coil designs but also stimulates a larger volume of tissue. Ideally, a new coil design would exhibit increased depth of stimulation with reduced volume of high field.

5.4 Coil design for animal subjects

Coils typically used for stimulation of the human brain are very large compared to the dimensions of animals such as mice. The small volume of neural tissue in these animals has been shown to reduce the intensity of induced electric field obtainable with standard TMS equipment [4]. As a result, smaller TMS coils are usually employed for animal studies but there are limits to how small the coils can be made. The present study investigates the suitability of such a TMS coil for this purpose and determines if new animal-specific devices are needed. Results of this study are essential for designing experimental protocols for TMS studies utilizing animal subjects.

It has been demonstrated that tissue heterogeneity and anisotropy of electrical conductivity have a profound effect upon the induced electric field in the brain during TMS [2], [5]. For modeling purposes, a high-resolution anatomically realistic adult mouse model has been obtained for this study. The mouse model is derived from structural MRI data of a male OF1 type mouse, of length 95 mm (excluding tail), weighing 35.5 g. The mouse model has been segmented into 50 distinct tissues for which electrical properties can be independently incorporated in similar fashion to the human anatomical models. Dielectric tissue parameters were obtained from the IT'IS database [6] which utilizes the work of Gabriel *et al.* [7]–[9]. This method can yield unusually high permittivity values at TMS frequencies but these have been shown to be an insignificant factor in the calculation of induced electric field for TMS [10].

The electromagnetic simulation incorporated a sinusoidal magnetic flux density of 2.5 kHz and 100% power was assumed to correspond to a current of 7 kA passing

through the coil. A commercially available coil identified as being adequate for the stimulation of mice was obtained. The coil, a Magstim 25 mm figure-8 coil, is shown in Figure 5.18. The coil has an internal and external diameter of each winding of 12 and 43 mm, respectively. The overall size of this coil is smaller than the TMS coils commonly used for stimulation of the human brain but still large compared to the animal subject size. Each winding of the coil contains 15 turns of copper wire with cross sectional area 5 × 0.8 mm.

Figure 5.18. Magstim 25 mm figure-8 coil, identified as suitable for small-animal studies.

The calculations assume the coil is placed on the surface of the mouse head, centered above the brain. The peak field intensity calculated for the modeled coil, in a plane 10 mm from the coil surface, at 50% stimulator output was 5.36×10^5 A/m. This is higher than the calculated peak magnetic field generated by the TMS coils normally used for stimulation of the human brain [5].

Measurements of axial magnetic field were performed along the x-axis of the coil, at distances of 10 and 20 mm from the coil surface with a Gaussmeter and axial Hall probe. The measurements are shown together with calculations of the axial magnetic field in Figure 5.19.

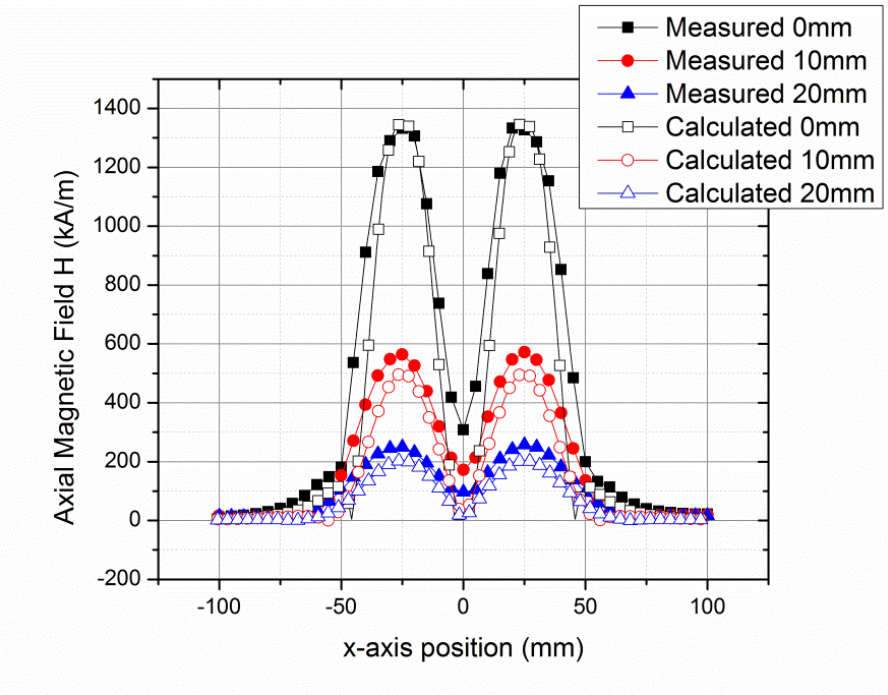

Figure 5.19. Measurements and calculations of axial magnetic field of a Magstim 25 mm figure-8 coil, along coil surface (x-axis) and at distances of 10 and 20 mm.

The maximum field intensity was found to be at the center of the windings, reaching approximately 1.35×10^6 A/m at the coil surface, reducing to approximately 0.5×10^6 A/m at 10 mm, and to 0.2×10^6 A/m at 20 mm. The measured and calculated values show good agreement, particularly at the coil surface, in proximity to the mouse brain. Measurements of the axial magnetic field were also taken along the coil z-axis, through the center of the left coil winding. Again, the results show good agreement. The peak calculated field is greater than the measured value due to the coil windings being modeled as infinitely thin current loops, rather than a current distributed over a cross sectional area. The overall effect of this modeling simplification is not significant in regions where the mouse brain is located (> 0 mm on z-axis), as indicated in Figure 5.20. The coil surface is located at z = 0 mm.

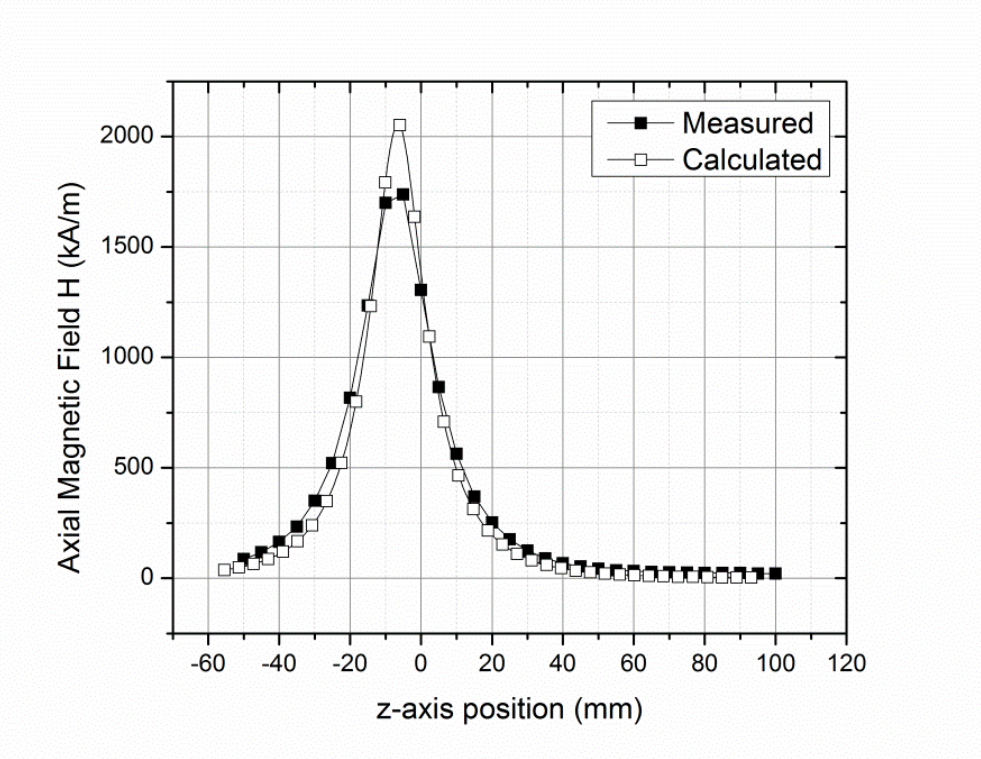

Figure 5.20. Measurement and calculation of axial magnetic field along z-axis, through center of left coil winding. The coil surface against which the subject's head is placed occurs at 0 mm on the z-axis.

Regions where neighboring tissues have a large difference in electrical conductivity are expected to create rapid changes in the induced electric field at the boundary. The calculated induced electric field in the cerebral hemisphere in a coronal plane bisecting the cerebral hemisphere of the anatomical mouse brain, below the center of the coil is shown in Figure 5.21 (a). The induced electric field decays from 132 V/m at the top of the cerebral hemisphere to 43 V/m at the bottom, as indicated in Figure 5.21 (b). Electric field values in the surrounding tissues are not indicated in order to emphasize the location of neural tissue. The highest value in the entire plane occurred at the air-skin interface, where the induced electric field has a magnitude of 150 V/m.

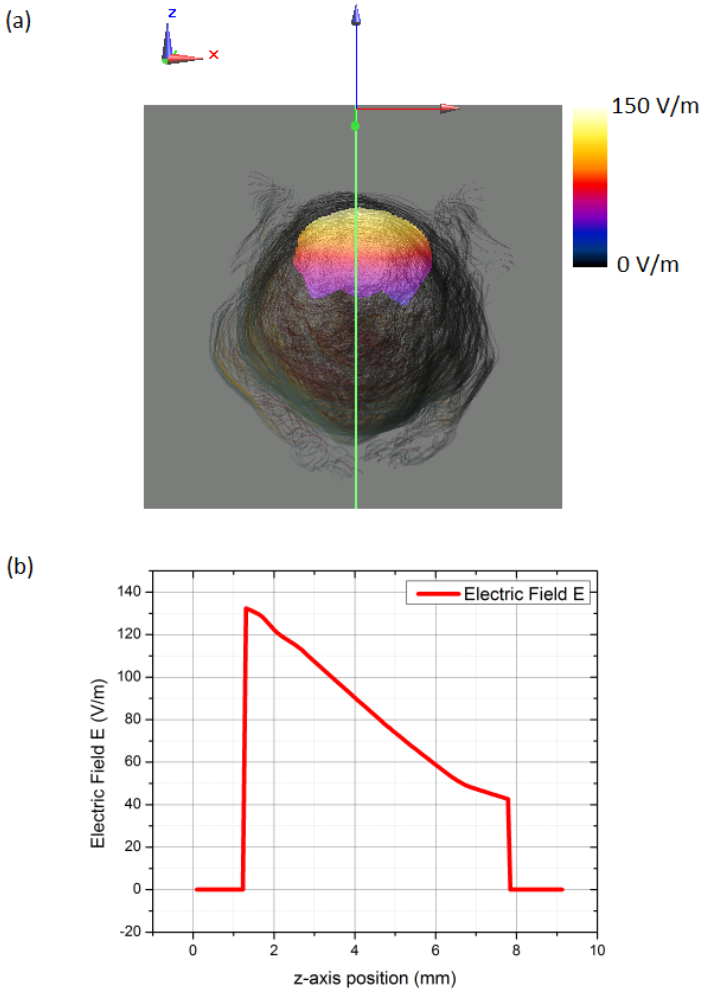

Figure 5.21. (a) Calculated induced electric field in coronal plane, bisecting the cerebral hemisphere of the anatomical mouse model, the modeled coil was positioned directly over the center of the cerebral hemisphere, and (b) electric field decay with depth in cerebral hemisphere. Electric field values in surrounding non-neural tissues are not plotted.

The electric field in the sagittal plane of the anatomical mouse brain is shown in Figure 5.22 (a). The peak electric field value in this plane is 143 V/m. The calculated electric field in the central transverse plane of the anatomical mouse model is shown in Figure 5.22 (b), with peak electric field value of 97 V/m. The electric field results indicate that much of the cerebral hemisphere will be stimulated with the commercial coil when operated at 100% output.

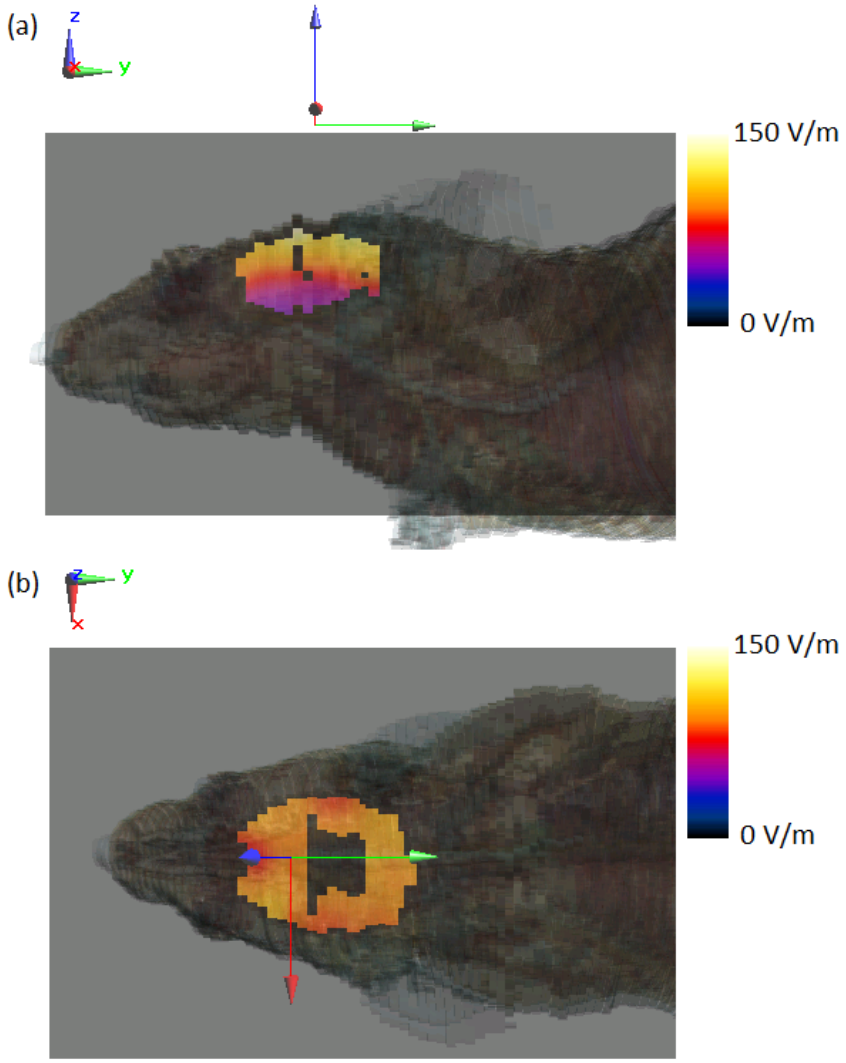

Figure 5.22. (a) Calculated induced electric field in sagittal and (b) transverse planes, bisecting the cerebral hemisphere of the anatomical mouse model.

The results highlight that it is difficult to achieve stimulation in only a small region in the brain with coils similar to the one utilized and modeled in this study. For this reason, novel coil designs must be created for this purpose. Studies for human subjects [11] have revealed that increased localization of stimulation is usually possible at the expense of depth of penetration. It is anticipated this will also be true for TMS coils designed for small animals.

References

[1] D. Cohen and B. N. Cuffin, "Developing a more focal magnetic stimulator. Part I: some basic principles," *J. Clin. Neurophysiol.*, vol. 8, no. 1, pp. 102–111, 1991.

[2] P. C. Miranda, M. Hallett, and P. J. Basser, "The electric field induced in the brain by magnetic stimulation: a 3-D finite-element analysis of the effect of tissue heterogeneity and anisotropy," *Biomed. Eng. IEEE Trans.*, vol. 50, no. 9, pp. 1074–1085, 2003.

[3] T. A. Wagner, M. Zahn, A. J. Grodzinsky, and A. Pascual-Leone, "Three-dimensional head model simulation of transcranial magnetic stimulation," *Biomed. Eng. IEEE Trans.*, vol. 51, no. 9, pp. 1586–1598, 2004.

[4] J. D. Weissman, C. M. Epstein, and K. R. Davey, "Magnetic brain stimulation and brain size: relevance to animal studies," *Electroencephalogr. Clin. Neurophysiol. Potentials Sect.*, vol. 85, no. 3, pp. 215–219, 1992.

[5] L. J. Crowther, I. C. Nlebedim, and D. C. Jiles, "Developments in deep brain stimulation using time dependent magnetic fields," *J. Appl. Phys.*, vol. 111, no. 7, p. 07B325, 2012.

[6] P. A. Hasgall, E. Neufeld, M. C. Gosselin, A. Klingenböck, and N. Kuster, "IT'IS Database for thermal and electromagnetic parameters of biological tissues," *Sept. 26th*, 2011.

[7] C. Gabriel, S. Gabriel, and E. Corthout, "The dielectric properties of biological tissues: I. Literature survey," *Phys. Med. Biol.*, vol. 41, no. 11, p. 2231, 1996.

[8] S. Gabriel, R. W. Lau, and C. Gabriel, "The dielectric properties of biological tissues: II. Measurements in the frequency range 10 Hz to 20 GHz," *Phys. Med. Biol.*, vol. 41, no. 11, p. 2251, 1996.

[9] S. Gabriel, R. W. Lau, and C. Gabriel, "The dielectric properties of biological tissues: III. Parametric models for the dielectric spectrum of tissues," *Phys. Med. Biol.*, vol. 41, no. 11, p. 2271, 1996.

[10] C. Gabriel, A. Peyman, and E. H. Grant, "Electrical conductivity of tissue at frequencies below 1 MHz," *Phys. Med. Biol.*, vol. 54, no. 16, p. 4863, 2009.

[11] L. J. Crowther, P. Marketos, P. I. Williams, Y. Melikhov, D. C. Jiles, and J. H. Starzewski, "Transcranial magnetic stimulation: Improved coil design for deep brain investigation," *J. Appl. Phys.*, vol. 109, no. 7, p. 07B314, 2011.

CHAPTER VI

RESULTS III: FORCES ON TMS COILS

6.1 Background

There has been a long-standing desire within the neural engineering community to combine a neuromodulation technique such as TMS with a neuroimaging technique such as functional magnetic resonance imaging (fMRI) [1]–[3]. Successfully combining these techniques would allow researchers to monitor the changes in brain activity during treatment and determine which regions have been stimulated. This capability would greatly improve our understanding of how TMS affects the brain and enhance the overall effectiveness of TMS in research and therapy. It would also experimentally solve the problem of determining the locus of stimulation during application.

The force experienced by a TMS coil during typical operation can be very high due to the large transient magnetic fields TMS coils generate. This force is made evident by the loud audible clicking sound the coil produces when stressed, which can potentially be harmful to the hearing of a subject if ear protection is not used. The force becomes even greater when the coil is in the presence of a large external field like that produced by an MRI magnet. As a result, some attempts at performing TMS and fMRI concurrently have led to failure of the coil. This is particularly problematic when high frequency TMS protocols are used, which are now capable of being utilized with a repetitive stimulation frequency of 100 Hz or more.

In this chapter the problem of forces on TMS coils is addressed. Combining TMS and fMRI also causes additional problems, principally artifacts in the resulting fMRI

image due to the presence of the TMS coil. This problem has been studied and mitigated to some extent by practice of an 'interleaved' procedure [4]–[6].

6.2 Numerical calculation of Lorentz forces on TMS coils

To understand how the presence of an external magnetic field affects the forces on a TMS coil, the forces that arise during normal operation with no external field will first be calculated. Once these forces have been established the calculation will then account for a large externally applied field of 3 T, comparable to that of a typical research MRI scanner. The changes in the forces on the coil will then be compared. The results of this investigation will allow inferences about safe operating levels and potential modifications to TMS coil construction to be made.

In this study, calculation of the fields generated by a TMS coil have been performed using finite element analysis software COMSOL Multiphysics 4.2a (COMSOL Inc., Burlington, MA, USA). Coils used for TMS are usually built from thick, rectangular cross-sectioned wire, concentrically wound to form a flat coil. In this study a typical figure-8 coil [7] has been modeled, similar to those widely used in research. The static currents and fields are considered such that the magnetic vector potential **A** satisfies equation (6.1),

$$\nabla \times (\mu^{-1} \nabla \times \vec{A}) = \vec{J}^{e} \tag{6.1}$$

where $\mathbf{J}^{e}$ denotes an applied current density. The relationship between the fields and potentials are described by (6.2) and (6.3) [8].

$$\vec{B} = \nabla \times \vec{A} \tag{6.2}$$

$$\vec{H} = \mu^{-1}\vec{B} \tag{6.3}$$

The current density of the wire was calculated by considering 9 turns of wire carrying 5 kA with an excitation frequency of 2.5 kHz. The cross sectional area of the wire was assumed to be 6 × 2 mm and the volume Lorentz force density was calculated by (6.4).

$$\vec{f} = \vec{J} \times (\vec{B}_{coil} + \vec{B}_{mri}) \tag{6.4}$$

The torque at the center of each winding was calculated as in (6.5),

$$\vec{\tau} = \int \vec{r} \times \vec{f}\, dV \tag{6.5}$$

where **r** is a vector pointing from the center of each coil winding to the corresponding Lorentz force density **f**.

Three different orientations of the applied field relative to the modeled figure-8 TMS coil have been considered. First, the external field is applied along the unique y-axis, such that it is perpendicular to the plane of the coil. Second, the external field is applied in the plane of the coil, perpendicular to the unique axis, where the field is aligned with the x-axis or length of the coil, such that it is parallel to a line connecting the center of the two coil windings. Third, the field is applied in the plane of the coil and aligned parallel to the z-axis or the width of the coil, which is perpendicular to a line connecting the center of the two coil windings. Each orientation is indicated in each case in Figures 6.2, 6.3, and 6.4.

Magnetic field characterization was completed to ensure the results of the magnetic field calculations correspond to measurements of the modeled coil. Axial magnetic field measurements were performed on a Magstim D70 (R) figure-8 coil. This coil is the basis for the model used in the following calculations. A Gaussmeter and axial

Hall probe with an active area of 0.46 mm^2, supported by a multi-axis linear stage with a movement precision of 0.6 μm was used to measure the magnetic field, which closely mirrored the calculated values. The figure-8 coil was energized with a Magstim Rapid^2 biphasic stimulator (The Magstim Company Ltd., Whitland, Wales, United Kingdom), with measured pulse duration of 400 μs.

The magnetic flux density distribution in the coil plane, caused by the current in the coil alone is shown in Figure 6.1 (a). The peak field intensity in the coil plane is approximately 1.9 T. The peak magnitude of the Lorentz force density when no external field is applied, the 'self force,' is approximately 7.3×10^8 N/m^3. The direction the Lorentz forces act in are shown in Figure 6.1 (b). It is known that the magnitude and direction of these forces do not cause mechanical failure of the coil.

The consequence of an applied field can now be investigated. First, the effect of orienting the applied 3 T field perpendicular to the modeled TMS coil was examined. In this case, the applied field was aligned with the y-axis of the coil model. The magnetic flux density distribution in the coil plane is shown in Figure 6.2 (a). It was observed that the peak field intensity present in the coil plane increased to approximately 4.9 T. The peak magnitude of the Lorentz force density was found to be approximately 1.85×10^9 N/m^3. This increase is significant when compared with the peak value of 7.3×10^8 N/m^3 calculated for the coil during normal operation, without an applied field. The directions in which the Lorentz forces act are indicated in Figure 6.2 (b). In this case, it is apparent the forces act in the coil plane. It can be observed that the Lorentz forces act inward or outward, radially, depending on the direction of current flow in the coil. The radial force

is higher when the magnetic field produced by the coil winding is in the same direction as the applied field. In Figure 6.2 (b), this is observed in the winding on the right.

The external field can be applied parallel to the coil plane in two different ways. First, the effect of the applied field oriented parallel to a line joining the centers of the two coil windings is considered. In this case, the field is oriented along the x-axis of the coil model, as indicated in Figure 6.3. The magnetic flux density distribution in the coil plane in this instance is shown in Figure 6.3 (a). It is observed that the peak magnetic flux density in the coil plane is approximately 3.6 T. This is considerably less than when the field is applied perpendicular to the coil plane, where a peak magnetic flux density of approximately 4.9 T was calculated. The peak magnitude of the Lorentz force density in this case is found to be 1.34×10^9 N/m^3, again lower than the previous case. The directions in which the Lorentz forces act are indicated in Figure 6.3 (b). For this orientation, the Lorentz forces act perpendicular to the coil plane, resulting in a flexural force about the mid point of the coil, where the two windings meet.

The applied field can also act parallel to the width of the TMS coil. In this case the applied field is oriented along the z-axis of the coil model as shown in Figure 6.4. The magnetic flux density distribution in the coil plane in this case is shown in Figure 6.4 (a). The peak magnetic flux density in the coil plane is calculated to be approximately 3.6 T. The peak magnitude of the Lorentz force in the coil when the external field is applied parallel to the model z-axis is calculated to be approximately 1.32×10^9 N/m^3. The directions in which the Lorentz forces act are indicated in Figure 6.4 (b). For this orientation of the applied field, the forces are found to act perpendicular to the coil plane, which results in a torsional force about the mid point of the coil.

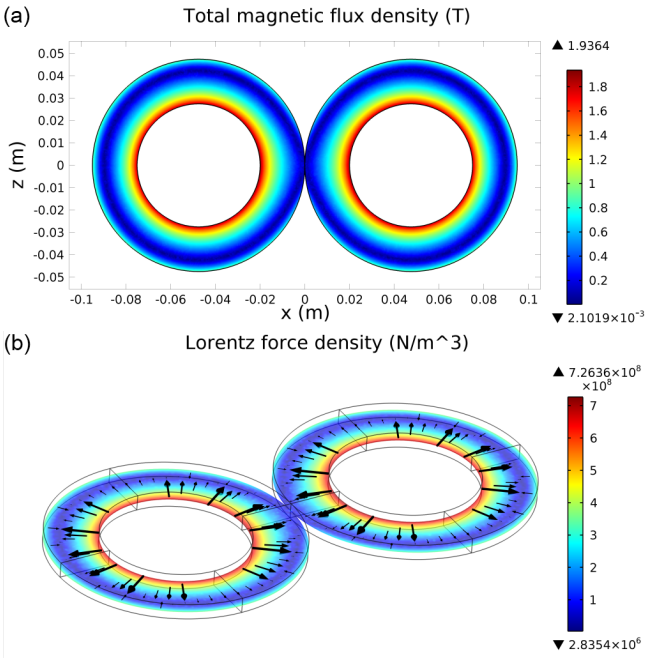

Figure 6.1. (a) Magnetic flux density inside modeled figure-8 coil with no external field applied and (b) resultant Lorentz forces on modeled figure-8 coil, arrows indicate direction of force.

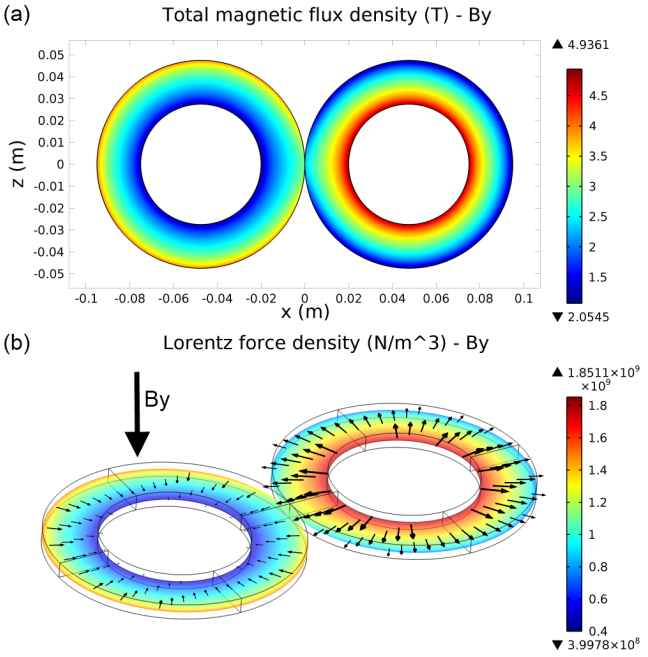

Figure 6.2. (a) Magnetic flux density inside modeled figure-8 coil with 3 T external field applied along the model y-axis, perpendicular to coil plane and (b) resultant Lorentz forces producing radial forces in the coil plane, arrows indicate direction of force.

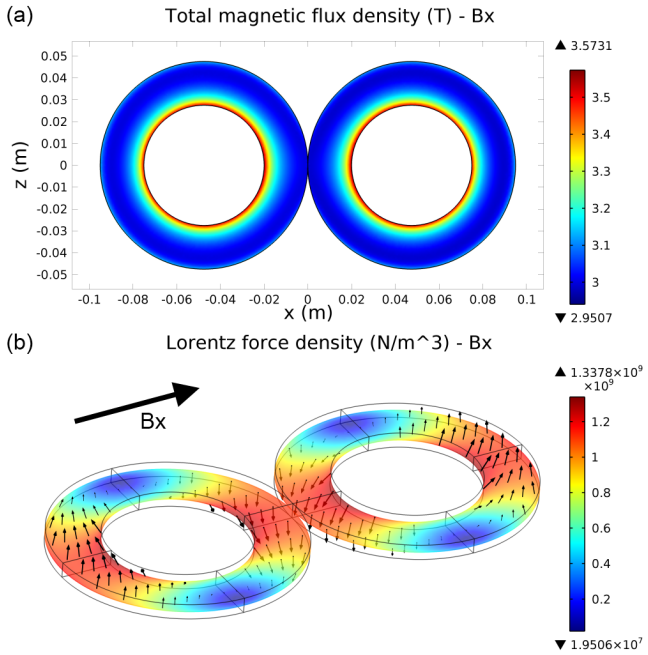

Figure 6.3. (a) Magnetic flux density inside modeled figure-8 coil with 3 T external field applied along the model x-axis, parallel to the coil plane and (b) resultant Lorentz forces producing a flexural force about the coil center, arrows indicate direction of force.

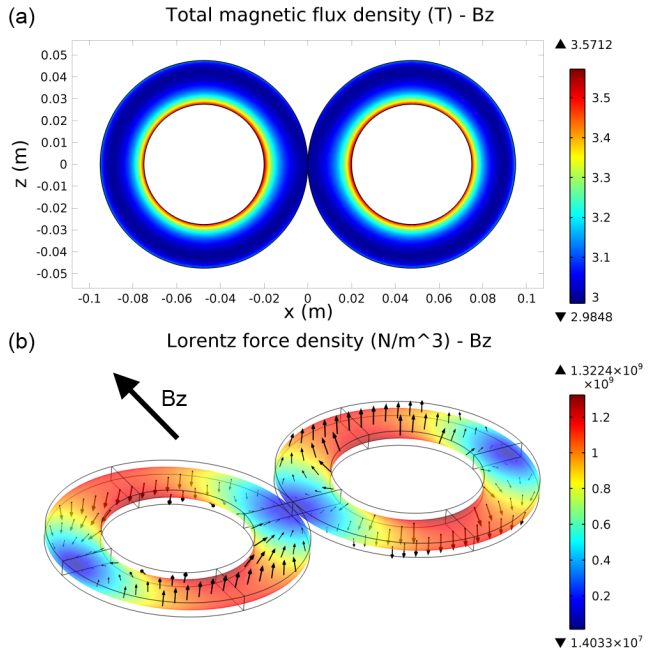

Figure 6.4. (a) Magnetic flux density inside modeled figure-8 coil with 3 T external field applied along the model z-axis, parallel to the coil plane and (b) resultant Lorentz forces producing a torsion force about the coil center, arrows indicate direction of force.

The forces experienced by the modeled TMS coil can be expressed as a torque calculated at the center of the coil windings. The following torque values have been calculated by (6.5) and are shown in Table 6.1. It is evident that when the applied field acts parallel to the coil plane, large counteracting torques are experienced, of approximately 610 Nm.

Table 6.1. Torque values for three orientations of applied magnetic field, perpendicular (B_y), and parallel (B_x and B_z) to the modeled coil plane.

	τ_x (Nm)	τ_y (Nm)	τ_z (Nm)
B_y (perpendicular)			
Right turn	3×10^{-3}	-8×10^{-6}	3×10^{-3}
Left turn	4×10^{-3}	9×10^{-7}	4×10^{-3}
B_x (parallel)			
Right turn	3×10^{-3}	-5×10^{-6}	-610.54
Left turn	4×10^{-3}	-3×10^{-6}	610.54
B_z (parallel)			
Right turn	610.55	-4×10^{-6}	3×10^{-3}
Left turn	-610.54	-2×10^{-6}	4×10^{-3}

The Lorentz forces experienced by the coil have been determined for normal operation and for three orientations of an applied 3 T field, such as the main field produced by an MRI magnet. The results indicate that under usual operating circumstances, the Lorentz force density on a TMS coil can exceed 7.3×10^8 N/m^3. The addition of a large applied field causes the Lorentz force density to increase to 1.85×10^9 N/m^3. The torque experienced at the center of the coil windings has also been calculated

and can exceed 600 Nm. The nature of the force experienced by the TMS coil depends on the direction of the applied field, relative to the orientation of the coil.

The findings of this study indicate the nature of the forces that act upon the coil must be considered, as the orientation of the coil relative to the applied field has an effect on the peak Lorentz force density generated. It is possible that shielding of the coil may reduce the forces generated but this is likely to make stimulation of neural tissue difficult.

6.3 Realistic coil modeling and calculation of stress

The preceding section indicated that the forces that act upon a TMS coil increase significantly with the addition of an externally applied field. To gain a greater understanding of these forces a geometrically realistic coil model must be used. In addition to calculating the Lorentz force density **f** inside the coil by (6.6),

$$\vec{f} = \vec{J} \times \vec{B} \tag{6.6}$$

where **J** is the current density and **B** is the magnetic flux density, we can also calculate stress inside the coil. This requires the components of the Maxwell stress tensor $T_{i,j}$ to be calculated by (6.7) [9],

$$T_{i,j} = \varepsilon_0 \left(E_i E_j - \frac{1}{2}\delta_{i,j} E^2 \right) + \frac{1}{\mu_0}\left(B_i B_j - \frac{1}{2}\delta_{i,j} B^2 \right) \tag{6.7}$$

where ε_0 and μ_0 are the relative permittivity and permeability, respectively, and $\delta_{i,j}$ is the Kronecker delta, which is equal to one if i = j. In this case the stress tensor depends only on a component of the electromagnetic field as no external mechanical stress or deformation is applied to the coil. Therefore, the mechanical part can be assumed to be

zero. Using the Maxwell stress tensor, the von Mises stress can be calculated as in (6.8) [10].

$$\sigma_v = \sqrt{\frac{1}{2}\left[(T_{xx}-T_{yy})^2+(T_{yy}-T_{zz})^2+(T_{zz}-T_{xx})^2\right]+3\left[T_{xy}^2+T_{xz}^2+T_{yz}^2\right]} \qquad (6.8)$$

To investigate the influence of skin effect and the overall change in magnetic flux density in the coil when considering the problem in an AC case as opposed to the DC case, an initial two-dimensional axisymmetric simulation has been performed. These calculations assume a current of 5 kA in the simulated copper medium having electrical conductivity 5.998×10^7 S/m, and a surrounding air region with electrical conductivity 0 S/m. The AC case assumed an excitation frequency of 2.5 kHz. The modeled coil consisted of nine turns with inner and outer radii of 32 and 48 mm, respectively. The separation between windings to account for an air gap and insulation was 1 mm. A cross-sectional area of 1×5 mm was assumed for the wire. The underlying rotational symmetry of this model allows a very fine mesh to be applied to the model. As anticipated, in the AC case it was found that the skin effect has an effect on the overall current distribution inside the coil windings however, the majority of the coil cross section has an instantaneous current density of approximately 1×10^9 A/m^2. This corresponds to the current density found in the DC case. The resulting magnetic flux density in both cases is shown in Figure 6.5, demonstrating an almost identical profile. These results indicate that the calculation can be modeled in the DC case as this greatly reduces the computational requirements of the simulation for the realistic three-dimensional coil model.

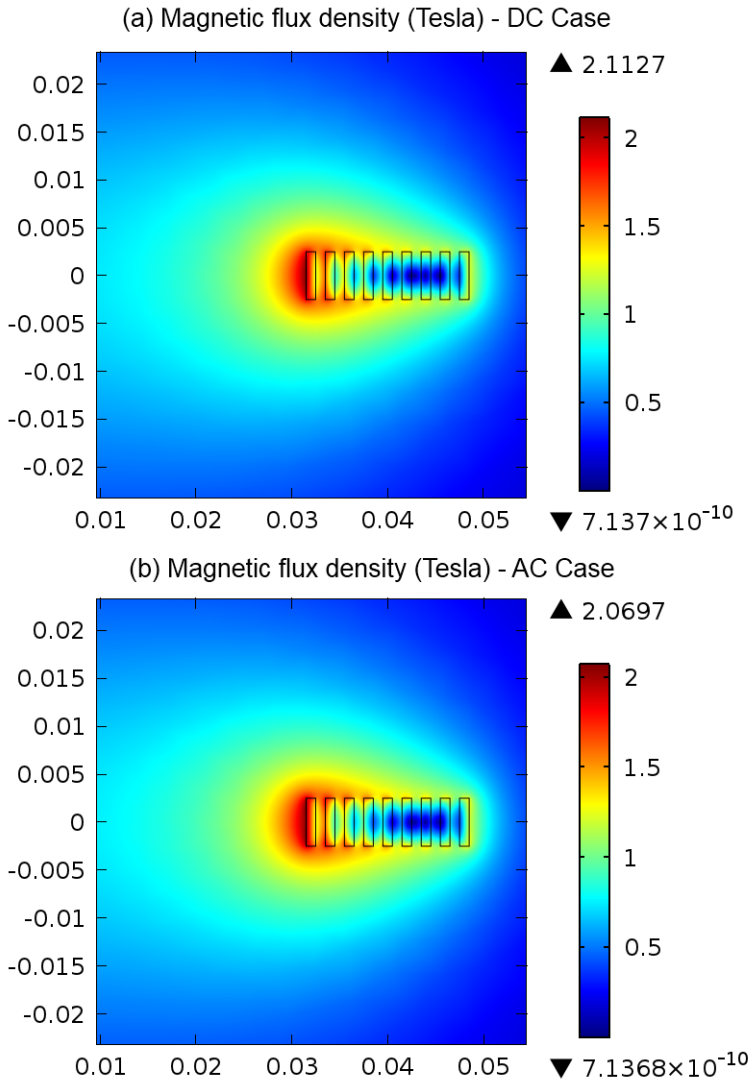

Figure 6.5. Axisymmetric simulation of magnetic flux density produced by modeled circular TMS coil in (a) DC and (b) AC case, resulting in almost identical results.

A figure-8 TMS coil was modeled with SolidWorks 2011 (SolidWorks Corp., Waltham, MA, USA) based on x-ray images of the commercially available Magstim D70 (R) figure-8 coil, shown in Figure 6.6. All calculations were performed with COMSOL Multiphysics 4.2a (COMSOL, Inc., Burlington, MA, USA) with an assumed current of 5 kA flowing in the copper wire with electrical conductivity 5.998×10^7 S/m.

Again, the effect of an externally applied field has been considered in a number of orientations relative to the modeled coil. First, the forces and stress generated without an applied field are investigated. The magnetic flux density distribution in the coil plane, as a result of only the current in the coil is shown in Figure 6.7 (a). The peak field intensity in the coil plane is approximately 2.3 T. The peak magnitude of the Lorentz force density in the coil when no external field is applied was found to be 2.8×10^9 N/m^3. The directions in which the Lorentz forces act are indicated in Figure 6.7 (b). The peak von Mises stress in this case was found to be approximately 4.3×10^6 Pa, as indicated in Figure 6.7 (c). The largest von Mises stresses are located in the inner-most turn of the coil windings.

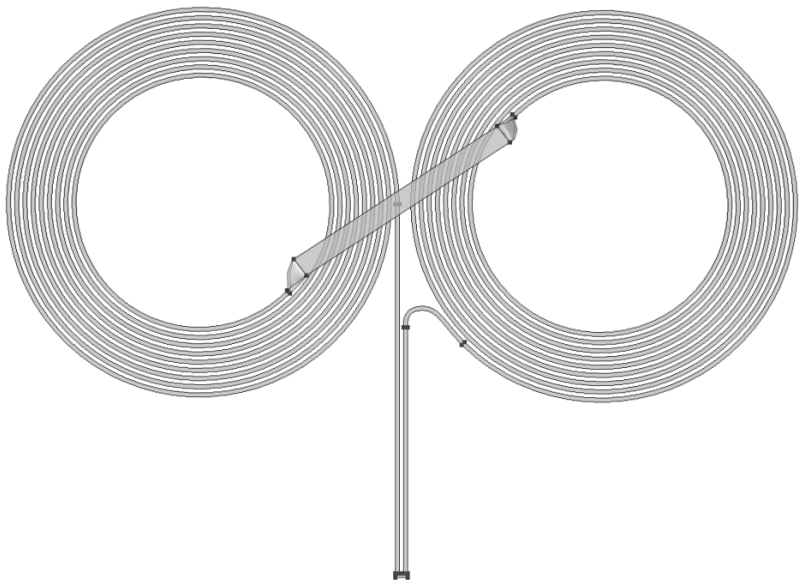

Figure 6.6. Geometrically realistic three-dimensional figure-8 coil model developed in SolidWorks 2011, with use of x-ray images of a commercial TMS coil.

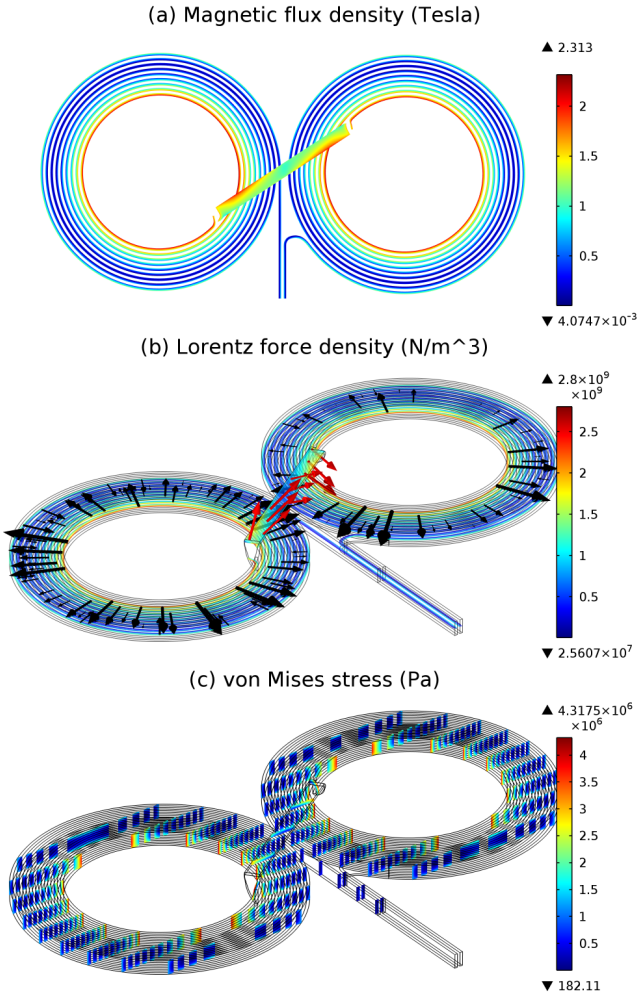

Figure 6.7. (a) Magnetic flux density inside realistically modeled figure-8 coil with no external magnetic field applied, (b) resultant Lorentz force density, and (c) von Mises stresses.

The effect of orienting the applied field perpendicular to the realistically modeled TMS coil will be considered first. The external field in this case is aligned with the unique z-axis of the coil model as indicated in Figure 6.8. The magnetic flux density distribution in the coil plane is shown in Figure 6.8 (a). The peak field intensity calculated in this case has increased to approximately 5.3 T. The peak amplitude of the Lorentz force density in the coil when the external field is applied perpendicular to the coil plane was found to be approximately 6.4×10^9 N/m^3. The Lorentz force density has more than doubled due to the external field in this case. The directions in which the

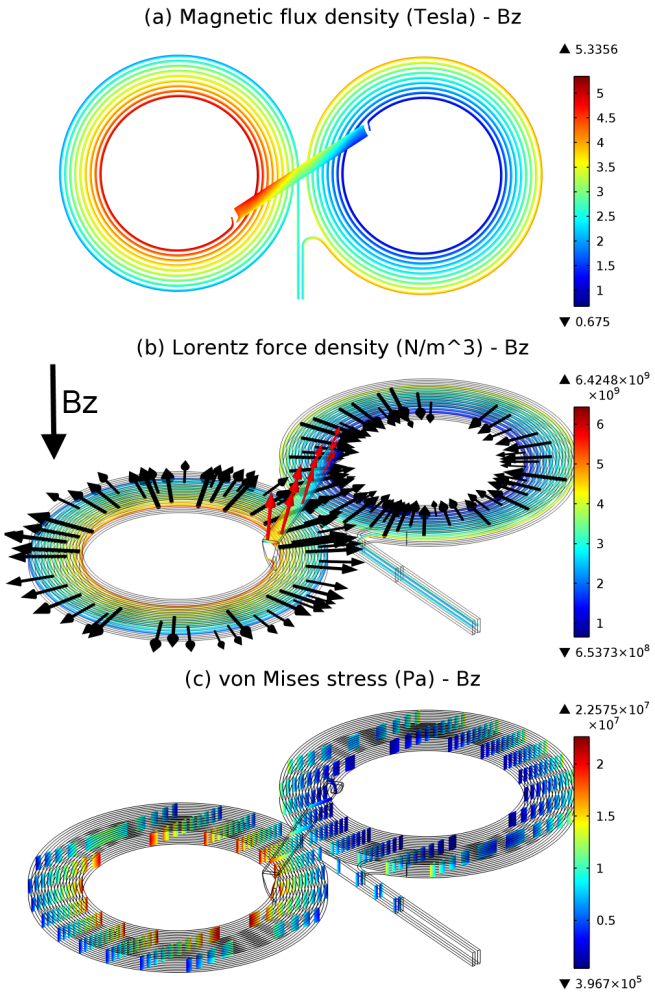

Figure 6.8. (a) Magnetic flux density inside realistically modeled figure-8 coil with 3 T external field applied along the model z-axis, perpendicular to the coil plane and (b) resultant Lorentz force density producing radial forces in the coil plane and (c) von Mises stresses.

Lorentz forces act are indicated in Figure 6.8 (b). In this scenario, the Lorentz forces act in the coil plane, radially inward or outward, depending on the direction of current flow in the modeled coil. The peak von Mises stress was found to be approximately 2.3×10^7 Pa as indicated in Figure 6.8 (c). The largest von Mises stresses were located in either the inner-most turn of the coil windings or the outermost, depending on the direction of the Lorentz forces.

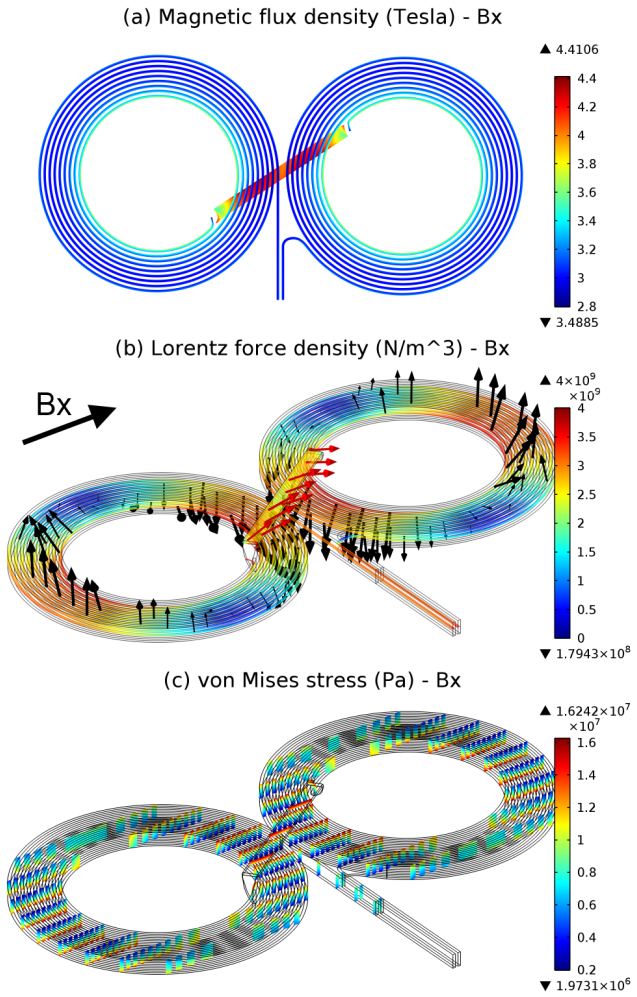

Figure 6.9. (a) Magnetic flux density inside realistically modeled figure-8 coil with 3 T external field applied along the model x-axis, parallel to the coil plane and (b) resultant Lorentz force density producing a flexural force about the coil center and (c) von Mises stresses.

As before, the applied field can be oriented parallel to the coil plane in two distinct ways. First, the effect of the applied field operating parallel to the line joining the centers of the two windings is investigated. In this case the field is oriented along the x-axis of the coil model as shown in Figure 6.9. The magnetic flux density distribution in the coil plane in this case is shown in Figure 6.9 (a). The peak magnetic flux density in the coil plane is approximately 4.4 T. This is significantly lower than in the magnetic flux

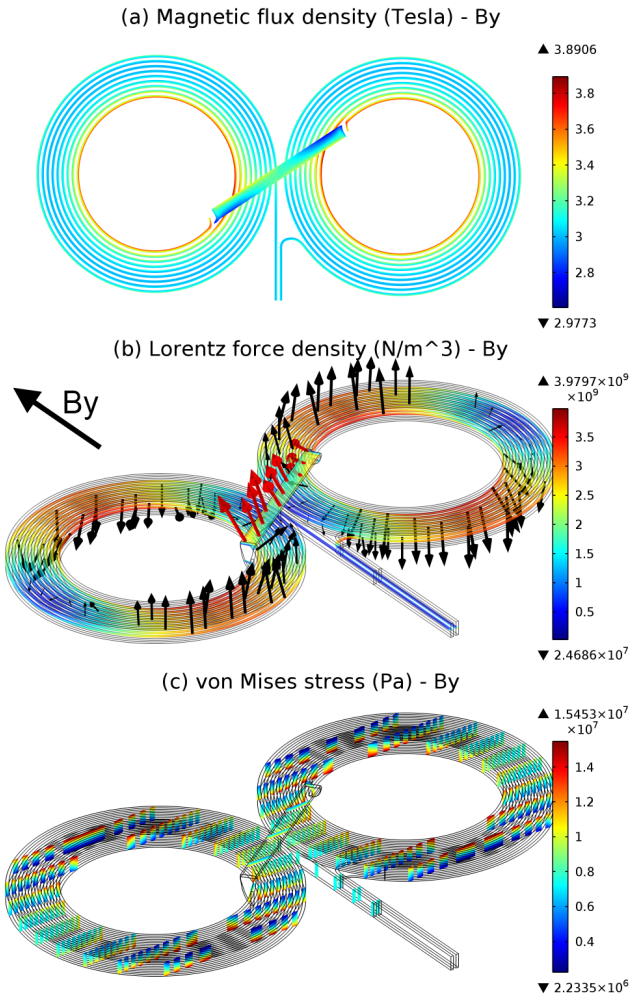

Figure 6.10. (a) Magnetic flux density inside realistically modeled figure-8 coil with 3 T external field applied along the model y-axis, parallel to the coil plane and (b) resultant Lorentz force density producing a torsional force about the coil center and (c) von Mises stresses.

density found when the field is applied perpendicular to the coil plane, where a peak magnetic flux density of approximately 5.3 T was calculated. The peak Lorentz force density is calculated to be 4.0×10^9 N/m^3, also lower than the previous case. The directions in which the Lorentz forces act are indicated in Figure 6.9 (b). In this case, the Lorentz forces create a flexural force about the mid point of the coil. The largest von Mises stress is approximately 1.6×10^7 Pa with higher stresses generally found in the top

or bottom surface of the coil, depending on which direction the current flows in the coil, relative to the model x-axis as indicated in in Figure 6.9 (c).

Lastly, the applied field is oriented parallel to the width of the modeled TMS coil, so that the applied field is oriented along the y-axis of the coil model as indicated in Figure 6.10. The magnetic flux density distribution in the coil plane in this shown in Figure 6.10 (a). The peak magnetic flux density in the coil plane is found to be approximately 3.9 T. The peak Lorentz force density calculated in this case is approximately 4.0×10^9 N/m^3. The directions in which the Lorentz forces act are indicated in Figure 6.10 (b). In this scenario, the Lorentz forces are found to act perpendicular to the coil plane, resulting in a torsional force about the center of the coil. The largest von Mises stress calculated is approximately 1.5×10^7 Pa, with high stresses generally occurring on the top or bottom surface of the coil, depending on the direction of the current flow, relative to the model x-axis, as indicated in Figure 6.10 (c).

The peak magnitude of the calculated Lorentz forces in all instances is below the 70 MPa yield strength of copper, therefore, it is not anticipated that the coil will plastically deform or fracture. However, the TMS coil casing should be selected such that it should have yield strength greater than 23 MPa. As the coil can potentially experience large elastic deformation, low cycle fatigue should be considered as this may have the potential to lead to coil failure. The peak calculated magnetic flux density and Lorentz force density found in this study and the earlier study utilizing simplified coil geometry is given in Table 6.2. As values of von Mises stress were not calculated in the prior study with simplified geometry, they cannot be compared to the realistic geometry.

The results of this study show that under typical conditions the peak Lorentz force density in a TMS coil can exceed 2.8×10^9 N/m^3. The addition of an applied 3 T field can increase the Lorentz force density to more than 6.4×10^9 N/m^3. The realistically modeled coil indicates that the peak Lorentz force density is more than three times larger than had previously been calculated with a simplified coil geometry. The maximum Lorentz force density calculated with the simplified model, in the presence of a 3 T applied field was 1.9×10^9 N/m^3, much less than the stresses calculated using the realistic model. The maximum von Mises stress encountered with an applied 3 T field is 2.3×10^7 Pa.

The methodology and results of this study can be used in the implementation of combined TMS/fMRI systems by increasing the understanding of how the devices interact and what the actual forces are. The results can also be used in future development of novel TMS coils to prevent mechanical failure in extreme conditions.

Table 6.2. Peak calculated magnetic flux density and Lorentz force for orientations of applied field.

	Simplified Geometry		**Realistic Geometry**	
	Max Magnetic Flux Density (T)	**Max Lorentz Force (Nm^{-3})**	**Max Magnetic Flux Density (T)**	**Max Lorentz Force (Nm^{-3})**
B_0	1.9	7.26×10^8	2.3	2.80×10^9
B_x	3.6	1.34×10^9	4.4	4.00×10^9
B_y	3.6	1.32×10^9	3.9	4.98×10^9
B_z	4.9	1.85×10^9	5.3	6.42×10^9

References

[1] M. F. S. Rushworth, K. A. Hadland, T. Paus, and P. K. Sipila, "Role of the human medial frontal cortex in task switching: a combined fMRI and TMS study," *J. Neurophysiol.*, vol. 87, no. 5, pp. 2577–2592, 2002.

[2] D. Bohning, A. Shastri, K. McConnell, Z. Nahas, J. Lorberbaum, D. Roberts, C. Teneback, D. Vincent, and M. George, "A combined TMS/fMRI study of intensity-dependent TMS over motor cortex," *Biol. Psychiatry*, vol. 45, no. 4, pp. 385–394, 1999.

[3] J. Reithler, J. C. Peters, and A. T. Sack, "Multimodal transcranial magnetic stimulation: using concurrent neuroimaging to reveal the neural network dynamics of noninvasive brain stimulation," *Prog. Neurobiol.*, vol. 94, no. 2, pp. 149–165, 2011.

[4] S. Denslow, M. Lomarev, M. S. George, and D. E. Bohning, "Cortical and subcortical brain effects of transcranial magnetic stimulation (TMS)-induced movement: an interleaved TMS/functional magnetic resonance imaging study," *Biol. Psychiatry*, vol. 57, no. 7, pp. 752–760, 2005.

[5] M. Moisa, R. Pohmann, L. Ewald, and A. Thielscher, "New coil positioning method for interleaved transcranial magnetic stimulation (TMS)/functional MRI (fMRI) and its validation in a motor cortex study," *J. Magn. Reson. Imaging*, vol. 29, no. 1, pp. 189–197, 2009.

[6] X. Li, C. C. Tenebäck, Z. Nahas, F. A. Kozel, C. Large, J. Cohn, D. E. Bohning, and M. S. George, "Interleaved transcranial magnetic stimulation/functional MRI confirms that lamotrigine inhibits cortical excitability in healthy young men.," *Neuropsychopharmacol. Off. Publ. Am. Coll. Neuropsychopharmacol.*, vol. 29, no. 7, pp. 1395–1407, 2004.

[7] S. Ueno, T. Tashiro, and K. Harada, "Localized stimulation of neural tissues in the brain by means of a paired configuration of time-varying magnetic fields," *J. Appl. Phys.*, vol. 64, no. 10, pp. 5862–5864, 1988.

[8] J. D. Jackson, *Classical electrodynamics*, vol. 3. Wiley New York etc., 1962.

[9] D. J. Griffiths and R. College, *Introduction to electrodynamics*, vol. 3. Prentice hall Upper Saddle River, NJ, 1999.

[10] P. Kurowski, *Engineering Analysis with SolidWorks Simulation 2013*. SDC publications, 2013.

CHAPTER VII

CONCLUSIONS

7.1 Anatomically realistic human head modeling

The impact of human head model complexity on accurate determination of the locus of neural stimulation during TMS has been studied. Numerical methods have been utilized, supported by empirical measurements, to demonstrate that tissue heterogeneity has a significant effect on the distribution of electric field induced in the brain during TMS. It has been proven that simplified human head models are inadequate for accurate determination of induced electric field, particularly at depth in the brain.

The inhomogeneous head models have demonstrated that significant spatial variation of the induced electric field can occur between subjects, as the physical characteristics each brain is different, particularly with age. The consequence of this discovery is that a particular TMS coil may not be able to accurately stimulate the same brain region for different patients. These results also highlight the value of neuronavigation in TMS trials, to ensure the desired cortical target has the maximum likelihood of being stimulated.

7.2 Coil design for transcranial magnetic stimulation

One of the main challenges in TMS is developing the ability to stimulate neural tissue at depth in the brain. Currently this requires invasive surgery and implantation of DBS electrodes. Replacing this procedure with a non-invasive, magnetic therapy would

provide significant benefits, reducing the cost and eliminating the risks associated with surgery.

The design of existing TMS coils have been investigated and quantitatively compared. The results of this analysis revealed that a trade-off exists between the depth and localization of stimulation and that it is not presently possible to stimulate brain tissue at depth without stimulating the overlying brain regions.

A novel coil design, the 'Halo' coil, has been proposed and demonstrated as an improved penetration depth over standard TMS coils through calculations and magnetic field measurements. The Halo coil is significantly different from standard TMS coils designs as it makes use of multiple coils, requiring two magnetic stimulators to operate. The Halo coil is also large enough to place over a subject's head, creating new stimulation possibilities. The results show promise for expanding the implementation and development of TMS for diagnostic and therapeutic applications as it provides substantial advantages over alternative invasive methods of stimulating neural tissue at depth in the brain.

7.3 Forces on transcranial magnetic stimulation coils

The forces generated when combining TMS with neuroimaging techniques such as fMRI have been investigated. The magnetic flux density, Lorentz force density, and von Mises stress experienced by a commercial figure-8 TMS coil have been calculated during normal operation and when in the presence of a 3 T external field, such as can be found in an fMRI scanner. Accurate geometrical modeling of the device demonstrated

that an externally applied 3 T field can increase the Lorentz force density by a factor of more than 3 times higher than had previously been established. The results of this study have implications for the development of combined TMS/fMRI systems and in the development of new TMS coil designs and construction methods to ensure mechanical failure does not occur.

CHAPTER VIII

FUTURE WORK

8.1 Advanced modeling of transcranial magnetic stimulation, future devices and applications

Much of the work described in this thesis makes use of the best available dielectric tissue property database. Many of the sources in this database are results of measurements performed at significantly higher frequencies than applies to TMS and many have been conducted on tissue from small animals. To ensure the validity of these values, dielectric tissue property measurements should be conducted specifically for use in TMS on the most suitable tissue to emulate the properties of living human tissue. Additionally, the effect of various neurological disorders on the tissue properties of the brain should be investigated so that accurate modeling of unhealthy patients can be achieved.

The work that has been presented on anatomically realistic human head modeling makes significant advances over other TMS studies that make use of simplified human head models. However, there are still ways in which these models could be improved. Consideration of anisotropic materials in the head, particularly the white matter, would improve accurate determination of induced fields in the brain. This will become increasingly important as advances in deep TMS are made. Incorporation of diffusion tensor imaging (DTI) data could also potentially model the connectivity of the brain and enable modeling of how neural stimulation propagates through the brain after the initial stimulation.

The results of anatomically realistic human head modeling have demonstrated the extent to which induced fields can vary between patients and depend upon coil positioning. Existing neuronavigation systems allow a TMS practitioner to target a particular region of the cortex by seeing where the coil is located relative to the subject's structural MRI data and ensure coil position is repeatable. However, these systems assume stimulation will occur directly beneath the coil center with no indication of how the stimulating field will be induced in the brain. Incorporating the modeling techniques demonstrated in this thesis will allow the practitioner to see how the induced field will be distributed in the head. As a result, the distribution of the induced field will be indicated to the user and offers scope for improvement to stimulation by suggesting better positioning of the coils. A challenge of this proposed system will be the computational time required to model the induced field during use. High-resolution modeling can take hours to compute while low-resolution modeling may not identify important features of the induced field. One possible solution to this problem would be to compute the induced field with the subject's MRI data for various coil positions prior to use and indicate the most relevant result during treatment.

Continued development of novel TMS devices will enable new applications of the technique to be established. Advances and improvements in the stimulation depth achievable with TMS may ultimately enable it to replace invasive neuromodulation methods such as DBS, which is currently used for the treatment of the motor symptoms of Parkinson's disease. Future studies of TMS may reveal utility in treatment of additional neurological disorders and injuries such concussion, traumatic brain injury and chronic traumatic encephalopathy.

APPENDIX A

DIELECTRIC TISSUE PROPERTIES

Low Frequency Electrical Conductivity Values (S/m)						
Tissue	**Average**	**Standard Deviation**	**Number of Values**	**Min**	**Max**	**Direction**
Cerebellum	1.21	0.10	2	1.12	1.31	Along
Cerebellum	0.31	0.09	2	0.22	0.40	Across
Cerebellum	0.58	0.36	7	0.10	1.31	Mixed
Brain (White Matter)	0.80	0.33	2	0.47	1.12	Along
Brain (White Matter)	0.10	0.02	2	0.08	0.12	Across
Brain (White Matter)	0.37	0.34	5	0.05	1.12	Mixed
Brain (Grey Matter)	0.26	0	1	0.26	0.26	Along
Brain (Grey Matter)	0.20	0	1	0.20	0.20	Across
Brain (Grey Matter)	0.19	1	4	0.08	0.26	Mixed
Liver	0.09	0.03	4	0.04	0.14	
Heart Muscle	0.39	0.00	1	0.39	0.39	Along
Heart Muscle	0.18	0.00	1	0.18	0.18	Across
Heart Muscle	0.29	0.13	5	0.08	0.48	Mixed
Bone	0.17	0	1	0.17	0.17	Along
Bone	0.10	1	2	0.02	1.17	Mixed
Skin (Dry)	0.000125	0.000075	2	0.00005	0.000	
Skin (Wet)	0.001215	0.000785	2	0.00043	0.002	
Cerebrospinal Fluid	1.80	0.21	2	1.59	2.00	
Blood	0.65	0.05	2	0.60	0.70	
Urine	1.71	0.16	2	1.55	1.87	
Lung (Inflated)	0.06	0.01	2	0.04	0.07	
Lung (Deflated)	0.16	0.05	2	0.11	0.21	

Muscle	0.13	0.06	3	0.04	0.19	Along
Muscle	0.41	0.13	4	0.15	0.60	Across
Muscle	0.29	0.18	7	0.04	0.60	Mixed
Fat	0.05	0.03	2	0.02	0.078	

Dielectric Properties															
Tissue	**ef**	**del1**	**tau1 (ps)**	**alf1**	**del2**	**tau2 (ns)**	**alf2**	**sig**	**del3**	**tau3 (µs)**	**alf3**	**del4**	**tau4 (ms)**	**alf4**	**Source**
Adrenal Gland	4	55	7.958	0.1	2500	159.155	0.1	0.5	100000	159.155	0.2	40000000	15.915	0	Thyroid gland
Air	1	0	0	0	0	0	0	0	0	0	0	0	0	0	Air
Bile	4	66	7.579	0.05	50	1.592	0	1.4	0	159.155	0.2	0	15.915	0.2	Bile
Blood	4	56	8.377	0.1	5200	132.629	0.1	0.7	0	159.155	0.2	0	15.915	0	Blood
Blood Vessel Wall	4	40	8.842	0.1	50	3.183	0.1	0.25	100000	159.155	0.2	10000000	1.592	0	Aorta Wall
Bone	2.5	10	13.263	0.2	180	79.577	0.2	0.02	5000	159.155	0.2	100000	15.915	0	Bone (Cortical)
Bone (Cancellous)	2.5	18	13.263	0.22	300	79.577	0.25	0.07	20000	159.155	0.2	20000000	15.915	0	Bone (Cancellous)
Bone (Cortical)	2.5	10	13.263	0.2	180	79.577	0.2	0.02	5000	159.155	0.2	100000	15.915	0	Bone (Cortical)
Bone Marrow (Red)	2.5	9	14.469	0.2	80	15.915	0.1	0.1	10000	1591.549	0.1	2000000	15.915	0.1	Bone Marrow (Red)
Bone Marrow (Yellow)	2.5	3	7.958	0.2	25	15.915	0.1	0.001	5000	1591.549	0.1	2000000	15.915	0.1	Bone Marrow (Yellow)
Brain	4	40	7.958	0.1	700	15.915	0.15	0.04	200000	106.103	0.22	45000000	5.305	0	Cerebellum
Brain (Grey Matter)	4	45	7.958	0.1	400	15.915	0.15	0.02	200000	106.103	0.22	45000000	5.305	0	Brain (Grey Matter)
Brain (White Matter)	4	32	7.958	0.1	100	7.958	0.1	0.02	40000	53.052	0.3	35000000	7.958	0.02	Brain (White Matter)
Breast Fat	2.5	3	17.68	0.1	15	63.66	0.1	0.01	50000	454.7	0.1	20000000	13.26	0	Breast Fat
Breast Gland	4	55	7.958	0.1	2500	159.155	0.1	0.5	100000	159.155	0.2	40000000	15.915	0	Thyroid gland
Bronchi	2.5	38	7.958	0.1	400	63.662	0.1	0.3	50000	15.915	0.2	1000000	15.915	0	Trachea
Bronchi lumen	1	0	0	0	0	0	0	0	0	0	0	0	0	0	Bronchi lumen
Cartilage	4	38	13.263	0.15	2500	144.686	0.15	0.15	100000	318.31	0.1	40000000	15.915	0	Cartilage
Cerebellum	4	40	7.958	0.1	700	15.915	0.15	0.04	200000	106.103	0.22	45000000	5.305	0	Cerebellum
Cerebrospinal Fluid	4	65	7.958	0.1	40	1.592	0	2	0	159.155	0	0	15.915	0	Cerebrospinal Fluid
Cervix	4	45	7.958	0.1	200	15.915	0.1	0.3	150000	106.103	0.18	40000000	1.592	0	Cervix
Commissura Anterior	4	32	7.958	0.1	100	7.958	0.1	0.02	40000	53.052	0.3	35000000	7.958	0.02	Brain (White Matter)

Commissura Posterior	4	32	7.958	0.1	100	7.958	0.1	0.02	40000	53.052	0.3	35000000	7.958	0.02	Brain (White Matter)
Connective Tissue	4	42	12.243	0.1	60	6.366	0.1	0.25	60000	318.31	0.22	20000000	1.326	0	Tendon\Ligament
Diaphragm	4	50	7.234	0.1	7000	353.678	0.1	0.2	1200000	318.31	0.1	25000000	2.274	0	Muscles
Ductus Deferens	4	40	8.842	0.1	50	3.183	0.1	0.25	100000	159.155	0.2	10000000	1.592	0	Aorta Wall
Dura	4	40	7.958	0.15	200	7.958	0.1	0.5	10000	159.155	0.2	1000000	15.915	0	Dura
Epididymis	4	55	7.958	0.1	5000	159.155	0.1	0.4	100000	159.155	0.2	40000000	15.915	0	Testis
Esophagus	4	60	7.958	0.1	2000	79.577	0.1	0.5	100000	159.155	0.2	40000000	15.915	0	Stomach
Esophagus Lumen	1	0	0	0	0	0	0	0	0	0	0	0	0	0	Esophagus Lumen
Eye (Cornea)	4	48	7.958	0.1	4000	159.155	0.05	0.4	100000	15.915	0.2	40000000	15.915	0	Eye (Cornea)
Eye (Lens)	3	32	8.842	0.1	100	10.61	0.2	0.2	1000	15.915	0.2	5000	15.915	0	Eye (Lens)
Eye (Sclera)	4	50	7.958	0.1	4000	159.155	0.1	0.5	100000	159.155	0.2	5000000	15.915	0	Eye (Sclera)
Eye (Vitrous Humor)	4	65	7.234	0	30	159.155	0.1	1.5	0	159.155	0	0	15.915	0	Eye (Vitrous Humor)
Eye Lens (Cortex)	4	42	7.958	0.1	1500	79.577	0.1	0.3	200000	159.155	0.1	40000000	15.915	0	Eye Lens (Cortex)
Eye Lens (Nucleus)	3	32	8.842	0.1	100	10.61	0.2	0.2	1000	15.915	0.2	5000	15.915	0	Eye (Lens)
Fat	2.5	9	7.958	0.2	35	15.915	0.1	0.035	33000	159.155	0.05	10000000	15.915	0.01	Fat (Average Infiltrated)
Fat (Average Infiltrated)	2.5	9	7.958	0.2	35	15.915	0.1	0.035	33000	159.155	0.05	10000000	15.915	0.01	Fat (Average Infiltrated)
Fat (Not Infiltrated)	2.5	3	7.958	0.2	15	15.915	0.1	0.01	33000	159.155	0.05	10000000	7.958	0.01	Fat (Not Infiltrated)
Gallbladder	4	55	7.579	0.05	40	1.592	0	0.9	1000	159.155	0.2	10000	15.915	0	Gallbladder
Heart Lumen	4	56	8.377	0.1	5200	132.629	0.1	0.7	0	159.155	0.2	0	15.915	0	Blood
Heart Muscle	4	50	7.958	0.1	1200	159.155	0.05	0.05	450000	72.343	0.22	25000000	4.547	0	Heart Muscle
Hippocampus	4	45	7.958	0.1	400	15.915	0.15	0.02	200000	106.103	0.22	45000000	5.305	0	Brain (Grey matter)
Hypophysis	4	55	7.958	0.1	2500	159.155	0.1	0.5	100000	159.155	0.2	40000000	15.915	0	Thyroid gland
Hypothalamus	4	55	7.958	0.1	2500	159.155	0.1	0.5	100000	159.155	0.2	40000000	15.915	0	Thyroid gland
Intervertebral Disc	4	38	13.263	0.15	2500	144.686	0.15	0.15	100000	318.31	0.1	40000000	15.915	0	Cartilage

Kidney	4	47	7.958	0.1	3500	198.944	0.22	0.05	250000	79.577	0.22	30000000	4.547	0	Kidney
Kidney (Cortex)	4	47	7.958	0.1	3500	198.944	0.22	0.05	250000	79.577	0.22	30000000	4.547	0	Kidney
Kidney (Medulla)	4	47	7.958	0.1	3500	198.944	0.22	0.05	250000	79.577	0.22	30000000	4.547	0	Kidney
Large Intestine	4	50	7.958	0.1	3000	159.155	0.2	0.01	100000	159.155	0.2	40000000	1.592	0	Large Intestine
Large Intestine Lumen	4	50	7.234	0.1	7000	353.678	0.1	0.2	1200000	318.31	0.1	25000000	2.274	0	Muscles
Larynx	4	38	13.263	0.15	2500	144.686	0.15	0.15	100000	318.31	0.1	40000000	15.915	0	Cartilage
Liver	4	39	8.842	0.1	6000	530.516	0.2	0.02	50000	22.736	0.2	30000000	15.915	0.05	Liver
Lung	2.5	18	7.958	0.1	500	63.662	0.1	0.03	250000	159.155	0.2	40000000	7.958	0	Lung
Lung (Deflated)	4	45	7.958	0.1	1000	159.155	0.1	0.2	500000	159.155	0.2	10000000	15.915	0	Lung (Deflated)
Lung (Inflated)	2.5	18	7.958	0.1	500	63.662	0.1	0.03	250000	159.155	0.2	40000000	7.958	0	Lung (Inflated)
Lymphnode	4	55	7.958	0.1	2500	159.155	0.1	0.5	100000	159.155	0.2	40000000	15.915	0	Thyroid gland
Mandible	2.5	10	13.263	0.2	180	79.577	0.2	0.02	5000	159.155	0.2	100000	15.915	0	Bone (Cortical)
Medulla Oblongata	4	40	7.958	0.1	700	15.915	0.15	0.04	200000	106.103	0.22	45000000	5.305	0	Cerebellum
Meniscus	4	38	13.263	0.15	2500	144.686	0.15	0.15	100000	318.31	0.1	40000000	15.915	0	Cartilage
Midbrain	4	40	7.958	0.1	700	15.915	0.15	0.04	200000	106.103	0.22	45000000	5.305	0	Cerebellum
Mucous Membrane	4	50	7.234	0.1	7000	353.678	0.1	0.2	1200000	318.31	0.1	25000000	2.274	0	Muscles
Muscle	4	50	7.234	0.1	7000	353.678	0.1	0.2	1200000	318.31	0.1	25000000	2.274	0	Muscles
Nerve	4	26	7.958	0.1	500	106.103	0.15	0.006	70000	15.915	0.2	40000000	15.915	0	Nerve
Ovary	4	40	8.842	0.15	400	15.915	0.25	0.3	100000	159.155	0.27	40000000	15.915	0	Ovary
Pancreas	4	55	7.958	0.1	2500	159.155	0.1	0.5	100000	159.155	0.2	40000000	15.915	0	Thyroid gland
Patella	2.5	10	13.263	0.2	180	79.577	0.2	0.02	5000	159.155	0.2	100000	15.915	0	Bone (Cortical)
Penis	4	40	8.842	0.1	50	3.183	0.1	0.25	100000	159.155	0.2	10000000	1.592	0	Aorta Wall
Pharynx	1	0	0	0	0	0	0	0	0	0	0	0	0	0	Pharynx
Pineal Body	4	55	7.958	0.1	2500	159.155	0.1	0.5	100000	159.155	0.2	40000000	15.915	0	Thyroid gland

Placenta	4	56	8.377	0.1	5200	132.629	0.1	0.7	0	159.155	0.2	0	15.915	0	Blood
Pons	4	40	7.958	0.1	700	15.915	0.15	0.04	200000	106.103	0.22	45000000	5.305	0	Cerebellum
Prostate	4	55	7.958	0.1	5000	159.155	0.1	0.4	100000	159.155	0.2	40000000	15.915	0	Testis
Salivary Gland	4	55	7.958	0.1	2500	159.155	0.1	0.5	100000	159.155	0.2	40000000	15.915	0	Thyroid gland
SAT (Subcutaneous Fat)	2.5	9	7.958	0.2	35	15.915	0.1	0.035	33000	159.155	0.05	10000000	15.915	0.01	Fat (Average Infiltrated)
Seminal vesicle	4	55	7.958	0.1	5000	159.155	0.1	0.4	100000	159.155	0.2	40000000	15.915	0	Testis
Skin	4	32	7.234	0	1100	32.481	0.2	0.0002	0	159.155	0.2	0	15.915	0.2	Skin (Dry)
Skull	2.5	10	13.263	0.2	180	79.577	0.2	0.02	5000	159.155	0.2	100000	15.915	0	Bone (Cortical)
Small Intestine	4	50	7.958	0.1	10000	159.155	0.1	0.5	500000	159.155	0.2	40000000	15.915	0	Small Intestine
Small Intestine Lumen	4	50	7.234	0.1	7000	353.678	0.1	0.2	1200000	318.31	0.1	25000000	2.274	0	Muscles
Spinal Cord	4	26	7.958	0.1	500	106.103	0.15	0.006	70000	15.915	0.2	40000000	15.915	0	Nerve
Spleen	4	48	7.958	0.1	2500	63.662	0.15	0.03	200000	265.258	0.25	50000000	6.366	0	Spleen
Stomach	4	60	7.958	0.1	2000	79.577	0.1	0.5	100000	159.155	0.2	40000000	15.915	0	Stomach
Stomach Lumen	4	50	7.234	0.1	7000	353.678	0.1	0.2	1200000	318.31	0.1	25000000	2.274	0	Muscle
Tendon\Ligament	4	42	12.243	0.1	60	6.366	0.1	0.25	60000	318.31	0.22	20000000	1.326	0	Tendon/Ligament
Testis	4	55	7.958	0.1	5000	159.155	0.1	0.4	100000	159.155	0.2	40000000	15.915	0	Testis
Thalamus	4	45	7.958	0.1	400	15.915	0.15	0.02	200000	106.103	0.22	45000000	5.305	0	Brain (Grey Matter)
Thymus	4	55	7.958	0.1	2500	159.155	0.1	0.5	100000	159.155	0.2	40000000	15.915	0	Thyroid gland
Thyroid Gland	4	55	7.958	0.1	2500	159.155	0.1	0.5	100000	159.155	0.2	40000000	15.915	0	Thyroid gland
Tongue	4	50	7.958	0.1	4000	159.155	0.1	0.25	100000	159.155	0.2	40000000	15.915	0	Tongue
Tooth	2.5	10	13.263	0.2	180	79.577	0.2	0.02	5000	159.155	0.2	100000	15.915	0	Bone (Cortical)
Tooth (Dentine)	2.5	10	13.263	0.2	180	79.577	0.2	0.02	5000	159.155	0.2	100000	15.915	0	Bone (Cortical)
Tooth (Enamel)	2.5	10	13.263	0.2	180	79.577	0.2	0.02	5000	159.155	0.2	100000	15.915	0	Bone (Cortical)
Trachea	2.5	38	7.958	0.1	400	63.662	0.1	0.3	50000	15.915	0.2	1000000	15.915	0	Trachea

Trachea Lumen	1	0	0	0	0	0	0	0	0	0	0	0	0	0	Trachea Lumen
Ureter\Urethra	4	40	8.842	0.1	50	3.183	0.1	0.25	100000	159.155	0.2	10000000	1.592	0	Aorta Wall
Urinary Bladder	2.5	16	8.842	0.1	400	159.155	0.1	0.2	100000	159.155	0.2	10000000	15.915	0	Urinary Bladder
Urinary Bladder Wall	2.5	16	8.842	0.1	400	159.155	0.1	0.2	100000	159.155	0.2	10000000	15.915	0	Urinary Bladder Wall
Uterus	4	55	7.958	0.1	800	31.831	0.1	0.2	300000	159.155	0.2	35000000	1.061	0	Uterus
Vagina	4	50	7.958	0.1	3000	159.155	0.2	0.01	100000	159.155	0.2	40000000	1.592	0	Large Intestine
Vertebrae	2.5	10	13.263	0.2	180	79.577	0.2	0.02	5000	159.155	0.2	100000	15.915	0	Bone (Cortical)

APPENDIX B

PEER-REVIEWED PUBLICATIONS BASED UPON THIS RESEARCH

1. L. J. Crowther, R. L. Hadimani, and D. C. Jiles, "Effect of Anatomical Brain Development on Induced Electric Fields During Transcranial Magnetic Stimulation," in press, *IEEE Transactions on Magnetics*, vol.50, no.11, 2014, DOI: 10.1109/TMAG.2014.2326819.

2. S. D. March, S. Stark, R. L. Hadimani, D. R. Stiner, M. Senter, K. Spoth, L. J. Crowther, and D. C. Jiles, "Thermal and Mechanical Analysis of Novel Transcranial Magnetic Stimulation Coil for Mice," *IEEE Transactions on Magnetics*, vol.50, no.9, Sep 2014, DOI: 10.1109/TMAG.2014.2316479.

3. L. J. Crowther, R. L. Hadimani, A. G. Kanthasamy, and D. C. Jiles, "Transcranial magnetic stimulation of mouse brain using high-resolution anatomical models," *Journal of Applied Physics*, vol.115, no.17, pp.17B303-17B303-3, May 2014, DOI: 10.1063/1.4862217.

4. L. J. Crowther, K. Porzig, R. L. Hadimani, H. Brauer, and D. C. Jiles, "Realistically Modeled Transcranial Magnetic Stimulation Coils for Lorentz Force and Stress Calculations During MRI," *IEEE Transactions on Magnetics*, vol.49, no.7, pp.3426-3429, Jul 2013, DOI: 10.1109/TMAG.2013.2247578.

5. L. J. Crowther, K. Porzig, R. L. Hadimani, H. Brauer, and D. C. Jiles, "Calculation of Lorentz Forces on Coils for Transcranial Magnetic Stimulation During Magnetic Resonance Imaging," *IEEE Transactions on Magnetics*, vol.48, no.11, pp.4058-4061, Nov 2012, DOI: 10.1109/TMAG.2012.2202888.

6. L. J. Crowther, I. C. Nlebedim, and D. C. Jiles, "Developments in deep brain stimulation using time dependent magnetic fields," *Journal of Applied Physics*, vol.111, no.7, pp.07B325-07B325-3, Apr 2012, DOI: 10.1063/1.3676623.

7. P. I. Williams, P. Marketos, L. J. Crowther, and D. C. Jiles, "New Designs for Deep Brain Transcranial Magnetic Stimulation," *IEEE Transactions on Magnetics*, vol.48, no.3, pp.1171-1178, Mar 2012, DOI: 10.1109/TMAG.2011.2170703.

8. L. J. Crowther, P. Marketos, P. I. Williams, Y. Melikhov, D. C. Jiles, and J. H. Starzewski, "Transcranial magnetic stimulation: Improved coil design for deep brain investigation," *Journal of Applied Physics*, vol.109, no.7, pp.07B314-07B314-3, Apr 2011, DOI: 10.1063/1.3563076.

APPENDIX C

CONFERENCE PRESENTATIONS BASED UPON THIS RESEARCH

1. L. J. Crowther, R. L. Hadimani, and D. C. Jiles, "Computational Analysis of Induced Electric Fields During Transcranial Magnetic Stimulation," 36th International Conference of the IEEE Engineering in Medicine and Biology Society, Chicago, IL, USA, 26-30 August 2014.

2. Y. Meng, J. Qu, Z. Xu, L. J. Crowther, R. L. Hadimani*, and D. C. Jiles, "Development of Adjustable Halo Coil Configuration for Deep Brain Transcranial Magnetic Stimulation," 36th International Conference of the IEEE Engineering in Medicine and Biology Society, Chicago, IL, USA, 26-30 August 2014.

3. L. J. Crowther, R. L. Hadimani, and D. C. Jiles, "Effect of Brain Development on Induced Electric Fields During Transcranial Magnetic Stimulation," International Mag- netics Conference, Intermag 2014, Dresden, Germany, 4-8 May 2014.

4. Y. W. Meng, J. K. Qu, R. L. Hadimani*, L. J. Crowther, and D. C. Jiles, "Development of Variable Halo Coil Configuration for Deep Brain Transcranial Magnetic Stimulation," 2nd Annual Minnesota Neuromodulation Symposium, Minneapolis, MN, USA, 10-11 April 2014.

5. L. J. Crowther, R. L. Hadimani, and D. C. Jiles, "Numerical dosimetry of transcranial magnetic stimulation coils," 2014 APS Physics March Meeting, Denver, CO, USA, 3-7 March 2014.

6. S. D. March, S. Stark, L. J. Crowther, R. L. Hadimani, and D. C. Jiles*, "Novel transcranial magnetic stimulation coil for mice," 2014 APS Physics March Meeting, Denver, CO, USA, 3-7 March 2014.

7. A. Carr, G. Zenitsky, L. J. Crowther, R. L. Hadimani*, V. Anantharam, A. G. Kanthasamy, and D. C. Jiles, "Treatment for Traumatic Brain Injury in Mice Using Transcranial Magnetic Stimulation: A Preliminary Study," 2014 APS Physics March Meet- ing, Denver, CO, USA, 3-7 March 2014.

8. L. J. Crowther, R. L. Hadimani, and D. C. Jiles, "A Numerical Dosimetry Study for Pediatric Transcranial Magnetic Stimulation," 6th International IEEE EMBS Conference on Neural Engineering, San Diego, CA, USA, 6-8 November 2013.

9. S. D. March, S. McAtee, M. Senter, K. Spoth, D. R. Stiner, L. J. Crowther, R. L. Hadimani, and D. C. Jiles, "Focused and Deep Brain Magnetic Stimulation Using New Coil Design in Mice," 6th International IEEE EMBS Conference on Neural Engineering, San Diego, CA, USA, 6-8 November 2013.

10. L. J. Crowther, R. L. Hadimani, A. Kanthasamy, and D. C. Jiles*, "Transcranial Magnetic Stimulation of Mouse Brain Using High-Resolution Anatomical Models," 58th Conference on Magnetism and Magnetic Materials, Denver CO, USA, 4-8 November 2013.

11. R. L. Hadimani*, S. D. March, S. McAtee, K. Spoth, D. R. Stiner, L. J. Crowther, and D. C. Jiles, "Development of Deep Brain and Focused Transcranial Magnetic Stimulation Coil for Mice," 58th Conference on Magnetism and Magnetic Materials, Denver, CO, USA, 4-8 November 2013.

12. L. J. Crowther, R. L. Hadimani, and D. C. Jiles, "Improved transcranial magnetic stimulation coil design with realistic head modeling," 2013 APS Physics March Meeting, Baltimore, MD, USA, 18-22 March 2013.

13. R. L. Hadimani*, K. Porzig, L. J. Crowther, H. Brauer, H. Toepfer, and D. C. Jiles, "The Effect of Variation in Permittivity of Different Tissues on Induced Electric Field in the Brain during Transcranial Magnetic Stimulation," 2013 APS Physics March Meeting, Baltimore, MD, USA, 18-22 March 2013.

14. L. J. Crowther, K. Porzig, R. L. Hadimani, H. Brauer, and D. C. Jiles, "Realistically modeled TMS coils for Lorentz force and stress calculations during MRI," 12th Joint MMM/Intermag Conference, Chicago, IL, USA, 14-18 January 2013.

15. R. L. Hadimani*, K. Porzig, L. J. Crowther, H. Brauer, H. Toepfer, and D. C. Jiles, "Effect of Permittivity and Conductivity Variation on Induced Electric Field During Transcranial Magnetic Stimulation," 34th International Conference of the IEEE Engineering in Medicine and Biology Society, San Diego, CA, USA, 28 August - 1 September 2012.

16. L. J. Crowther, R. L. Hadimani, and D. C. Jiles, "Calculation of Lorentz forces on coils for transcranial magnetic stimulation," International Magnetics Conference, Intermag 2012, Vancouver, BC, Canada, 7-11 May 2012.

17. L. J. Crowther, I. C. Nlebedim and D. C. Jiles, "Developments in Deep Brain Stim- ulation using Time Dependent Magnetic Fields," 56th Conference on Magnetism and Magnetic Materials, Scottsdale, AZ, USA, 30 October - 3 November 2011.

18. L. J. Crowther and D. C. Jiles*, "Improved Designs for Field Generation for Non Invasive Transcranial Magnetic Stimulation," 38th Annual Review of Progress in Quan- titative Nondestructive Evaluation, Burlington, VT, USA, 17-22 July 2011.

19. L. J. Crowther and D. C. Jiles, "Transcranial Magnetic Stimulation for non-invasive monitoring and treatment of the brain," IEEE Magnetics Society Summer School, New Orleans, LA, USA, 22-28 May 2011.

20. L. J. Crowther and D. C. Jiles*, "Coil design optimization using structurally detailed models for Transcranial Magnetic Stimulation," International Magnetics Conference, Intermag 2011, Taipei, Taiwan, 25-29 April 2011.

21. L. J. Crowther, P. I. Williams, and D. C. Jiles, "Deep Brain Stimulation using Magnetic Fields," 2011 APS Physics March Meeting, Dallas, TX, USA, 21-25 March 2011.

22. L. J. Crowther, P. Marketos, P. I. Williams, Y. Melikhov, D. C. Jiles, and J. H. Starzewski, "Transcranial Magnetic Stimulation: Improved Coil Design for Deep Brain Investigation," 55th Conference on Magnetism and Magnetic Materials, Atlanta, GA, USA, 14-18 November 2010.

23. L. J. Crowther, P. I. Williams, and D. C. Jiles, "Realistic Head Modeling for Field Optimization in Transcranial Magnetic Stimulation," Magstim/University of Oxford 2010 TMS Summer School, Oxford, UK, 28-29 June 2010.